

A GO/PO tool for synthesizing shaped multi-surface dielectric lens antennas

Master thesis - Electrical Engineering

Leila Gottmer

A GO/PO tool for synthesizing shaped multi-surface dielectric lens antennas

by

Leila Gottmer

in partial fulfilment of the requirements for the degree of

Master of Science
in Electrical Engineering

at the Delft University of Technology,
to be defended publicly on 21 December, 2022 at 10:00 AM.

Student number:	4454448	
Supervisor:	Prof. dr. N. Llombart, Dr. S.O. Dabironezare	
Thesis committee:	Prof. dr. N. Llombart,	TU Delft
	Prof. dr. A. Neto,	TU Delft
	Dr. W. Jellema,	SRON
	Dr. S.O. Dabironezare,	TU Delft

The work presented in this thesis was performed at:
Tera-Hertz Sensing Group
Department of Microelectronics
Faculty of Electrical Engineering, Mathematics and Computer Science
Delft University of Technology

Copyright ©2022 by Leila Gottmer.
All rights reserved.

Acknowledgements

I would like to express my sincere gratitude to the professors of this group, Prof. dr. Andrea Neto, Prof. dr. Nuria Llombart and dr. Daniele Cavallo. Your enthusiasm during lectures in the bachelor and master inspired me to do my master thesis in the Terahertz sensing group.

I also want to thank my supervisor, prof. dr. Nuria Llombart. You have been a tremendous supervisor. You made time to answer questions, and give extremely valuable input, even when you were busy. Your eye for detail and your immense knowledge on these topics never ceases to amaze me. Not only did I gain more knowledge on quasi-optics, you have also shown me that research does not have to be scary. Thank you for your advice, patience, and most importantly, your understanding.

I would also like to thank my daily supervisor, dr. Shahab Dabironezare. You have been an incredible supervisor. You were always more than willing to answer any question that arose. Whether it were trivial questions, or coding problems, you were always there to patiently guide me through the process. Thank you for encouraging me, and thank you for your valuable advice during the master.

Furthermore, I want to thank the THz sensing group for creating a very nice working environment. I enjoyed the morning coffee chats, the lunches and the post lunch cakes.

To my friends, I appreciate your support and encouragement.

To my family in Morocco. Merci beaucoup pour votre soutien, أحبكم.

Last, but most certainly not least. I would like to thank my mother and my sister. I am profoundly grateful for your support during the past few years. I could not have done this without you by my side, كلاكما تعني العالم بالنسبة لي وأنا أحبكما.

*Leila Gottmer
Delft, December 2022*

Contents

Acknowledgements	i
1 Introduction	1
1.1 Background	1
1.2 Proposed methodology	2
1.3 Thesis outline	3
2 Modifying the shape of lens elements fed by a single antenna	4
2.1 Lens Antenna Geometry	4
2.1.1 Elliptical Lens	4
2.1.2 Shape Modification of the Elliptical Lens	6
2.1.3 Lens Feed Definition	9
3 Optimization Kernel	11
3.1 Shaped Lens Antenna Optimization Kernel	11
3.1.1 Reaction integral over the lens surface	12
3.1.2 Transmitted fields	13
3.1.3 Incident field definition	15
4 Optimization procedure	18
4.1 Optimization problem	18
4.2 Initial Guess Points	19
4.2.1 Initial guess for the f-number	19
4.2.2 Initial guess for the lateral displacement	19
4.3 Parameter Search Range	20
4.4 Setup of the optimizer and optimizer choice	20
5 Case study: plastic elliptical lens	22
5.1 Scanning to 25 degrees in a plastic lens	23
5.1.1 Scanning case in the H-plane	23
5.2 CST validation	30
5.2.1 Setting up the full wave simulation	31
5.2.2 Results: Optimizer vs. Full Wave Simulator	35
5.3 Bandwidth performance of the proposed shaped lens antennas	36
5.4 Scanning in the E- and D-plane	37
5.5 Testing the theoretical scanning performance of plastic lens antennas	40
5.5.1 45 degree scanning scenario	40
5.5.2 60 degree scanning scenario	42
5.5.3 Scan loss versus scan angle	44
6 Multi lens analysis	46
6.1 Multi lens example scenario	46
6.1.1 Lens parametrization	47
6.2 Multi layer lens analysis	49
6.2.1 Ray tracing for multi layer components	50
6.2.2 Geometrical Optics for multi lens QO systems	51
6.3 Propagation of the EM fields through the multi-lens geometry	55
6.3.1 Finding the field outside the hyper-hemispherical lens	56
6.3.2 Finding the field outside the hyperbolic lens	56
6.3.3 Propagating the field to the flat surface	56
6.3.4 Efficiency terms for a multi lens QO system	57
6.4 Physical Optics validation	58

6.5	Application cases	59
6.5.1	Broadside case	59
6.5.2	Scanning cases	62
7	Conclusion	69
7.1	Summary and Conclusion	69
7.2	Future Outlook	70
	References	71
A	Derivatives of the Zernike expansion	73
B	Derivations for the radii of curvature of an arbitrary surface	74

List of Figures

1.1	Examples of solutions addressing the low scanning performance of low density dielectric lenses, with (a) being the dielectric grating wedge in the lens [2] and (b) is an example of a shaped dielectric lens [3].	1
1.2	Examples of multi-layer lenses, with (a) being a inversely magnified dual-lens system [5] and (b) is an core-shell leaky-wave lens antenna [12].	2
2.1	Illustration of the ellipse definition.	5
2.2	Modifying the shape of the Elliptical lens.	6
2.3	Examples of the higher order phase aberrations where the z-axis ranges from -1 to 1	7
2.4	Examples of the behaviour of the radial polynomial for $n = 2, 4, 6$ and $m = 0$	8
2.5	Increasing the domain of the lens from ρ to $\bar{\rho}$	9
2.6	A Gaussian feed modeled in a dielectric with a relative permittivity of ϵ_r	9
2.7	An illustration of the lateral and vertical feed displacement in addition to the introduced tilt angle.	10
3.1	Analysis on a lens antenna performed on the equivalent aperture. [15]	11
3.2	The scenario under investigation with a standard elliptical lens antenna illuminated by a plane wave.	12
3.3	The induction surface S with the equivalent magnetic and electric currents defined on the surface.	13
3.4	Defining point Q_1 on the inside of the lens	13
3.5	A zoom in of the surface around point Q_1 . Where Snell's law is applied to determine the field on the outside of the lens at point Q_1	14
3.6	The Fourier transform of the incident field, to illustrate the side lobe level control.	15
3.7	The incident field definition for a scanning case, where the shadow region is shown as the grey region on the lens.	16
3.8	The top view of the equivalent aperture	17
4.1	An illustration of a lens antenna geometry and the considered parameters for the optimization procedure	18
4.2	Top level illustration of the optimizer setup	19
4.3	The output of the surrogateopt optimizer.	21
4.4	The Pareto solutions of the two competing objective functions, where the grey shaded area shows the usable solutions.	21
5.1	Dielectric gratings implemented in a lens antenna.	22
5.2	Scan loss for a 25° beam steering case in an integrated plastic lens [1].	23
5.3	The tangent incident (a,b) and transmitted (c,d) fields on the lens surface in 2D in both amplitude and phase for the base lens.	25
5.4	The tangent incident (a,b) and transmitted (c,d) fields on the lens surface in 2D in both amplitude and phase for the unshaped lens.	26
5.5	The radiated far fields for the target and the optimized lens antenna for a scanning case of 25°	27
5.6	The ray tracing plot for the 25° scanning case (a) and the added surface Δ_s of the modified lens (b).	28
5.7	The tangent incident (a,b) and transmitted (c,d) fields on the lens surface in 2D in both amplitude and phase	29
5.8	The radiated far fields for the target and the optimized lens antenna for a scanning case of 25°	30

5.9	The far field of the optimized lens antenna evaluated in transmission using the analysis method in transmission.	31
5.10	The optimized lens antenna geometry exported to the CST environment.	32
5.11	The designed feed in CST.	33
5.12	The radiated far field of the Huygens' source implemented in CST.	33
5.13	The 3D pattern of the feed.	34
5.14	The H-plane of the radiated far field from CST versus the H-plane of the radiated far field from the optimizer.	35
5.15	The E-plane of the radiated far field from CST versus the E-plane of the radiated far field from the optimizer.	35
5.16	The bandwidth performance of the lens.	37
5.17	The tangent incident (a,b) and transmitted (c,d) fields on the lens surface in 2D in both amplitude and phase for the E-plane	38
5.18	The radiated far fields for the target and the optimized lens antenna for a scanning case of 25° in the E-plane.	38
5.19	The tangent incident (a,b) and transmitted fields (c,d) on the lens surface in 2D in both amplitude and phase for the E-plane	39
5.20	The radiated far fields for the target and the optimized lens antenna for a scanning case of 25° in the D-plane.	40
5.21	The ray tracing plot for the 45° scanning case (a) and the added surface Δs of the modified lens (b).	41
5.22	The tangent incident (a,b) and transmitted (c,d) fields on the lens surface in 2D in both amplitude and phase	41
5.23	Far field pattern for the 45° case	42
5.24	The ray tracing plot for the 60° scanning case (a) and the added surface Δs of the modified lens (b).	43
5.25	The tangent incident (a,b) and transmitted (c,d) fields on the lens surface in 2D in both amplitude and phase	43
5.26	Far field pattern for the 60° case.	44
5.27	Scan loss versus scan angle.	45
5.28	The shaped lenses for the 25° , 45° and 60° case, respectively.	45
6.1	Dual lens setup with the silicon hyper-hemispherical lens shown in blue and the plastic hyperbolic lens shown in Green	47
6.2	The enclosed surface s^+ where the reaction integral is performed.	49
6.3	Schematic overview of the lens with its respective regions considered for the ray tracing procedure.	50
6.4	The result of the ray tracing procedure after steps 1 – 3.	51
6.5	The primary wavefront A_1	52
6.6	The elementary area around point P_1 defined as dA_1	53
6.7	The secondary wavefront A_2 with its respective elementary area around point P defined as dA_2	53
6.8	The field is incident upon a transmitting surface	54
6.9	The two different coordinate systems shown in point P on the wavefront.	55
6.10	The lens setup with the three evaluation points Q_1 , Q_2 and Q_3	56
6.11	An visualisation of the PO validation for the considered scenario	58
6.12	The amplitude and phase on the hyper-hemispherical lens	59
6.13	The amplitude and phase on the hyperbolic surface using the GO method (a,b) and the PO validation method (c,d).	60
6.14	The phase and amplitude on the flat surface of the hyperbolic lens with the results of the GO method shown in (a,b) and the results of the PO method shown in (c,d).	61
6.15	The radiated far field for the broadside case.	61
6.16	The ray tracing results for 5 beams scanning	62
6.17	The amplitude and phase on the hyper-hemispherical lens	63
6.18	The amplitude and phase on the hyperbolic surface using the GO method (a,b) and the PO validation method (c,d).	63

6.19	The phase and amplitude on the flat surface of the hyperbolic lens with the results of the GO method shown in (a,b) and the results of the PO method shown in (c,d).	64
6.20	The radiated far field for the 5 beams scanning case.	64
6.21	The ray tracing results for 15 beams scanning	65
6.22	The amplitude and phase on the hyper-hemispherical lens	65
6.23	The amplitude and phase on the hyperbolic surface using the GO method (a,b) and the PO validation method (c,d).	66
6.24	The phase and amplitude on the flat surface of the hyperbolic lens with the results of the GO method shown in (a,b) and the results of the PO method shown in (c,d).	67
6.25	The radiated far field for the 15 beams scanning case.	67

List of Tables

4.1	Upper and lower bounds for the optimization parameters.	20
5.1	Base lens parameters.	24
5.2	Base lens results.	24
5.3	The directivity, gain maximum achieved sidelobe levels, and scan loss of the target versus the optimized pattern.	24
5.4	Optimized parameter results.	25
5.5	Efficiencies after the optimization process.	26
5.6	The directivity, gain and maximum achieved sidelobe levels of the target versus the optimized pattern.	27
5.7	Optimized parameter results.	28
5.8	Efficiencies after the optimization process.	28
5.9	The directivity, gain and maximum achieved sidelobe levels of the target versus the optimized pattern.	29
5.10	The performance metric of the optimized lens antenna obtained using the MATLAB based analysis code.	30
5.11	CST versus optimizer results	36
5.12	Optimized parameter results for the E-plane.	37
5.13	Optimized parameter results for the D-plane.	39
5.14	Optimized parameter results.	40
5.15	The performance metric of the optimized lens antenna for a 45° scanning case, obtained using the MATLAB based analysis code.	42
5.16	Optimized parameter results.	42
5.17	The performance metric of the optimized lens antenna for a 60° scanning case obtained using the MATLAB based analysis code.	44
6.1	The gain and directivity for the broadside case.	62
6.2	The gain and directivity for the 5 beams scanning case.	65
6.3	The gain and directivity for the 15 beams scanning case.	68
6.4	The time elapsed for the cascaded GO and the PO analysis.	68

Introduction

1.1. Background

Due to the growing trends toward radar and communication systems operating at frequency bands above 100 GHz, there is a demand for high gain and low cost antenna systems. The demand for low-cost antennas is to make them accessible for mass-market applications. The high gain is required to compensate for higher path spreading loss and lower output power sources at (sub)-mm wavelengths. To satisfy these demands, low permittivity ($\epsilon_r \leq 2.5$) plastic lens antennas are a good candidate. These plastic materials exhibit relatively low dielectric losses. Moreover, low cost fabrication techniques exist (i.e. milling, injection molding) for these type of lenses. However, one downside of plastic lenses is that steering capabilities are limited due to the curvature of the elliptical lenses in addition to the required large off-focus feed displacements [1].



Figure 1.1: Examples of solutions addressing the low scanning performance of low density dielectric lenses, with (a) being the dielectric grating wedge in the lens [2] and (b) is an example of a shaped dielectric lens [3].

Several solutions exist that address the low scanning performance of low density dielectric lenses (see Fig. 1.1). For example, [2] proposes the use of a dielectric grating wedge in the lens. In [4] symmetric dielectric pins are added into the waveguide feeder to improve the scanning capabilities of the lens antenna. In this thesis, the potential in terms of scanning capabilities of lens antennas that are fabricated in low density plastic materials is investigated further.

One method that could improve the scanning capabilities is modifying the shape of the lens antenna. Several shaping techniques for lens antennas exist [5], [6], [7]. In this work, the effect of shape modification using a Zernike [8] expansion is investigated. Moreover, a computationally efficient analysis method based on antenna in reception is employed as a kernel for to optimize low density shaped lens antenna geometries.

Another approach for achieving wide scanning performance is by introducing multiple lens surfaces

(see Fig.1.2) in the Quasi-Optical (QO) design. Recently, sensing and imaging systems for (sub)-mm wavelengths have been demonstrated that require QO systems with wide scanning and wideband performance. Large available bandwidths are beneficial for several applications including, 3D radar systems [9], passive radiometry [10] systems and astronomical spectrometers [11]. The image acquisition speed in all of these applications improves with a larger number of antennas simultaneously looking at different pixels in the image.

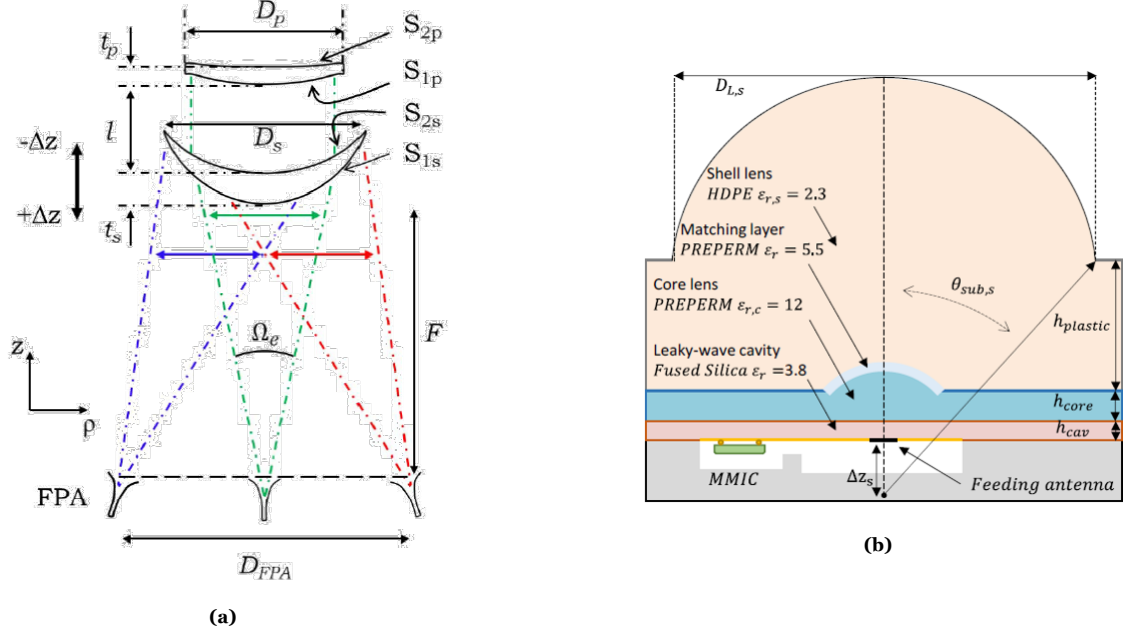


Figure 1.2: Examples of multi-layer lenses, with (a) being a inversely magnified dual-lens system [5] and (b) is an core-shell leaky-wave lens antenna [12].

Several analysis techniques exist to analyse multi-lens QO components. A multi surface Physical Optics (PO) approach can be employed to propagate the radiation from the antenna feed through multiple transmitting surfaces. Such analysis can also be performed by coupling commercial software such as CST [13] and GRASP [14] with a similar PO based approach for larger lens components and full wave simulation for integrated lenses. However, these methods are oftentimes extremely time-consuming since the lens components are large in terms of the wavelength and placed at relatively small distances from each other. Therefore, it is important to develop techniques that can analyse these multi-layer QO elements efficiently. In this work, such an analysis technique of these elements is proposed and studied.

1.2. Proposed methodology

This work proposes a computationally efficient analysis method for single layer and multi-layer Quasi-Optical components. This method applies Geometrical Optics (GO) and ray tracing techniques to perform a field matching on the lens surface. For the single layer components, the developed code is the kernel of a MATLAB optimizer. Here, the feed location, feed tilt and surface expansion coefficients are optimized. This code allows for a time efficient analysis of the scanning performance of the single layer components. Based on this approach, a few wide scanning scenarios using low density integrated lens antennas are investigated by optimizing the lens antenna geometry. The performance of the optimized geometries is validated by full wave simulations using commercial software. For the multi-layer elements, a similar analysis method is proposed. In this case, a combination of a multi transmitting surface GO technique and ray tracing is used to propagate the Electromagnetic (EM) field through multiple transmitting layers.

1.3. Thesis outline

This thesis consists of six chapters. Furthermore, the thesis is split up into two parts. The first part of the thesis consists of four chapters, and it is focused on the optimization process for single layer shaped low density integrated elliptical lenses. Chapter 2 introduces the lens antenna geometry considered for the analysis. Furthermore, a shape modification method using Zernike polynomials is discussed. Chapter 3 provides a detailed explanation of the GO methodology chosen for analyzing lenses for wide scanning applications. In Chapter 4 the optimization process is described, where the optimization problem for low density lens antennas is explained and the setup of the optimizer is discussed. Chapter 5 discusses the performance of the optimized lens antennas for several application cases. Firstly, a 25° scanning case is evaluated, and the obtained results are validated by means of a CST full wave simulation [13]. Furthermore, the bandwidth performance of the proposed shaped lens antenna is investigated. Lastly, the theoretical scanning performance of shaped lens antennas is investigated and analysed.

The second part of the thesis consists of one chapter. Chapter 6 introduces an efficient analysis method using a combination of cascaded GO and ray tracing to analyse multi-lens QO systems. This method is then applied to an application case where a combination of plastic and silicon QO components are used. Finally, the broadside and scanning capabilities of such QO systems are investigated. The analysis method is validated using a time-consuming multi surface PO approach.

2

Modifying the shape of lens elements fed by a single antenna

This work focuses on improving the scanning performance of lens antennas by modifying the shape of standard lens configurations. In this chapter, a single feed per lens antenna architecture is envisioned. These architectures can be used as planar lens arrays generating multiple fixed simultaneous beams, i.e. a Fly's Eye configuration, for the next generation of communication systems [15][2]. Elliptical plastic lenses are common Quasi-Optical (QO) component to realize low-cost and directive antennas above 100 GHz. However, the curvature of such lenses leads to total reflection and shadow region issues in scanning scenarios. As a result, their scanning capabilities are limited. Therefore, this chapter is concentrated on a synthesis and optimization procedure for shaped plastic lenses. Several parameters are optimized to synthesize lens elements with high scanning capabilities. This objective led to the development of a MATLAB based code capable of synthesizing shaped dielectric lenses by optimizing lens antenna parameters. Firstly, the considered elliptical lens QO component is introduced. Secondly, shape modification of the elliptical lens is discussed. Lastly, the lens feed definition is explained.

2.1. Lens Antenna Geometry

This section focuses on the parametrization of the elliptical lens, moreover a surface description of the elliptical lens is given. Furthermore, the lens feed is discussed. Lastly, the shape modification of the elliptical lens is discussed.

2.1.1. Elliptical Lens

In this work the parametrization variables are defined in (x, y, z) (Cartesian) coordinates. The surface of an elliptical lens antenna can be expressed in terms of Cartesian coordinates, as follows

$$\frac{x^2 + y^2}{b^2} + \frac{(z - c)^2}{a^2} = 1 \quad (2.1)$$

where a is the lens semi-major axis; b is the lens semi-minor axis; c is the distance from the centre to the focus O ; For a lens with known a known angular region, diameter and material, the ellipsoid parameters as shown in Fig. 2.1 are calculated as:

$$a = r_{min} \frac{1 - e \cos \theta_0}{1 - e^2} \quad (2.2)$$

$$b = \sqrt{a^2 - c^2} \quad (2.3)$$

$$c = a \cdot e \quad (2.4)$$

where e is the eccentricity, for an elliptical lens the eccentricity is related to the permittivity of the lens material (ϵ_r) as $\frac{1}{\sqrt{\epsilon_r}}$; θ_0^l is the subtended lens angle defined as $\arcsin(\frac{1}{2f_{\#}})$ where $f_{\#}$ is the lens focal length (r_{min}) to diameter (D_l) ratio, $f_{\#} = \frac{r_{min}}{D_l}$.

The x , y and z parameters in Eq. (2.1) represent the Cartesian locations of the ellipsoid from a coordinate system located at the lower focus of the ellipse, as shown in Fig. 2.1. The z coordinates of the surface can be calculated from the two independent parameters x and y as follows:

$$z = a\sqrt{1 - \frac{x^2 + y^2}{b^2}} + c \quad (2.5)$$

Figure 2.1 shows an illustration of the discussed lens parameters.

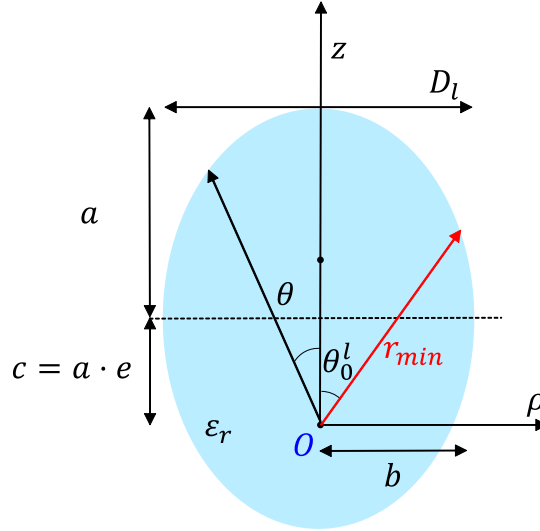


Figure 2.1: Illustration of the ellipse definition.

The normal vector and Jacobian of the surface of a QO component are important parameters for high frequency analysis of these components. These parameters are computed using the derivatives of the surface location vector, $\vec{Q} = x\hat{x} + y\hat{y} + z\hat{z}$, with respect to the independent parameters x and y . Therefore, it is beneficial to define an expression for the normal vector of the elliptical surface S . The Jacobian is given by Eq. (2.6) and the normal vector is given by Eq. (2.7).

$$Jacob = \left| \frac{\partial \vec{Q}}{\partial x} \times \frac{\partial \vec{Q}}{\partial y} \right| \quad (2.6)$$

$$\hat{n}_Q = \pm \frac{\frac{\partial \vec{Q}}{\partial x} \times \frac{\partial \vec{Q}}{\partial y}}{\left| \frac{\partial \vec{Q}}{\partial x} \times \frac{\partial \vec{Q}}{\partial y} \right|} \quad (2.7)$$

where $\frac{\partial \vec{Q}}{\partial x}$ and $\frac{\partial \vec{Q}}{\partial y}$ are the partial derivatives with respect to x and y , respectively. The \pm symbol relates to the sign convention. A $+$ defines an outward pointing normal vector \hat{n} and a $-$ defines an inward pointing normal vector \hat{n} . For an arbitrary point Q on the lens surface the locations in x, y, z are defined as

$$Q_x = x \quad (2.8a)$$

$$Q_y = y \quad (2.8b)$$

$$Q_z = a\sqrt{1 - \frac{x^2 + y^2}{b^2}} + c \quad (2.8c)$$

One can find the partial derivatives with respect to x and y as

$$\frac{\partial Q_x}{\partial x} = 1 \quad (2.9a)$$

$$\frac{\partial Q_y}{\partial x} = 0 \quad (2.9b)$$

$$\frac{\partial Q_z}{\partial x} = \frac{\frac{-ax}{b^2}}{\sqrt{1 - \frac{x^2+y^2}{b^2}}} \quad (2.9c)$$

and

$$\frac{\partial Q_x}{\partial x} = 0 \quad (2.10a)$$

$$\frac{\partial Q_y}{\partial x} = 1 \quad (2.10b)$$

$$\frac{\partial Q_z}{\partial y} = \frac{\frac{-ay}{b^2}}{\sqrt{1 - \frac{x^2+y^2}{b^2}}} \quad (2.10c)$$

respectively. Note that this calculation is shown for one point Q on the surface S . However, this can be applied to all the defined points on the surface S .

2.1.2. Shape Modification of the Elliptical Lens

To achieve wide scanning, one has to compensate for the phase aberrations in the lens. This compensation can be performed by changing the shape of the lens surface. In this chapter, where the focus lies on single feed per lens geometries, the shape of the ellipsoid is modified using a non-rotational symmetric polynomial set referred to as the Zernike expansion [16]. The elliptical lens can be transformed into a modified surface by adding a height modification Δs on top of the elliptical surface, as illustrated in Fig. 2.2.

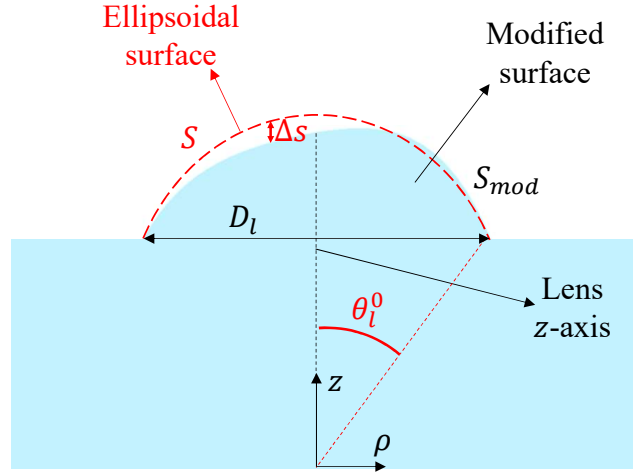


Figure 2.2: Modifying the shape of the Elliptical lens.

here the modified lens surface S_{mod} is defined as

$$S_{mod} = S + \Delta s \lambda_0 \quad (2.11)$$

Where S is the original elliptical surface and Δs is the height modification. This height modification as determined by the Zernike expansion is shown in Eq. (2.12).

$$\Delta s(\bar{\rho}, \phi) = \sum_{m=0}^M \sum_{n=m}^N [A_n^m \cos m\phi + B_n^m \sin m\phi] R_n^m(\bar{\rho}) \quad (2.12)$$

here $0 \leq \bar{\rho} = \frac{\rho}{D_l/2} \leq 1$ and $0 \leq \phi \leq 2\pi$ represent the normalized radial positions on the lens surface and the azimuth location, respectively; M and N are the orders of the polynomials; A_n^m and B_n^m are the weights of the polynomials and $R_n^m(\bar{\rho})$ is the radial function. The radial function is given by

$$R_n^m(\bar{\rho}) = \begin{cases} \sum_{l=0}^{\frac{n-m}{2}} \frac{(-1)^l (n-k)!}{k! (\frac{n+m}{2}-k)! (\frac{n-m}{2}-k)!} \bar{\rho}^{n-2k}, & \text{if } n-m : \text{even} \\ 0, & \text{otherwise} \end{cases} \quad (2.13)$$

The number of required modes is related to the higher order phase aberration complexity. Examples of higher order phase aberrations are shown in Fig. 2.3.

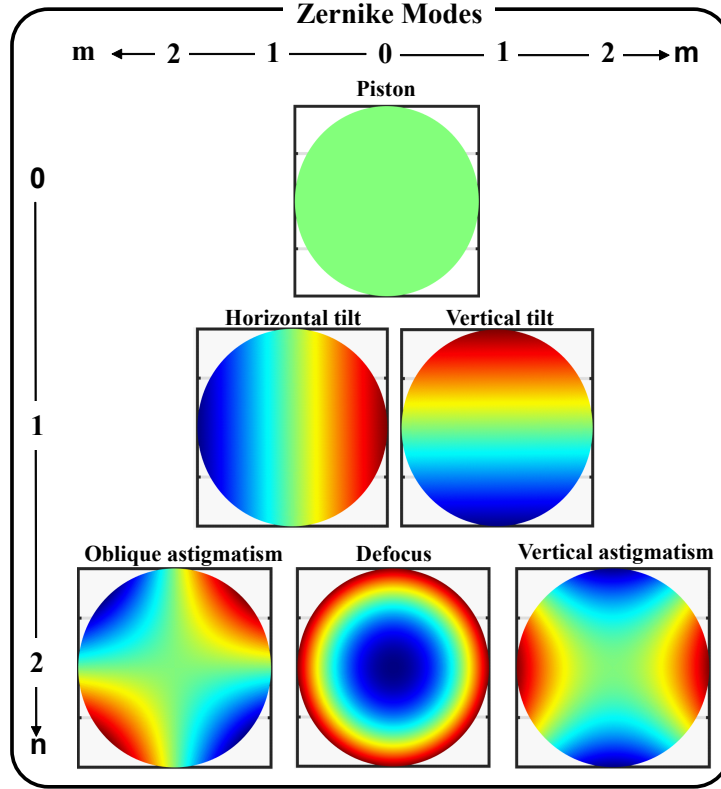


Figure 2.3: Examples of the higher order phase aberrations where the z -axis ranges from -1 to 1

By definition, the Zernike polynomials are orthogonal to each other, moreover, they have well-defined and analytical first and second order derivatives with respect to ρ and ϕ [8]. These derivatives allow for the calculation of the normal vector and the Jacobian for a surface that is modified using the Zernike polynomials. The partial derivatives of Δ_s with respect to x and y can be calculated by applying the chain rule as follows

$$\frac{\partial \Delta_s}{\partial x} = \frac{\partial \Delta_s}{\partial \rho} \frac{\partial \rho}{\partial x} + \frac{\partial \Delta_s}{\partial \phi} \frac{\partial \phi}{\partial x} \quad (2.14)$$

$$\frac{\partial \Delta_s}{\partial y} = \frac{\partial \Delta_s}{\partial \rho} \frac{\partial \rho}{\partial y} + \frac{\partial \Delta_s}{\partial \phi} \frac{\partial \phi}{\partial y} \quad (2.15)$$

The different components have been color coded, and they will be derived separately. Firstly, the derivative of Δ_z with respect to ρ is determined. The product rule is applied to calculate this derivative, and it is given by

$$\frac{\partial \Delta_z}{\partial \rho} = \sum_{m=0}^M \sum_{n=m}^N [A_n^m \sin(m\phi) + B_n^m \cos(m\phi)] \frac{\partial R_n^m(\rho)}{\partial \rho} \quad (2.16)$$

where $\frac{\partial R_n^m(\rho)}{\partial \rho}$ is defined as

$$\frac{\partial R_n^m(\rho)}{\partial \rho} = \sum_{k=0}^{\frac{n-m}{2}} \frac{(-1)^k (n-k)! (n-2k)}{k! (\frac{n+m}{2} - k)! (\frac{n-m}{2} - k)!} \rho^{n-2k-1} \quad (2.17)$$

The derivatives of ρ with respect to x and y are defined as

$$\frac{\partial \rho}{\partial x} = \frac{\cos \phi}{\frac{D_l}{2}} \quad (2.18a)$$

$$\frac{\partial \rho}{\partial y} = \frac{\sin \phi}{\frac{D_l}{2}} \quad (2.18b)$$

and the derivatives of ϕ with respect to x and y are defined as

$$\frac{\partial \phi}{\partial x} = \frac{-\sin \phi}{\frac{D_l}{2} \rho} \quad (2.19a)$$

$$\frac{\partial \phi}{\partial y} = \frac{\cos \phi}{\frac{D_l}{2} \rho} \quad (2.19b)$$

Finally, the last derivative that has to be determined is the first order derivative of Δs with respect to ϕ and it is given by

$$\frac{\partial \Delta s}{\partial \phi} = \sum_{m=0}^M \sum_{n=m}^N [m A_n^m R_n^m(\rho) \cos(m\phi) - m B_n^m R_n^m(\rho) \sin(m\phi)] \quad (2.20)$$

Now all the partial derivatives are known, and these partial derivatives are used to calculate the normal vector and the Jacobian. Since these derivatives are well-defined and analytical in the first order with respect to the independent parameters ρ and ϕ , a lens surface that is modified by adding the Zernike polynomials is a smooth and well-defined shape. As mentioned before, Δz is a function of the two parameters ρ and ϕ . Where ρ is the normalized domain of the radial function. Since there are many modes in the Zernike expansion, it is known [8] that the expansion has high edge values at the border of the unity circle. To explain this, an example is shown in Fig. 2.4 where a radial polynomial is shown for $n = 2, 4, 6$ and $m = 0$. Indeed, it can be observed that the radial function tends to 1 at the edge of the domain border ($\rho = 1$).

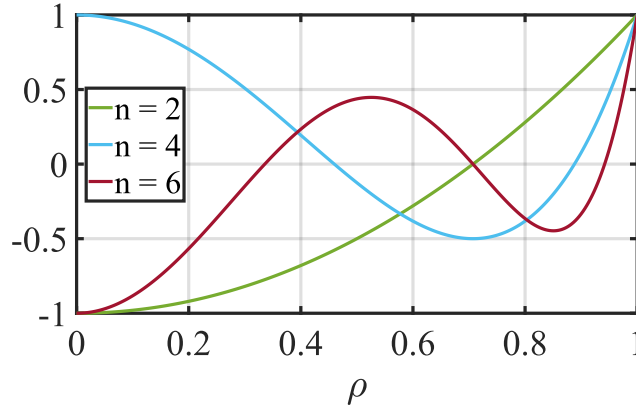


Figure 2.4: Examples of the behaviour of the radial polynomial for $n = 2, 4, 6$ and $m = 0$

These high edge values lead to discontinuities at the edge of the lens. A specific mapping is applied that increases the angular domain of the lens such that the edge of the border is now located at $\bar{D}_l/2$. The surface expansion is then applied to this increased domain, however, the original domain of the lens is used for the actual analysis. Fig. 2.5 illustrates this principle. Where the grey dotted lines illustrate the increased angular region with an angle of θ_{mod} . The corresponding diameter is \bar{D}_l and $\bar{\rho}$ is defined as $\bar{\rho} = \frac{\rho}{D_l/2}$. The actual usable part of the lens has a corresponding diameter of D_l and an angular region of θ_0^l . This method eliminates the high edge values at the border of the unity circle of the relevant domain.

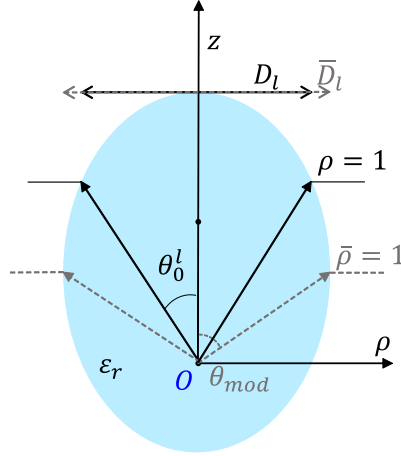


Figure 2.5: Increasing the domain of the lens from ρ to $\bar{\rho}$.

2.1.3. Lens Feed Definition

In this work, a feed with a Gaussian pattern is used as the lens feed. This two-dimensional pattern can be described in terms of u and v coordinates, as follows

$$F(u, v) = e^{[-(\frac{u}{u_0})^2 - (\frac{v}{v_0})^2]} \quad (2.21)$$

where $u = \sin \theta \cos \phi$ and $v = \sin \theta \sin \phi$, u_0 and v_0 are the variances of this Gaussian distribution. In this work, the Gaussian pattern is assumed to be symmetric, meaning that $u_0 = v_0$. One can then calculate the variance for a specific edge taper level T_e at a lens angle θ_l as

$$u_0 = \frac{\sin(\theta_l)}{\sqrt{-\log(10^{(-\frac{T_e}{20})})}} \quad (2.22)$$

In this work, the variance is determined for a -10 dB edge taper level at the lens angle $\theta_l = 35^\circ$. These values are chosen such that the feed's Gaussian profile models the far field pattern of the leaky wave antenna feed, as presented in [1]. Fig. 2.6 shows the feed definition in an infinite dielectric medium of a relative permittivity ϵ_r . In this work, the dielectric medium is plastic with $\epsilon_r = 2.3$.

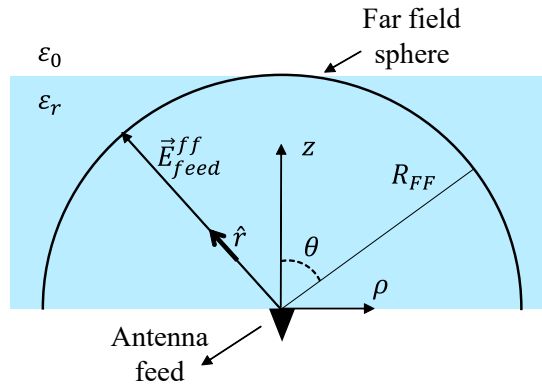


Figure 2.6: A Gaussian feed modeled in a dielectric with a relative permittivity of ϵ_r .

The far field of the feed in Fig. 2.6 is given by

$$\vec{E}_{feed}^{ff} = CF(u, v) \frac{e^{-jk_d R_{FF}}}{4\pi R_{FF}} \hat{p} \quad (2.23)$$

where C is a constant representing the amplitude; k_d is the propagation constant in the dielectric medium; R_{FF} is the far field sphere radius; and $F(u, v)$ is the Gaussian pattern as defined in Eq. (2.21).

The power radiated by the feed into an infinite medium is defined as

$$P_{tx} = \int_0^{2\pi} \int_0^{\pi/2} \frac{1}{2} \Re[\vec{E}_{feed}^{ff} \times \vec{H}_{feed}^{ff*} \cdot \hat{r}] R_{FF}^2 \sin \theta d\theta d\phi \quad (2.24)$$

where \vec{E}_{feed}^{ff} is the electric far field; \vec{H}_{feed}^{ff*} is the magnetic far field;

For scanning cases, the antenna feed can be moved in the vertical and horizontal direction with respect to the lens axis. This change in location results in a modification in the feed's far field phase profile inside the dielectric material. These locations can be optimized to compensate for the linear and quadratic phase terms. Fig. 2.7 illustrates the displacement of the feed in the horizontal direction with respect to the lens axis. In addition, it shows the displacement of the feed in the vertical direction with respect to the lens axis. To improve the radiation from the dielectric medium to air, the feed can be tilted such that the critical angle regions on the lens surface are avoided. This concept is also shown in Fig. 2.7. When a tilt angle is introduced, $u = \sin \theta \cos \phi - \sin \theta_{tilt} \cos \phi_{tilt}$ and $v = \sin \theta \sin \phi - \sin \theta_{tilt} \sin \phi_{tilt}$. This definition is then substituted in Eq. (2.21).

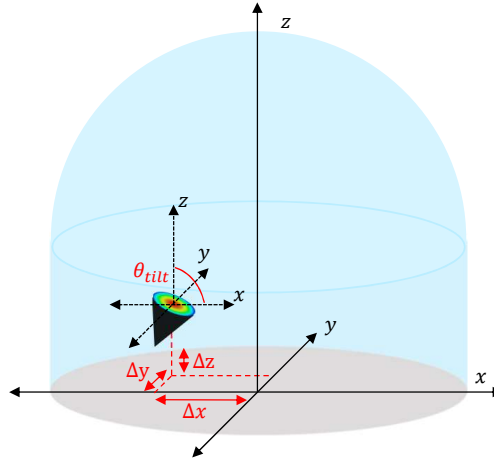


Figure 2.7: An illustration of the lateral and vertical feed displacement in addition to the introduced tilt angle.

3

Optimization Kernel

In previous works, analyses of lens antennas have been predominantly performed on the equivalent lens aperture [3]. This concept is illustrated in Fig. 3.1. In this method the forward Geometrical Optics

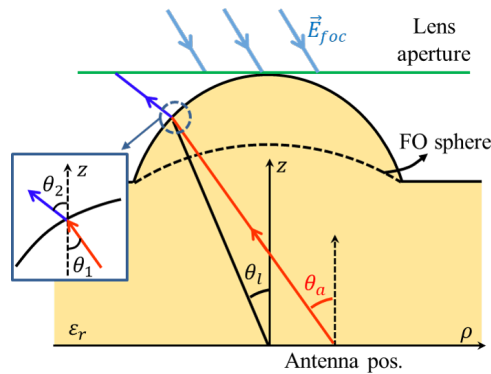


Figure 3.1: Analysis on a lens antenna performed on the equivalent aperture. [15]

(GO) propagation is from the feed to the lens aperture, this results in an irregular grid on the aperture. Therefore, intermediate interpolation steps are required for this analysis method, which results in a time-consuming analysis. To eliminate the intermediate interpolation steps, the analysis can be performed via a field correlation on the lens surface instead. In this method, the analysis is based on the antenna in reception (Rx) methodology. This analysis method is the foundation of the employed optimization kernel, and this method will be discussed in this chapter. Firstly, the goal of the optimization kernel is explained. Secondly, the analysis on the lens surface is discussed. Afterwards, the transmitted field analysis is explained. Lastly, the incident field analysis is explained.

3.1. Shaped Lens Antenna Optimization Kernel

In this section the kernel is explained and to aid this explanation, a general scenario is considered. The scenario under investigation is for a lens antenna that is illuminated by a plane wave from broadside, as illustrated in Fig. 3.2.

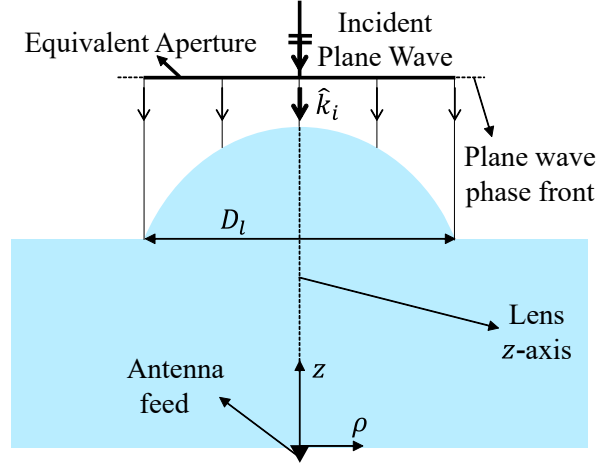


Figure 3.2: The scenario under investigation with a standard elliptical lens antenna illuminated by a plane wave.

Let us consider the geometry as described in Fig 3.2. Here, the lens is illuminated by an incident plane wave from a broadside. The objective is to maximize the received power by the antenna feed. Equivalently, the objective is to maximize the aperture efficiency of the lens antenna. A Thevenin equivalent circuit [2] in reception is considered to define an expression for the received power as

$$P_{rx} = \frac{|V_{oc}I_{tx}|^2}{16P_{rad}^{feed}} \quad (3.1)$$

where P_{rx} is the power received by the feed, V_{oc} is the open circuit voltage, I_{tx} is the current feeding the antenna, and P_{rad}^{feed} is the total power radiated by the feed. This received power is used to define a cost function for the optimization problem. The total efficiency of the lens is defined as

$$\eta_{tot} = \frac{P_{rx}}{P_{in}} = \frac{|V_{oc}I_{tx}|^2}{16P_{rad}^{feed}P_{inc}} \quad (3.2)$$

This antenna receiving efficiency can be split up into two terms, where the first term is the reflection efficiency

$$\eta_{ref} = \frac{P_{tx}^{lens}}{P_{rad}^{feed}} \quad (3.3)$$

The reflection efficiency is defined as the ratio between the total power radiated by the antenna P_{rad}^{feed} , and the power transmitted out of the lens surface P_{lens}^{tx} . The second term is the field match efficiency:

$$\eta_{FM} = \frac{|V_{oc}I_{tx}|^2}{16P_{lens}^{tx}P_{inc}} \quad (3.4)$$

This efficiency represents the field match between the incident and transmitted fields. The total efficiency, as described in Eq. (3.2) is the product of these two efficiency terms. The analysis is performed on the lens surface when calculating these efficiency terms. The next section explains the analysis surface choice.

3.1.1. Reaction integral over the lens surface

As mentioned before, the Thevenin equivalent circuit is applied, it is therefore important to calculate the open circuit voltage V_{oc} . To do this, one can express the voltage as a reaction integral which is defined over an induction surface. In this work the induction surface is the surface of the lens taken just outside the lens, see Fig. 3.3. The expression of the reaction integral is as follows

$$V_{oc}I_{tx} = \iint_{S^+} (\vec{H}_{inc} \cdot \vec{M}_{tx} - \vec{E}_{inc} \cdot \vec{J}_{tx}) dS \quad (3.5)$$

where $[\vec{E}_{inc}, \vec{H}_{inc}]$ are the fields generated by the incident plane wave from Fig. 3.2 on the surface S ; $[\vec{J}_{tx}, \vec{M}_{tx}]$ are the equivalent currents related to the transmitted field at S generated by the lens feed. These two sets of fields are clarified in the next sections.

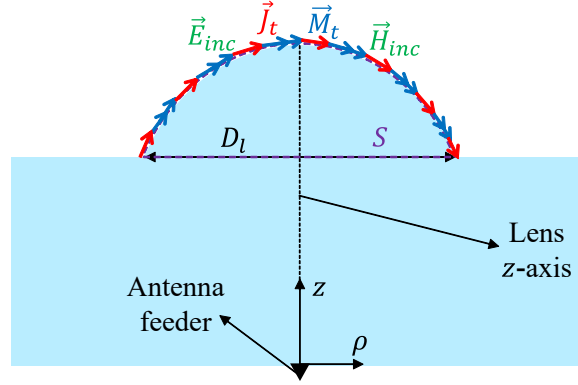


Figure 3.3: The induction surface S with the equivalent magnetic and electric currents defined on the surface.

3.1.2. Transmitted fields

To find the equivalent transmitted electric and magnetic currents as defined in the previous section, one has to calculate the transmitted electric and magnetic fields outside the lens at S^+ . To find this field, a two-step procedure is applied. Firstly, the feed's far field is propagated to the inside of the lens surface (S^-). Secondly, Snell's law of reflection and refraction is applied to obtain the transmitted field on the outside of the lens surface (S^+). By propagating the far field as described in section 2.1.3 to the inside of the lens surface, one arrives at the following expression for the far field

$$\vec{E}_{feed}^{ff} = C e^{-((\frac{u}{v_0})^2 + (\frac{v}{v_0})^2)} \frac{e^{-jk_d |\vec{r}_{lens}|}}{|\vec{r}_{lens}|} \hat{p} \quad (3.6)$$

where C is a constant that represent the amplitude of the far field; k_d is the propagation constant in the dielectric medium; \hat{p} represents the generic polarization unit vector of the far field; $|\vec{r}_{lens}|$ is the distance between the antenna feed and the lens surface as shown in Fig. 3.4.

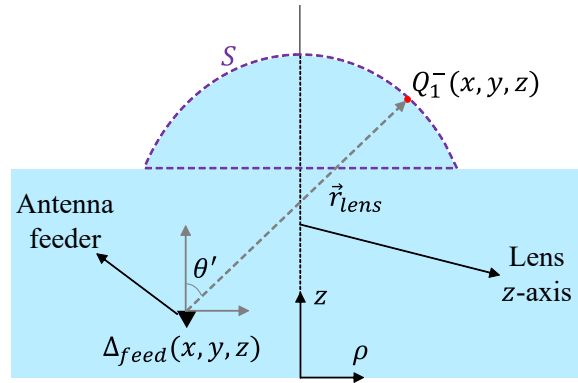


Figure 3.4: Defining point Q_1 on the inside of the lens

To find $|\vec{r}_{lens}|$, a high frequency technique known as backwards ray tracing is applied. Assuming that a point on the lens surface \vec{Q}_1 and the location of the feed $\vec{\Delta}_{feed}$ is known, the direction is determined as

$$\vec{r}_{lens} = \vec{Q}_1 - \vec{\Delta}_{feed} \quad (3.7)$$

and the distance between the feed and the lens surface is defined as

$$|\vec{r}_{lens}| = \sqrt{\vec{r}_{lens} \cdot \vec{r}_{lens}^*} \quad (3.8)$$

The unit vector can also be calculated, and it is defined as

$$\hat{r}_{lens} = \frac{\vec{r}_{lens}}{|\vec{r}_{lens}|} \quad (3.9)$$

It is also important to find the relative u and v in this scenario. Assuming that the feed is displaced and tilted, u and v are defined as

$$u = \sin \theta' \cos \phi' - \sin \theta_{tilt} \cos \phi_{tilt} \quad (3.10a)$$

$$v = \sin \theta' \sin \phi' - \sin \theta_{tilt} \sin \phi_{tilt} \quad (3.10b)$$

here, the tilt angle is expressed as a displacement in the $u - v$ domain. θ' and ϕ' can be related to \vec{r}_{lens} in a reference system located at the feed, see Fig. 3.5. They are expressed as follows

$$\theta' = \arccos \frac{\vec{r}_{lens} \cdot \hat{z}}{|\vec{r}_{lens}|} \quad (3.11a)$$

$$\phi' = \arctan \frac{\vec{r}_{lens} \cdot \hat{y}}{\vec{r}_{lens} \cdot \hat{x}} \quad (3.11b)$$

Next, the far field has to be propagated to the outside of the lens surface S^+ . This surface is denoted by the purple dotted line in Fig. 3.4. The transmitted electric and magnetic fields are shown in Eq. (3.12) and in Eq. (3.13) respectively.

$$\vec{E}_{tx} = \bar{\bar{T}} \cdot \vec{E}_{inside}^{ff} \quad (3.12)$$

$$\vec{H}_{tx} = \frac{1}{\zeta} \hat{k}_t \times \vec{E}_{tx} \quad (3.13)$$

where \hat{k}_t is the transmit direction of propagation; $\bar{\bar{T}}$ is the dyadic transmission coefficient. The dyadic transmission coefficient is expressed as

$$\bar{\bar{T}} = \tau^\perp \hat{p}_t^\perp \hat{p}_i^\perp + \tau^\parallel \hat{p}_t^\parallel \hat{p}_i^\parallel \quad (3.14)$$

where $\hat{p}_i^\perp/\hat{p}_i^\parallel$ are the corresponding polarization unit vectors for the parallel (TM) and perpendicular (TE) components; $\tau^\perp/\tau^\parallel$ are the perpendicular and parallel transmission coefficients, which can be found by applying Snell's law to an assumed locally flat surface on the lens as illustrated in Fig. 3.5.

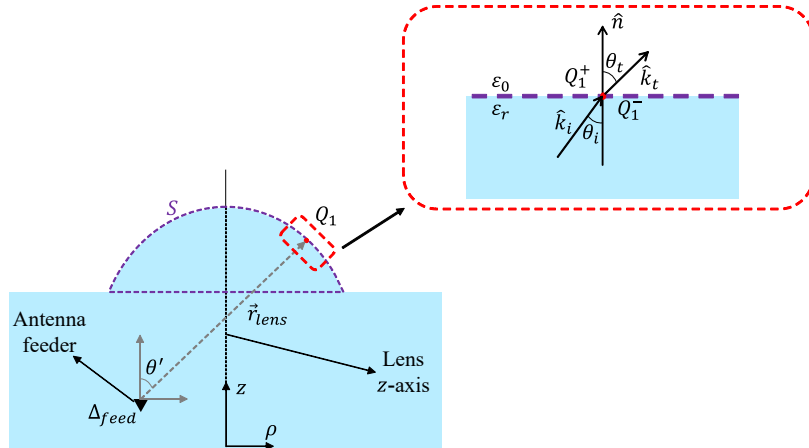


Figure 3.5: A zoom in of the surface around point Q_1 . Where Snell's law is applied to determine the field on the outside of the lens at point Q_1 .

These steps are shown for one point on the lens, but this approach can be applied to the remaining $N - 1$ points on the lens.

Once the transmitted electric and magnetic fields are determined, the equivalent currents of the transmitted field evaluated on the lens surface can be calculated. In this case, M_{tx} is the magnetic equivalent current and J_{tx} is the electric equivalent current.

$$\vec{M}_{tx} = -\hat{n} \times \vec{E}_{tx} \quad (3.15)$$

$$\vec{J}_{tx} = \hat{n} \times \vec{H}_{tx} \quad (3.16)$$

The power that is radiated into free space by the lens is defined as

$$P_{lens}^{tx} = \iint_{S^+} \frac{1}{2} \Re\{\vec{E}_{tx} \times \vec{H}_{tx}^*\} \cdot \hat{n} dS \quad (3.17)$$

where S^+ represents the surface of the lens. Finally, to find the far field, the currents are radiated using a standard Fourier transform far field approach with the free space Green's function.

3.1.3. Incident field definition

Another important component for the calculation of the reaction integral is to determine the incident field. Reciprocity is applied, and the analysis is performed in reception mode. In reception mode, the lens antenna is illuminated by an incident plane wave as shown in Fig. 3.2. The incident plane wave radiation profile is defined as

$$\vec{E}_{inc} = e^{-((\frac{U_{ref}}{u_{inc}})^2 + (\frac{V_{ref}}{v_{inc}})^2)} e^{jk_0 z \hat{p}} \quad (3.18)$$

The radiation profile is similar to the radiation profile of the antenna feed, where the introduced Gaussian taper allows for a better side lobe level control over the desired radiation profile. This sidelobe level control is shown in Fig. 3.6, which shows the Fourier transform of the incident field truncated over a circular aperture (D_l).

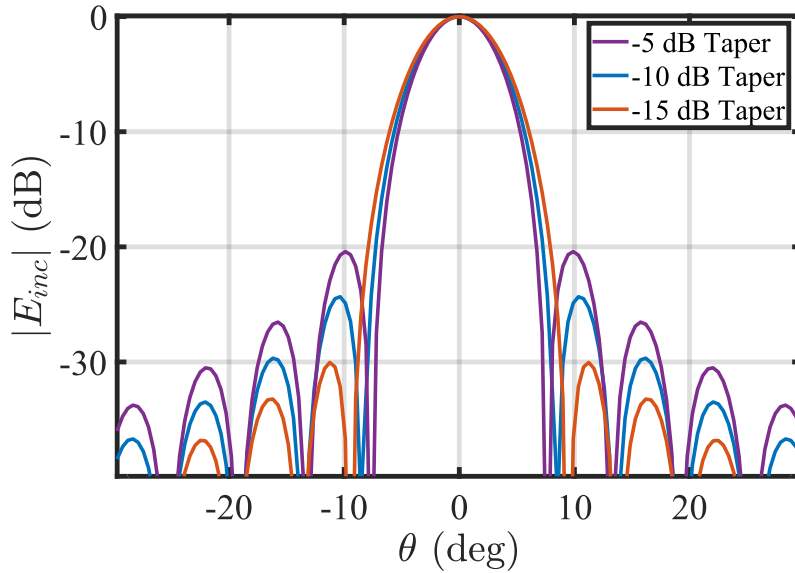


Figure 3.6: The Fourier transform of the incident field, to illustrate the side lobe level control.

Assuming a plane wave relation between the incident electric- and magnetic field, the magnetic field can be expressed as

$$\vec{H}_{inc} = \frac{1}{\zeta} \hat{k}_i \times \vec{E}_{inc} \quad (3.19)$$

where ζ is the medium impedance and \hat{k}_i is the incident direction of propagation. The incident received power is calculated as

$$P_{inc} = \iint_{S^+} \frac{1}{2} \Re\{\vec{E}_{inc} \times \vec{H}_{inc}^*\} \cdot -\hat{n} dS \quad (3.20)$$

here \vec{E}_{inc} is the incident electric field; \vec{H}_{inc} is the incident magnetic field; and \hat{n} is the normal vector of the lens surface.

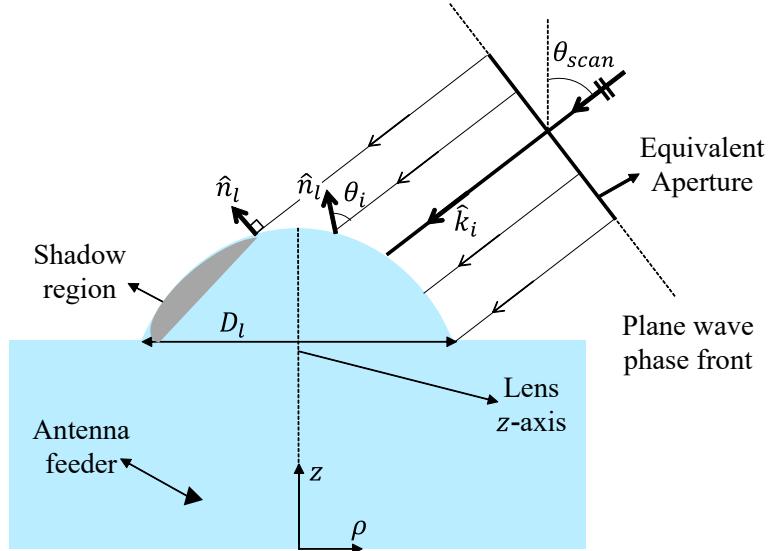


Figure 3.7: The incident field definition for a scanning case, where the shadow region is shown as the grey region on the lens.

Incident field definition for scanning

For scanning cases (see Fig. 3.7), where the incident plane wave's elevation and azimuth angles, θ_{scan} and ϕ_{scan} , are known, one must identify the usable region of the lens.

This usable region is bound by identifying the first and last possible ray that hit the lens. To find these rays, one must first determine the Cartesian components of the incident direction of propagation \hat{k}_i . These components are defined as

$$\hat{k}_{ix} = -\sin \theta_{scan} \cos \phi_{scan} \quad (3.21a)$$

$$\hat{k}_{iy} = -\sin \theta_{scan} \sin \phi_{scan} \quad (3.21b)$$

$$\hat{k}_{iz} = -\cos \theta_{scan} \quad (3.21c)$$

For example, for a broadside incident plane wave, only a z-component of the incident direction of propagation exists. As illustrated in Fig. 3.2. The last ray that hits the lens can be found by calculating θ_i as

$$\theta_i = \arccos(\hat{k}_i \cdot \hat{n}_l) \quad (3.22)$$

where \hat{k}_i is the incident direction of propagation; and \hat{n}_l is the normal vector of the lens. When $\theta_i > 90^\circ$ the rays do not intersect with the lens surface anymore. Therefore, if this condition is applied to all points on the lens, the entire usable region of the lens is found. The portion of the quasi-optical component (lens) that is not illuminated by a skewed incident plane wave is defined as the shadow region. Fig. 3.7 shows this region on the left side of the lens.

Because of the incident field definition, a Gaussian taper can be applied to the incident field. For this, the top view of the equivalent aperture as shown in Fig. 3.8 is useful.

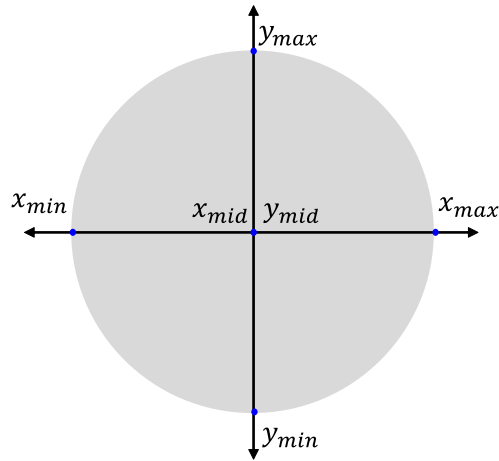


Figure 3.8: The top view of the equivalent aperture

Ideally, one would want to place the amplitude taper in the middle of the aperture. To do this, one can determine the maximum x and y locations of the aperture. Afterwards, U_{ref} and V_{ref} as defined in Eq. (3.18) can be calculated as

$$U_{ref} = \frac{X_{ap} - x_{mid}}{x_{max} - x_{mid}} \quad (3.23a)$$

$$V_{ref} = \frac{Y_{ap} - y_{mid}}{y_{max} - y_{mid}} \quad (3.23b)$$

here x_{mid} , x_{max} , y_{mid} and y_{max} are defined as shown in Fig. 3.8. X_{ap} and Y_{ap} are the points on the aperture itself.

Optimization procedure

Shape optimization of reflectors to directly maximize the aperture efficiency has been widely applied in the reflector antenna community [17]. For integrated lens components, the direct approach does not necessarily result in optimal geometries, mainly because the shaping of transmitting surfaces results in regions of the lens with poor transmission or regions where total internal reflections are present. An alternative approach that can be taken is to maximize the radiation and taper efficiency of the lens antenna, which can be achieved using a multi-objective optimizer. This chapter focuses on the implementation of this optimizer. Firstly, the optimization problem and parameters are introduced. Secondly, optimization setup is discussed. Moreover, a code structure is presented, and finally some optimizer results are discussed.

4.1. Optimization problem

As previously mentioned, the objective of this work is to optimize specified lens antenna parameters in order to improve the radiation performance of the lens. Fig. 4.1 shows the to be optimized parameters in red.

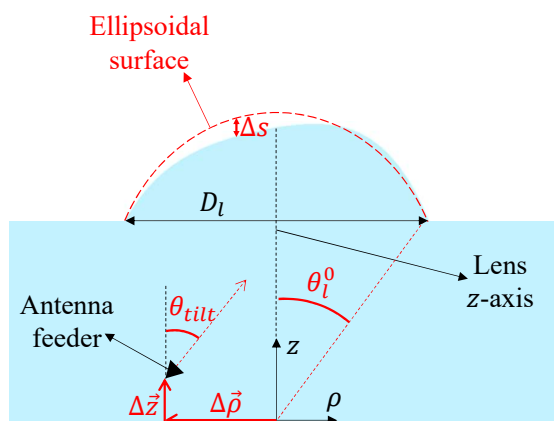


Figure 4.1: An illustration of a lens antenna geometry and the considered parameters for the optimization procedure

The considered optimization parameters are listed as follows:

1. The lens $f_{\#}$, which is related to the lens maximum solid angle θ_l^0
2. The lateral and vertical location of the antenna feed ($\Delta\rho$ and Δz)
3. The tilt angle (θ_{tilt}) of the feed
4. The Zernike expansion coefficients A_n^m and B_n^m , which results in a change of Δs

A block diagram is presented that shows the structure of the optimizer code architecture.

The blocks that are of interest for this chapter are the initialization block and the setup block. Firstly, the initial guess block is discussed, which is followed up by a discussion of the bounds specification.

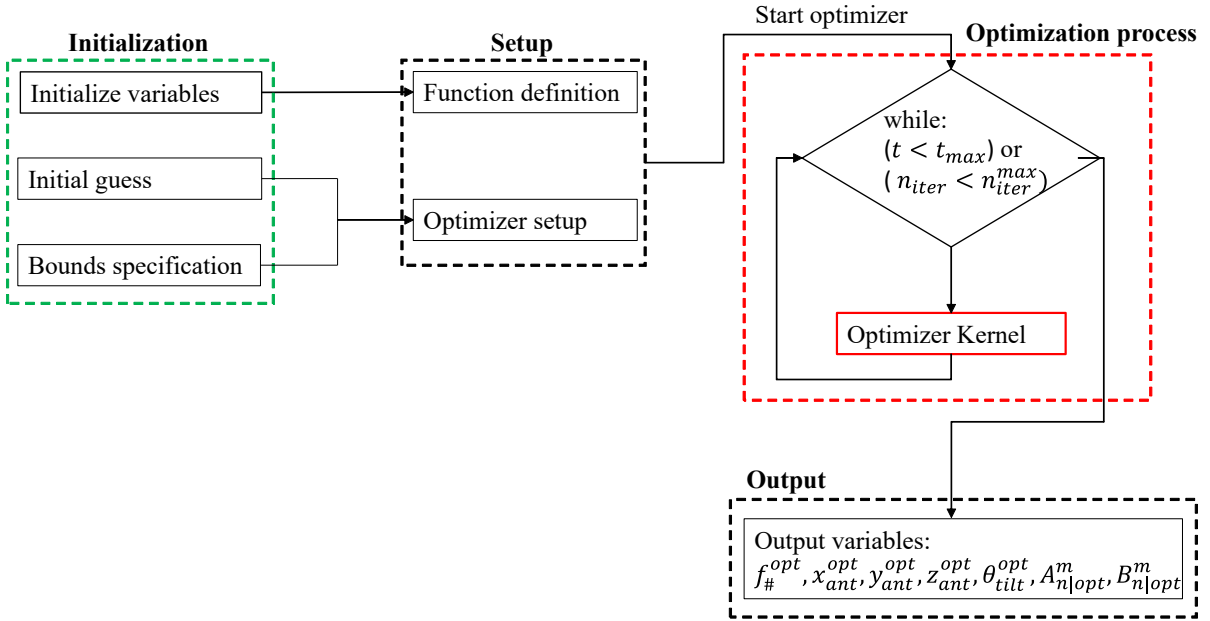


Figure 4.2: Top level illustration of the optimizer setup

4.2. Initial Guess Points

When using an optimizer, there is an opportunity to provide an initial guess. By providing an adequate initial guess, the optimization time could significantly decrease. The initial guesses that are calculated in this work are related to the optimization parameters as discussed in the previous section.

4.2.1. Initial guess for the f-number

The initial guess for the $f_{\#}$ is determined as follows:

$$f_{\#}^{guess} = \frac{1}{2 \cdot \sin \theta_l} \quad (4.1)$$

where θ_l^0 is defined as:

$$\theta_l^0 = \arcsin\left(\sqrt{-\log\left(10^{\frac{T_e^{dB}}{20}} \cdot u_0\right)}\right) \quad (4.2)$$

where T_e^{dB} represents the normalized edge field taper at the θ_l angle. Finally, the initial guess for the tilt angle is chosen to be $\theta_{tilt}^{guess} = \theta_l$.

4.2.2. Initial guess for the lateral displacement

The initial guess for the lateral displacement can be found by placing the feed in a location which compensates, to the first-order, the linear phase present in the focal plane due to illuminating the lens by a plane wave from a (θ_i, ϕ_i) angle. The relationship between the incident angle (θ_i) and the transmitted angle (θ_t) is expressed as

$$\sqrt{\varepsilon_r} \sin \theta_t = \sqrt{\varepsilon_i} \sin \theta_i \quad (4.3)$$

where ε_r is the relative permittivity of the lens material, and ε_i is the relative permittivity of the material outside of the lens. In this case the material outside the lens is vacuum, therefore $\varepsilon_i = 1$. The transmitted angle θ_t is expressed as

$$\theta_t = \arcsin\left(\sin \theta_i \frac{1}{\sqrt{\varepsilon_r}}\right) \quad (4.4)$$

the displacement is found by applying a geometrical relation that relates the displacement of the feed and the location of the feed to the focal distance F of the lens. Where F is defined as $f_{\#}/D$. Therefore, the initial guess for the displacement is given by

$$\vec{\rho}_{guess} = \tan\left(\arcsin\left(\frac{\sin \theta_i}{\sqrt{\varepsilon_r}}\right)\right) \cdot D \cdot f_{guess} \cdot [\cos(\phi_i - \pi)\hat{x} + \sin(\phi_i - \pi)\hat{y}] \quad (4.5)$$

Eq. (4.5) shows a general expression to determine the displacement of the feed in ρ . Where the ϕ_i angle decides how much the feed is displaced in the x- or y-direction. The initial guess discussed in this section are provided as an input for the optimizer such that a reasonable starting point is obtained.

4.3. Parameter Search Range

It is also beneficial to determine a proper search range for the optimizer. A proper range should consider the geometrical limitations of the structure under analysis, as well as the search time of the optimizer. Preferably, the search range should be as small as possible to improve the execution time while still containing a meaningful search space for the optimized parameters.

Table 4.1 displays the parameters and their respective bounds. In particular, the minimum lens $f_{\#}$ is limited by the critical angle of plastic, whereas the upper limit is determined by the limitations in directivity of the considered feed. Even though the theoretical lower limit for the $f_{\#}$ is limited by the critical angle, in this case it is limited by a lens angle of 40° ; For the feed lateral displacement, a $\pm 30\%$ deviation from the initial guess is considered; a $\pm 20\%$ deviation from the initial tilt angle guess is considered; the weight of the Zernike modes, A_n^m and B_n^m are limited to $\pm 2\lambda_0$ to ensure that the surface modification can compensate for the remaining phase mismatch.

Table 4.1: Upper and lower bounds for the optimization parameters.

Parameter	Lower bound	Upper bound
$f_{\#}$	$\frac{1}{2 * \sin(40)}$	2
Δx	$0.7x_{guess}$	$1.3x_{guess}$
Δy	$0.7y_{guess}$	$1.3y_{guess}$
θ_{tilt}	$0.8\theta_i$	$1.2\theta_i$
Δz	0	$10\lambda_0$
A_n^m	$-2\lambda_0$	$2\lambda_0$
B_n^m	$-2\lambda_0$	$2\lambda_0$

4.4. Setup of the optimizer and optimizer choice

This section discusses the setup of the optimizer as well as the considerations related to the optimizer choice. For the function definition, the inputs are usually the known initialization variables and the unknown optimization parameters. The optimizer setup itself consists of determining the settings, the stop conditions. In this work, the *UseParallel* kernel run in parallel. The *MaxTime* setting is a variable that changes according to the difficulty of the optimization problem. For optimizers, it is required to define a cost function to minimize. To define this cost function, one can consider the efficiency terms as discussed in the previous section. The cost functions are defined as

- $f_c^1 = \frac{1}{\eta_{tot}}$
- $f_c^2 = \frac{1}{\eta_{ref}}, \frac{1}{\eta_{FM}}$

These cost functions are appropriate depending on the difficulty of the problem. For a less complex optimization problem, a less complex optimization process is required. For example, for a broadside optimization case where one would only consider changing the lens f-number and the location of the feed, a global solver such as *surrogateopt* [18] from MATLAB's global optimization toolbox will suffice. Additionally, the cost function for this case is defined as $\frac{1}{\eta_{tot}}$. The output of such an optimization process is shown in Fig. 4.3, where the cost function is shown on the y-axis and the number of iterations is shown on the x-axis. It can be observed that the function value indeed decreases and that the optimizer tries to find a minimum. The previously mentioned optimizer is sufficient for less complex optimization cases, however, for a more complex objective function (i.e. for a scanning case with lens shape optimization) it was observed that the two separate efficiency terms seem to follow a different trend. Therefore, a switch is made to a multiobjective optimizer (*gamultiobj*) [18]. This optimizer is capable of optimizing

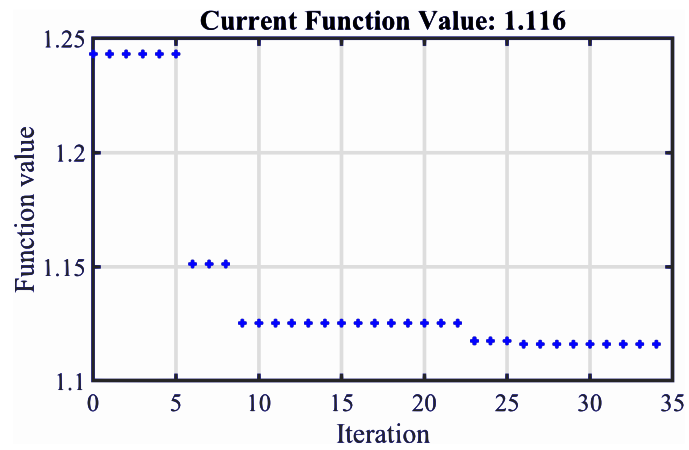


Figure 4.3: The output of the surrogateopt optimizer.

two separate cost functions $\frac{1}{\eta_{ref}}$ and $\frac{1}{\eta_{FM}}$. This optimizer uses a genetic algorithm to find a local Pareto front. Fig. 4.4 shows the Pareto solutions of the two competing objective functions. Here the grey shaded area denotes the region where the usable solutions are located, and each cross represents an optimized solution and its corresponding efficiency terms. In this work, a solution is considered to be sufficient if $\eta_{FM} \geq 0.6$ or $\eta_{ref} \geq 0.6$.

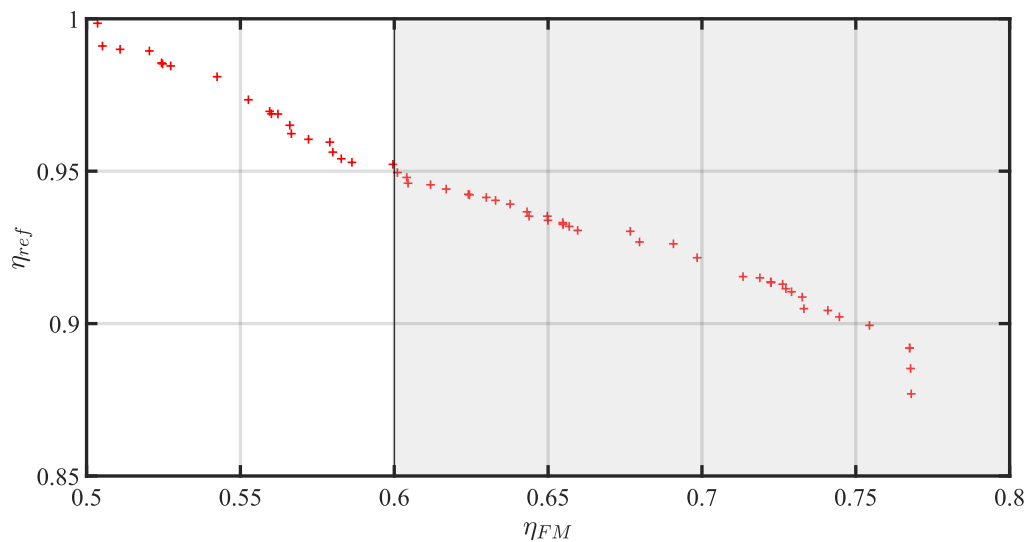


Figure 4.4: The Pareto solutions of the two competing objective functions, where the grey shaded area shows the usable solutions.

5

Case study: plastic elliptical lens

The Terahertz range is important for many applications. An example of one of these applications is the next generation of communication systems. High-gain antennas are required in the frequencies above 100 GHz where these communication systems are envisioned [1]. There has also been an increase in the employment of low permittivity elliptical lenses for these applications. Low permittivity elliptical lenses are adequate for these applications for a few reasons:

- They are cost-effective
- The materials are readily available
- The material is lightweight and low loss

Even though, there are many advantages in using low permittivity elliptical lenses, there are some disadvantages as well. One of these disadvantages is the reduced beam steering capabilities for scanning cases [2]. In a lens design for scanning applications, this disadvantage manifests itself as a higher reflection loss at the lens-air boundary, shadow and total reflection regions on the lens surface. Therefore, a significant performance loss for scanning cases occurs [2].

One solution proposed in[2] is to implement dielectric gratings as shown in Figure 5.1

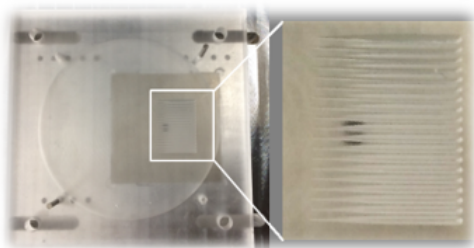


Figure 5.1: Dielectric gratings implemented in a lens antenna.

These gratings are located at a vertical distance z from the ground plane inside a low permittivity elliptical lens. The objective of the gratings is to achieve an enlarged angular field of view (FoV) over a wide band of operation. The gratings are able to create a linear phase shift in the aperture field of the lens feed [2]. This linear phase shift translates into a beam-tilt in the far field of the antenna feed that leads to a more efficient illumination of the lens surface [2]. As a result, spill-over and reflection losses are decreased.

For a 25° beam steering configuration as shown in Fig. 5.2, a scan loss of approximately -4 dB was achieved at the centre frequency f_c of 180 GHz. A -8 dB scan loss was achieved when no gratings were used. The gratings improved the scanning performance, however, the amount of possible beam-tilt is limited.

In this work, the optimization procedure is focused on the described Fly's eye plastic lens scenario. It is studied if shaping the lens will further improve the scanning performance of plastic lenses than those

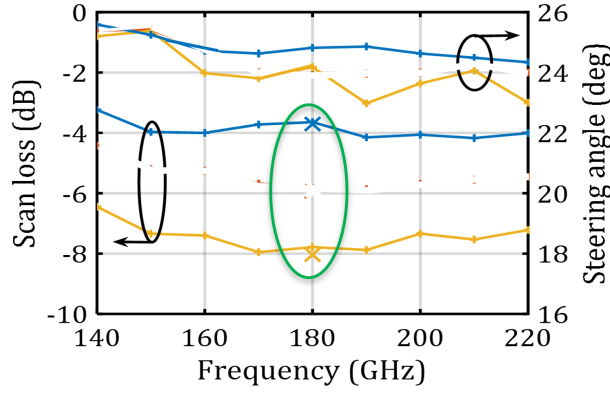


Figure 5.2: Scan loss for a 25° beam steering case in an integrated plastic lens [1].

reported in [1]. In addition, shape modification is applied for wider scanning applications (up to 60°). In the following sections, a plastic lens with a relative permittivity of $\epsilon_r = 2.3$ is studied to optimize the scanning performance of such lenses. Firstly, a scanning case of 25° is considered. Afterwards, a similar lens geometry is simulated in CST [13] to validate the proposed methodology. Lastly, the capabilities of free form plastic lenses are investigated.

5.1. Scanning to 25 degrees in a plastic lens

In this section, a scanning case with a 25° incident plane wave is investigated. Firstly, the scanning scenario and the specifications are introduced. Secondly, an optimization case is considered where the lens parameters are optimized while the lens surface is fixed to its canonical shape. i.e, an ellipsoid. Lastly, a similar optimization case is considered where both the lens parameters and the lens shape are optimized. This approach allows us to investigate the influence of the lens shape on the overall scanning performance of the lens.

5.1.1. Scanning case in the H-plane

Let us now consider the scanning case in [1] as a reference case for the optimization of a plastic lens antenna. The geometrical specification of this optimization case are as follows:

1. Frequency of operation: $f = 180$ GHz
2. Lens diameter: $D = 18\lambda_0$
3. Permittivity of the material: $\epsilon_r = 2.3$
4. Incident plane wave angle: $\theta_{pw}^i = 25^\circ$, $\phi_{pw}^i = 0^\circ$

The used feed is considered ideal, and it has the same definition as described in Chapter 2 (Eq. (3.6)).

Base lens

Prior to the optimization procedure, a base lens geometry and its results are presented. This lens geometry achieves a scan loss that is comparable to the -8 dB scan loss presented in Fig. 5.2. The scan loss is defined as the loss in gain with respect to the broadside case. This lens serves as a proper starting point for the optimization process. Moreover, it can be used to measure how well the optimizer performs. Table 5.1 shows the f-number and the horizontal feed displacement. Table 5.2 shows the obtained efficiencies for this lens geometry. As can be seen, the reflection efficiency is very low, this is because there is a large critical region present on the lens as shown in Fig. 5.3c. Table 5.3 shows the directivity, gain, side lobe level and the scan loss for this geometry, respectively. What can be observed is that the obtained scan loss is approximately -7.3 dB, which is comparable to the -8 dB scan loss found in [2].

Table 5.1: Base lens parameters.

Parameter	Value
$f_{\#}$	0.9
Δx	$-5.9\lambda_0$

Table 5.2: Base lens results.

Efficiency	Value
η	0.17
η_{ref}	0.28
η_{FM}	0.61

Table 5.3: The directivity, gain maximum achieved sidelobe levels, and scan loss of the target versus the optimized pattern.

	Target	Optimized
Directivity (dB)	34.6	32.5
Gain (dB)	34.6	26.9
SLL (dB)	-17.5	-12.4
Scan Loss (dB)		-7.3

Fig. 5.3 shows the tangent incident and transmitted fields on the lens surface in 2D. What can be observed from this is that the transmitted field, shown in Fig. 5.3c, is mostly radiated on the left side of the lens close to the critical angle. This also causes the reflection efficiency to be low.

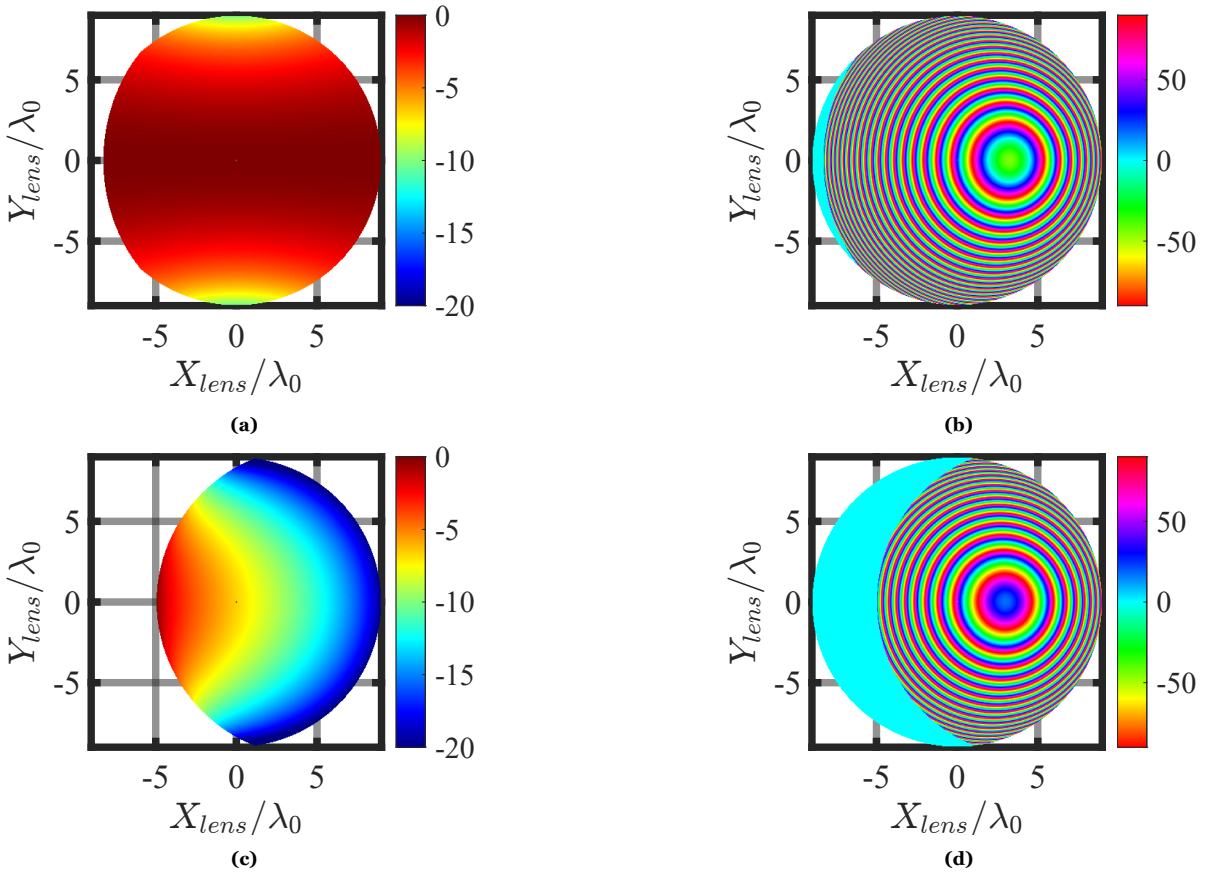


Figure 5.3: The tangent incident (a,b) and transmitted (c,d) fields on the lens surface in 2D in both amplitude and phase for the base lens.

Optimization of lens antenna without modifying the lens shape

The lens antenna geometry is optimized following the in reception procedure as described in Chapter 3. The considered test antenna feed has a Gaussian profile in the far field, as described in Eq. (3.6) with an edge taper of -10 dB at 35° . Table 5.4 shows the optimized geometrical lens parameters for the canonical elliptical lens case. The parameters listed in this table are the ones as described in Section 4.1 The tangent, with respect to the lens surface, magnitude and phase of the incident plane wave are

Table 5.4: Optimized parameter results.

Parameter	Value
$f_\#$	1.05
Δx	$-5.76\lambda_0$
θ_{tilt}	21.1°
Δz	$1.67\lambda_0$

shown in Fig.5.4a and Fig. 5.4b respectively. The transmitted fields of the feed are shown in Fig. 5.4c and Fig. 5.4d, respectively. In this case, η_{ref} is 0.65. The added tilt allows for the maximum of the feed's far field to be guided towards the relevant region without the critical angle. This becomes clear when comparing Fig. 5.3c to Fig. 5.4c. In conclusion, more power can be transmitted out of the lens even if the critical angle region still exists on the left side of the lens surface.

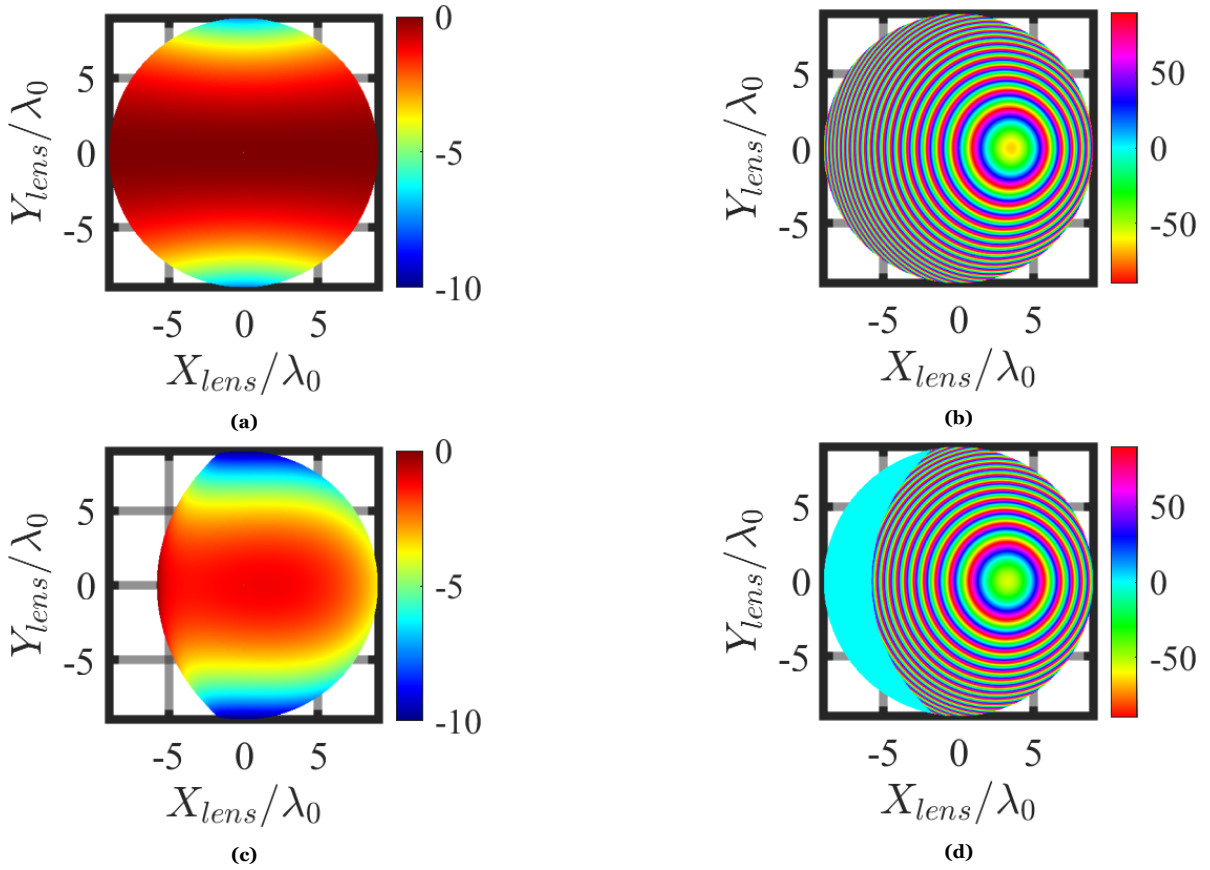


Figure 5.4: The tangent incident (a,b) and transmitted (c,d) fields on the lens surface in 2D in both amplitude and phase for the unshaped lens.

Table 5.5 shows the efficiencies found as a result of the optimization process.

Table 5.5: Efficiencies after the optimization process.

Efficiency	Value
η	0.50
η_{ref}	0.65
η_{FM}	0.77

Fig. 5.5 shows the resulting far field patterns for this optimization case. The scan loss of the optimized geometry is -2.5 dB. This performance is a substantial improvement compared to the scan loss that was reported in [2]. This improvement is partially due to the increased tilt angle. In the previous design in [2] the tilt angle was approximately 5.7° . This was the maximum tilt possible using a physical grating. The proposed larger tilt angle can be achieved using a novel QO architecture, such as the recently proposed core-shell lens geometry in [12].

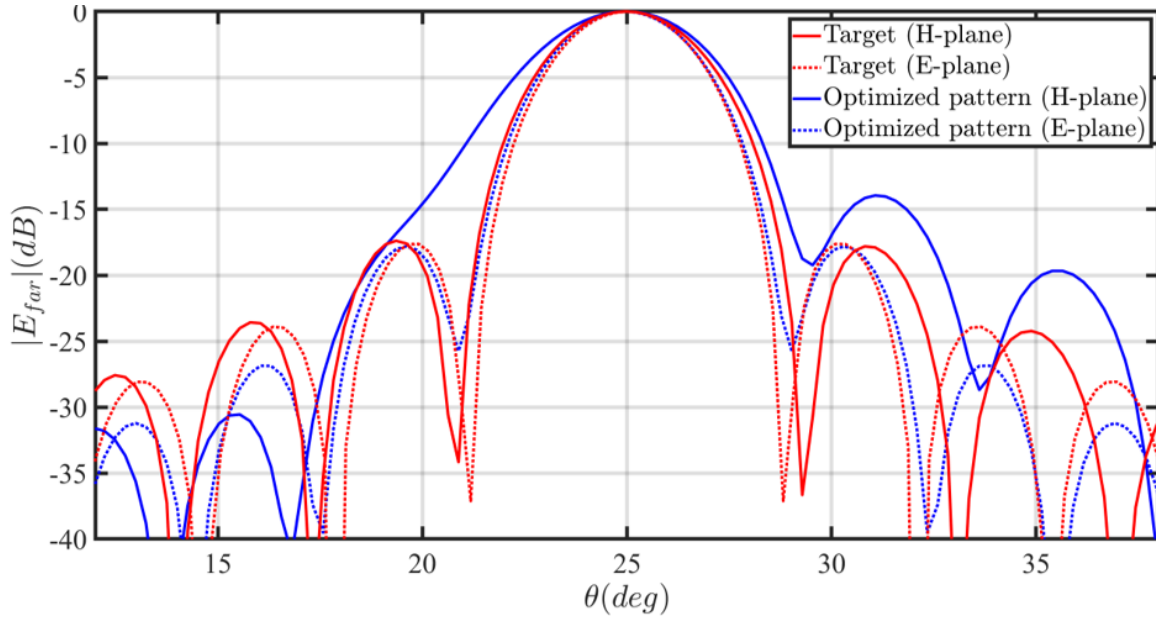


Figure 5.5: The radiated far fields for the target and the optimized lens antenna for a scanning case of 25°.

Table 5.6 compares the gain, directivity, and sidelobe level of the target pattern and the optimized pattern. As can be observed, the loss of directivity with respect to the optimizer target is 1.1 dB, which corresponds to the field matching efficiency. The loss in Gain from the target value, is approximately 3 dB. This value can also be reported in terms of the total efficiency of the lens antenna (0.5), as shown in Table 5.5. The side lobe level of the optimized geometry is approximately 3.4 dB higher than the target (cost function) of the optimizer. The higher side lobe level of the optimized lens antenna pattern is also reflected in the directivity and field match efficiency of this geometry. One could potentially improve the side lobe level if an additional optimization criteria is introduced.

Table 5.6: The directivity, gain and maximum achieved sidelobe levels of the target versus the optimized pattern.

	Target	Optimized
Directivity (dB)	34.6	33.5
Gain (dB)	34.6	31.6
SLL (dB)	-17.4	-13.9
Scan Loss (dB)		-2.5

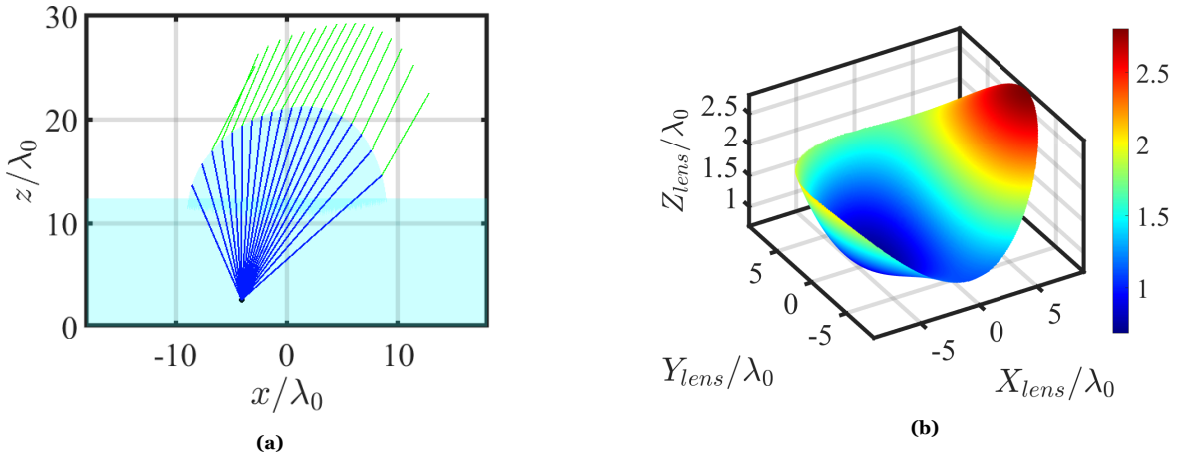
Optimization of a lens antenna by modifying the lens shape

In this subsection, the surface shape modification is added to the optimization process. In this case, the order of the Zernike expansion is 3 ($m = n = 3$). One can assume that the addition of a surface modification increases the complexity of the optimization process. This implies that a longer optimization time is necessary to achieve reasonable results. In this case, the chosen maximum optimization time is $t_{opt} = 60$ minutes. The results of the optimization process are shown in Table 5.7. There are some differences if we compare the previous optimization results to these optimization results. What can be noted is that the $f_{\#}$ has decreased from 1.05 to 0.71. There also appears to be a difference between the lateral and vertical feed displacement as well as the tilt angle. A part of the phase mismatch between the incident field and the transmitted field (Eq. (3.5)) is now compensated for by the surface modification. Therefore, the optimized lateral and vertical feed displacement differ with respect to the previous case. Furthermore, the optimum tilt angle can change by modifying the shape of the surface, since the optimizer attempts to find a tilt angle such that most of the power from the feed of the lens is transmitted out of the lens.

Table 5.7: Optimized parameter results.

Parameter	Value
$f_{\#}$	0.71
Δx	$-4.1\lambda_0$
θ_{tilt}	23.8°
Δz	$2.6\lambda_0$

Fig. 5.6a shows the ray tracing and the modified lens surface. Fig. 5.6b shows the added surface Δ_s of the modified lens.

**Figure 5.6:** The ray tracing plot for the 25° scanning case (a) and the added surface Δ_s of the modified lens (b).

When comparing the amplitudes of the tangent transmitted fields in Fig. 5.4 and Fig. 5.7, it can be seen that there is a significant improvement. Due to the curvature of the modified lens surface, a small region of the lens surface is in the shadow with respect to an incident plane wave arriving from a 25° elevation angle. What's more, the critical angle region has decreased, as shown in Fig. 5.7. This decrease of critical angle region leads to an overall increase of η_{ref} from 0.65 to 0.87. The remaining efficiencies are displayed in Table 5.8. Modifying the lens surface provides more degrees of freedom for the optimizer to achieve a conjugate phase match between the incident and transmitted field, therefore, the field match efficiency is improved from 0.77 to 0.87.

Table 5.8: Efficiencies after the optimization process.

Efficiency	Value
η	0.76
η_{ref}	0.87
η_{FM}	0.87

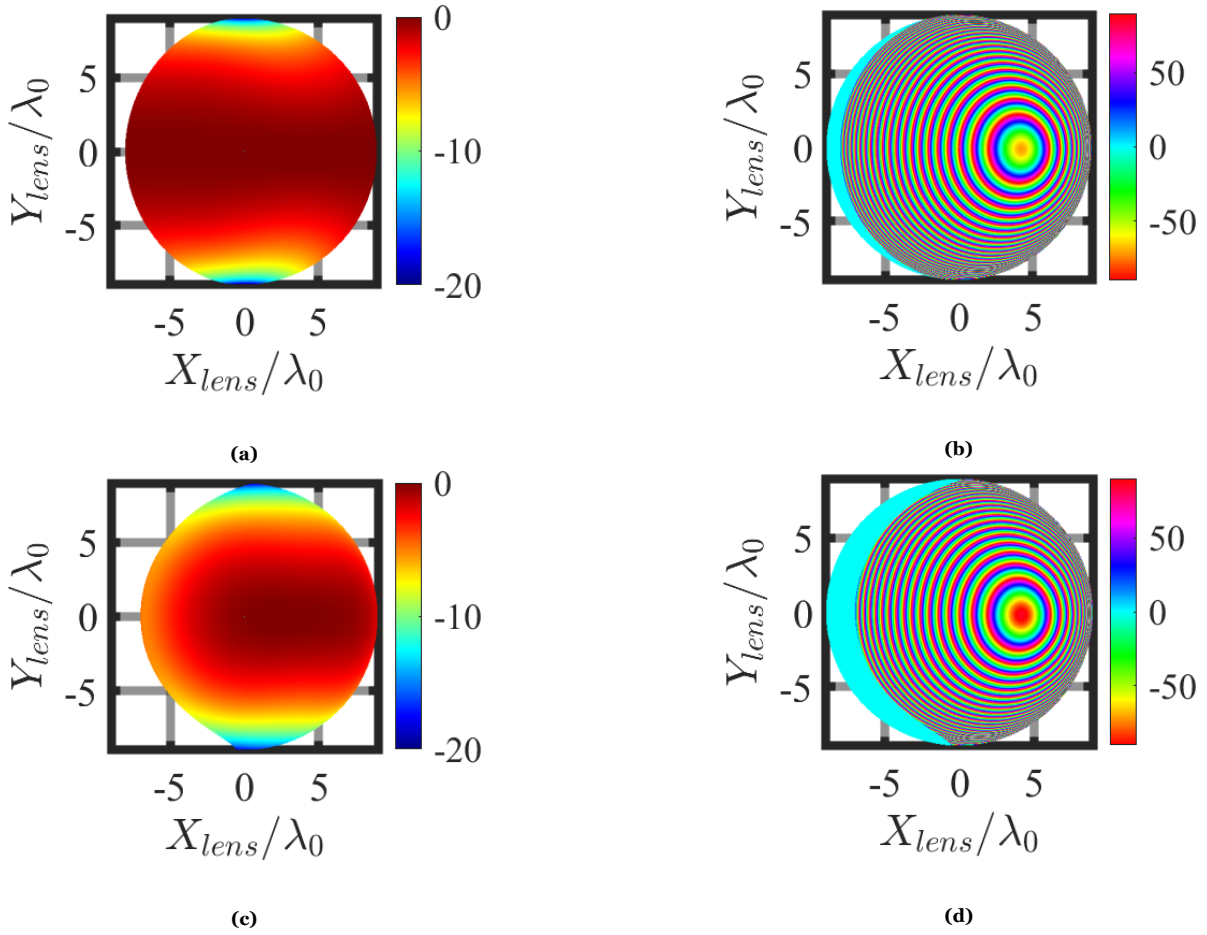


Figure 5.7: The tangent incident (a,b) and transmitted (c,d) fields on the lens surface in 2D in both amplitude and phase

The improvement in the field match efficiency becomes apparent in the far field pattern of the lens antenna in transmission mode, shown in Fig. 5.8. The main lobes of this far field in both planes are matched better to the optimizer target. Moreover, the maximum sidelobe level is reduced to approximately -15 dB. The scan loss in this case is -0.52 dB, which is a significant improvement with respect to the reference case (4 dB [2]) and with respect to the results found in the previous step (2.5 dB).

Table 5.9 compares the gain, directivity, and sidelobe level of the optimizer's target pattern and the optimized pattern for this optimization case.

Table 5.9: The directivity, gain and maximum achieved sidelobe levels of the target versus the optimized pattern.

	Target	Optimized
Directivity (dB)	34.7	34.1
Gain (dB)	34.7	33.5
SLL (dB)	-17.4	-15.5
Scan Loss (dB)		-0.52

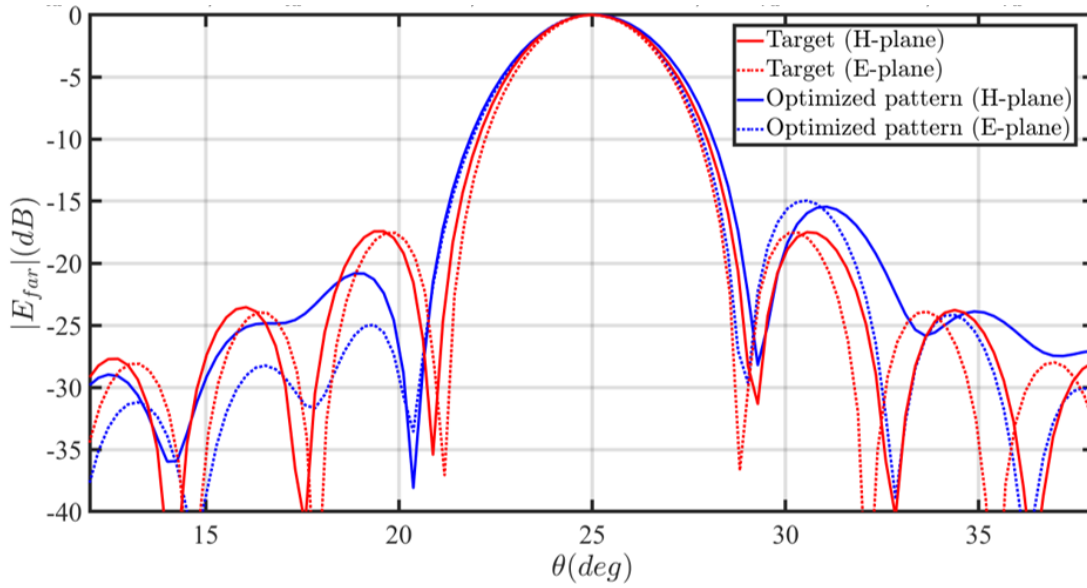


Figure 5.8: The radiated far fields for the target and the optimized lens antenna for a scanning case of 25° .

5.2. CST validation

In the previous section, the optimization results for a shaped plastic lens scanning to 25° were presented. To validate the proposed analysis methodology in reception in combination with the optimization process, a full wave simulation of a similar lens antenna geometry is presented here. The full wave validation is performed using CST STUDIO SUITE [13]. The specifications of the validation case are as follows:

- Frequency of operation: $f = 180$ GHz
- Lens diameter: $D = 10\lambda_0$
- Permittivity of the material: $\epsilon_r = 2.3$
- Incident plane wave angle: $\theta_{pw}^i = 26^\circ$, $\phi_{pw}^i = 0^\circ$
- A tapered Huygens' source is used the test feed antenna

The parameters are similar to the parameters from the previous case, except for the lens diameter. The lens diameter is reduced to $10\lambda_0$ to reduce the configuration cost of a full wave simulator like CST. A similar optimization process to the one described in Section 5.1 is performed for the described scenario. The lens shape, the lateral and vertical displacement, the feed tilt angle, and the lens f-number are optimized. The far field pattern after the lens and relevant performance metrics of the optimized geometry are provided in Fig. 5.9 and Table 5.10, respectively.

Table 5.10: The performance metric of the optimized lens antenna obtained using the MATLAB based analysis code.

Parameter	Value
Directivity	28.7 dB
SLL	-16.5 dB
Gain	28.1 dB
Scan loss	-0.89 dB
η	0.65

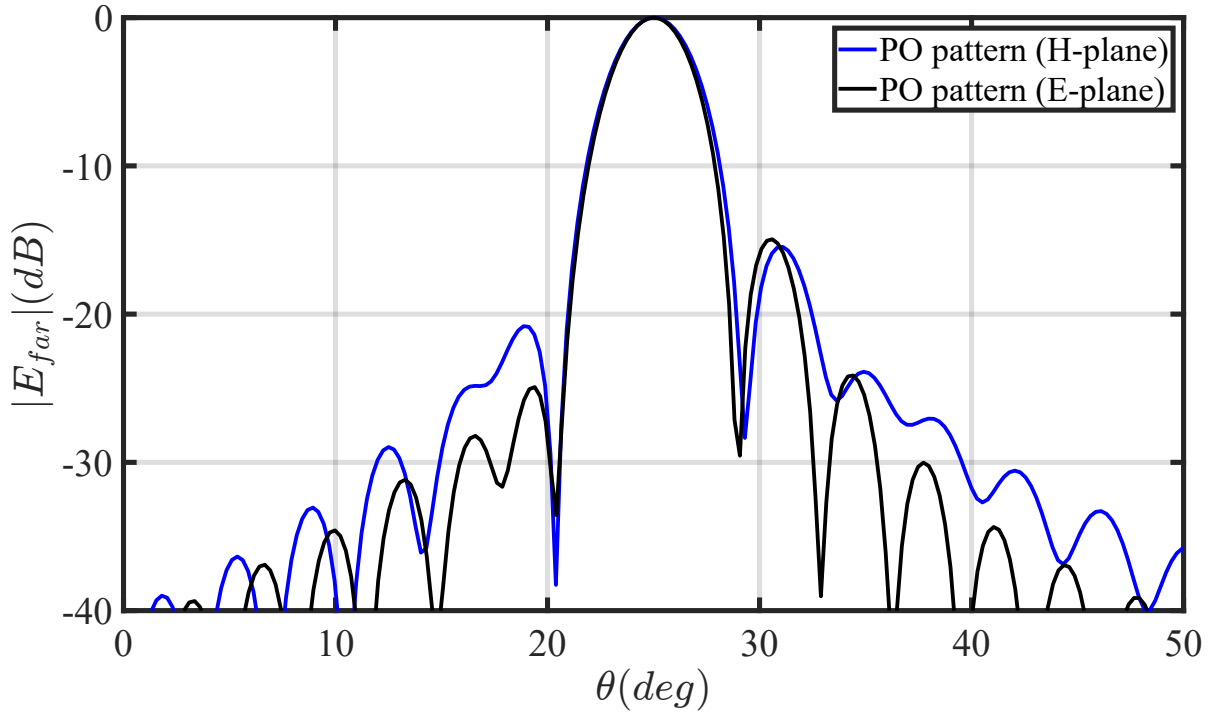


Figure 5.9: The far field of the optimized lens antenna evaluated in transmission using the analysis method in transmission.

5.2.1. Setting up the full wave simulation

The goal is to model the shaped lens surface in CST, however, a surface with Zernike polynomials cannot be modeled directly in CST. A surface can be modeled if a STEP file is provided. To obtain this file, the following steps have to be taken:

1. The optimized weights of the Zernike polynomials are exported to TICRA Tool's GRASP software [14];
2. The Zernike polynomials are added to the original elliptical shape of the lens in the GRASP environment
3. The total modified lens surface is export from GRASP as a step file
4. The step file is imported to the CST environment. The imported lens surface is shown in Fig. 5.10 within the CST environment.

In order to represent the same geometry analyzed in MATLAB, the lens itself is a lossless plastic with a relative permittivity of $\epsilon_r = 2.3$. In addition, a lossy plastic material with a relative permittivity of ϵ_r and a loss tangent of $\delta_{tan} = 0.001$ are added to the lens lateral sides as an absorber (see Fig. 5.10). Finally, a PEC layer is added on top of the dielectric box to remove the effect of side radiation in the CST simulation (see Fig. 5.10).

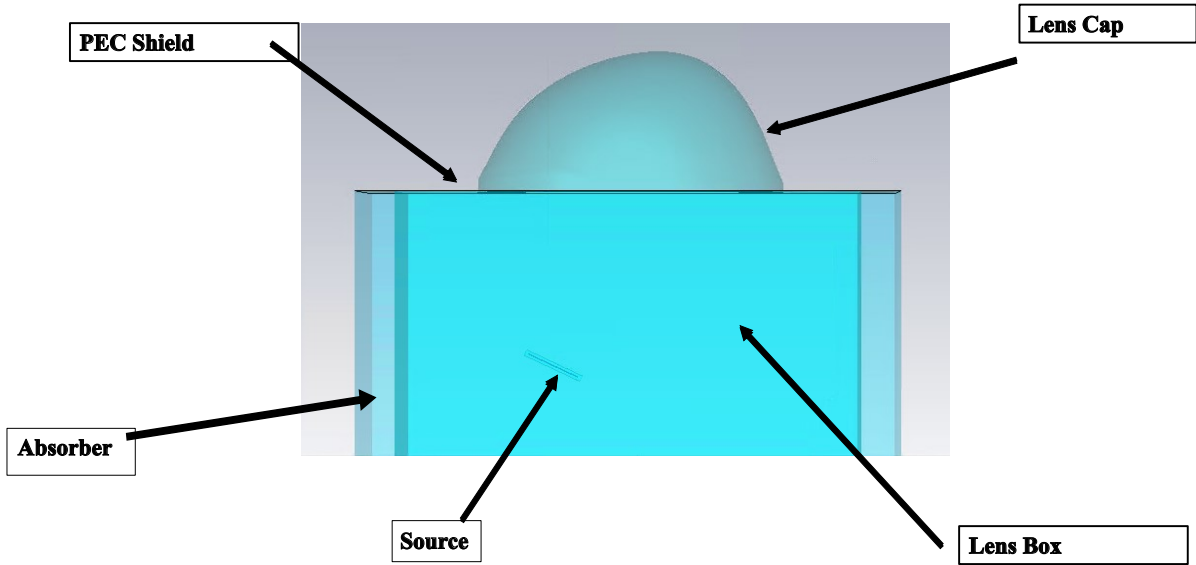


Figure 5.10: The optimized lens antenna geometry exported to the CST environment.

The antenna feed was modeled in CST using the imported source option. In this case, the source is a Huygens' source with a Gaussian taper. Where the Huygens' source is defined as

$$|\vec{J}| = e^{-\left(\frac{\rho^2}{\omega_0^2}\right)} \quad (5.1)$$

and ω_0 is defined as

$$\omega_0 = \sqrt{\frac{8.868 D_f}{T_e}} \quad (5.2)$$

where T_e is the taper level, and D_f is the diameter of the feed (see Fig. 5.11). The characteristics of a Huygens' source are as follows:

1. $|\vec{M}| = \zeta |\vec{J}|$
2. $\vec{M} \cdot \vec{J} = 0$
3. $\vec{J} \times \vec{M} = \hat{z}$

The imported CST source modeling the described Huygens' source is shown in Fig. 5.11. To model a tilted feed, this imported source is rotated with respect to the axis of the lens component. The E- and H-plane cuts of this far field are shown in Fig. 5.12 where the z-axis of the far field is rotated to the tilt angle as marked in Fig. 5.10. The 3D pattern of the feed is shown in Fig. 5.13.

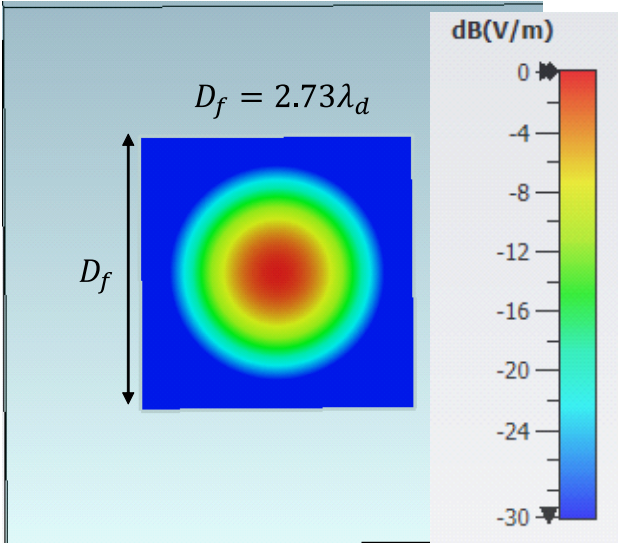


Figure 5.11: The designed feed in CST.

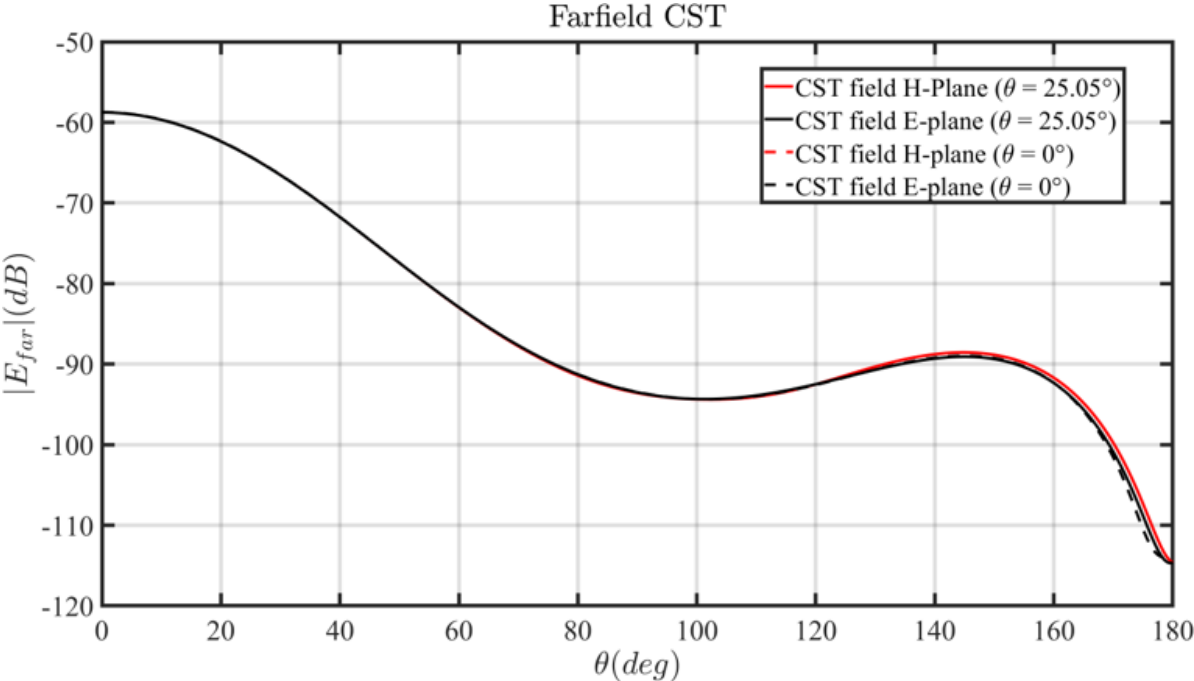


Figure 5.12: The radiated far field of the Huygens' source implemented in CST.

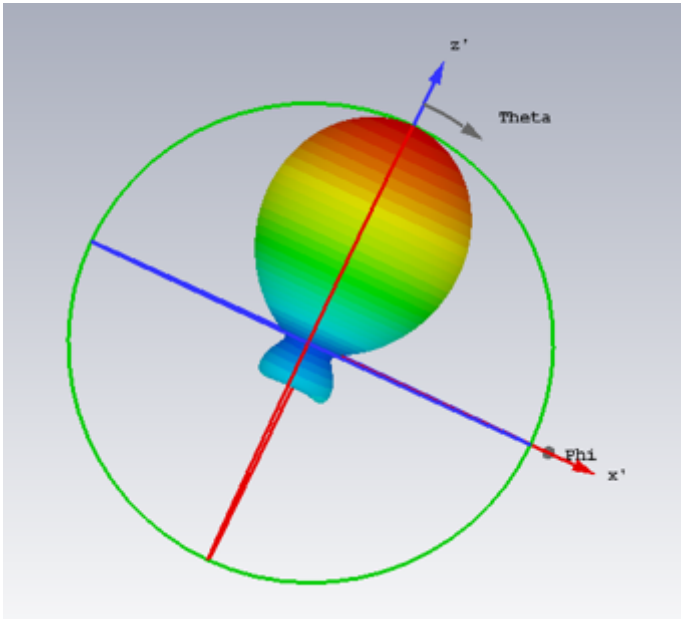


Figure 5.13: The 3D pattern of the feed.

5.2.2. Results: Optimizer vs. Full Wave Simulator

Fig. 5.14 and Fig. 5.15 show the far field patterns of the optimized lens antenna compared to the results obtained using the MATLAB based analysis for the H- and E-plane cuts, respectively. What can be observed is a very good main lobe match. In addition, the pointing angles are in agreement as well. The sidelobe levels differ with approximately 2 dB.

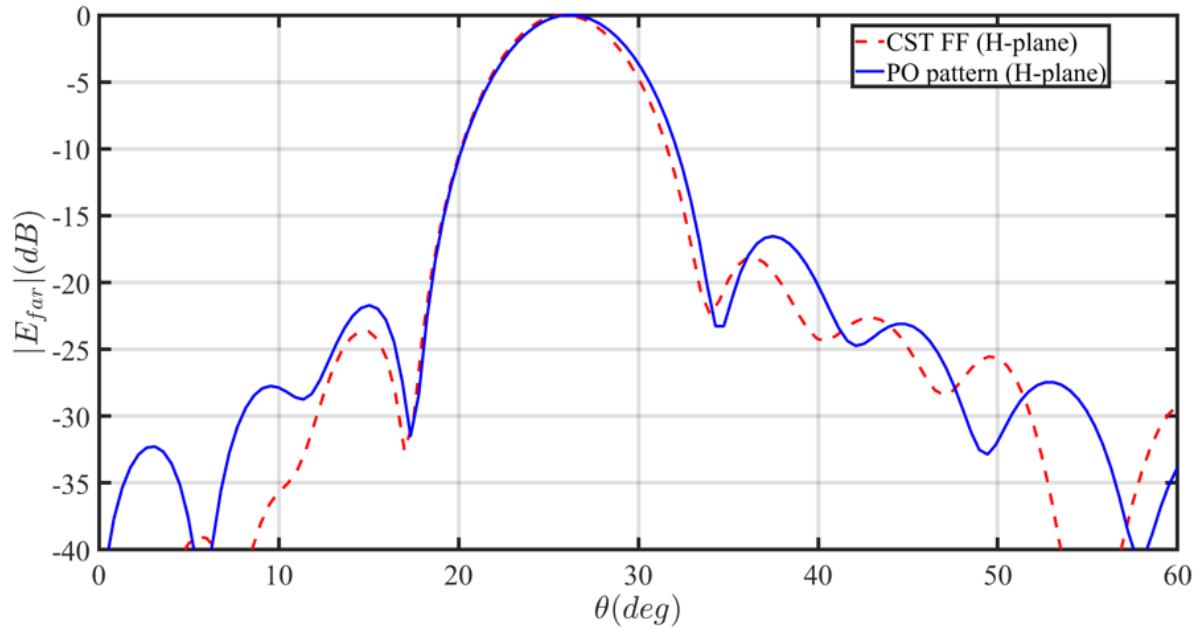


Figure 5.14: The H-plane of the radiated far field from CST versus the H-plane of the radiated far field from the optimizer.

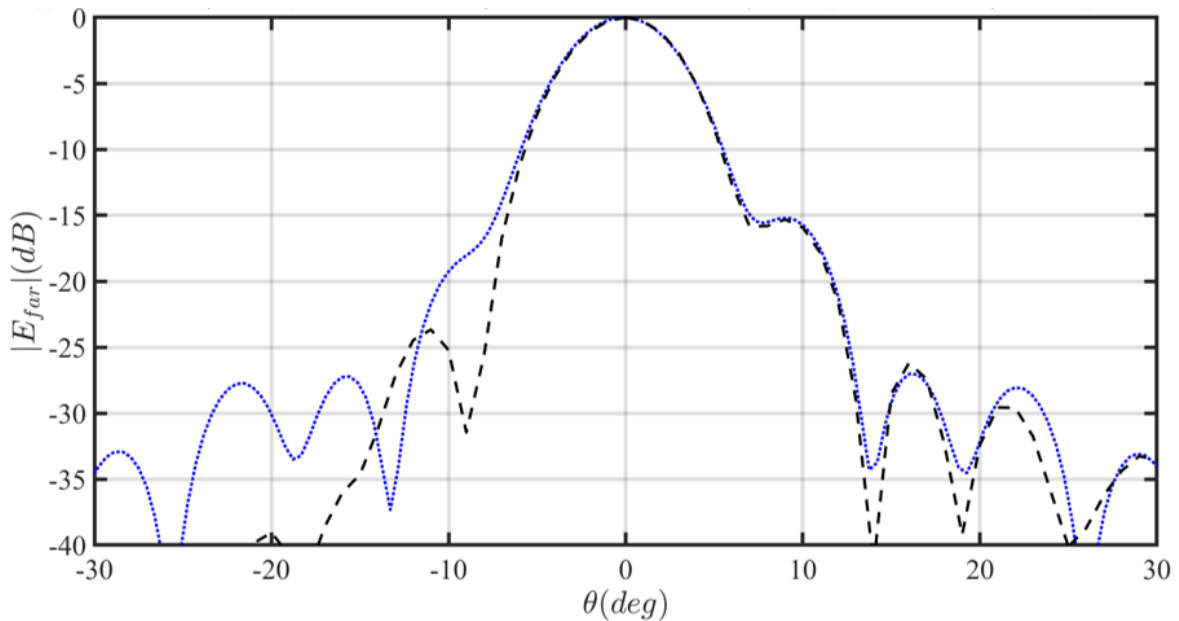


Figure 5.15: The E-plane of the radiated far field from CST versus the E-plane of the radiated far field from the optimizer.

Table 5.11 shows the comparison of the performance metrics of the optimized lens antenna using CST and the MATLAB based analysis in transmission. What can be observed is that the CST results are slightly better than the results of the MATLAB simulation. The primary reason for this small discrepancy is how the transmitted fields are modeled in the critical angle region of the lens in the MATLAB based code. Specifically, in this region, the analysis code assumes that no transmitted field is present;

however, in a full wave simulation, higher order field effects are included in the critical angle region of the lens.

Table 5.11: CST versus optimizer results

	CST	Optimizer
Directivity (dB)	28.9	28.7
Gain (dB)	28.3	28.1
SLL (dB)	-18.2	-16.5
η_{rad}	0.87	0.87
η_t	0.78	0.75
η	0.68	0.65
Scan loss (dB)	-0.71	-0.89

5.3. Bandwidth performance of the proposed shaped lens antennas

Since the conjugate field matching of the transmitted and incident fields in the described analysis in reception method is frequency dependent, an important step to consider in designing a shaped lens antenna is its bandwidth performance. As a result, the focus of this subsection is to determine the bandwidth performance of such shaped lens antennas. This is relevant because the surface modification is limited by the upper and lower bounds of the Zernike coefficients, as discussed in Chapter 4.

Fig. 5.16 shows the bandwidth performance of the optimized shaped lens antenna that was described in section 5.1. For this analysis, the same Gaussian feed is assumed over the entire bandwidth. Therefore, the only limit should come from the lens focusing properties. In addition, all the optimized parameters and the geometry of the lens antenna are fixed at the central frequency (180 GHz), and the geometry is analyzed in terms of the efficiency terms and far field patterns over a 130 – 230 GHz bandwidth. This frequency range is chosen to be similar to the one of the lens antenna design in [2], where the bandwidth was ultimately limited by the matching performance of the antenna feed into a waveguide port.

In this figure, the maximum achievable theoretical directivity, which is also known as the diffraction limited directivity, is shown. The directivity and gain of the shaped lens antenna are also shown in this figure as a function of the frequency. As expected, the directivity and gain of the geometry increases with the operation frequency. The difference between the gain and the directivity (reflection efficiency) remains constant (≈ 1.7 dB). However, the difference between the diffraction limited directivity and directivity (field match efficiency) increases when the frequency increases.

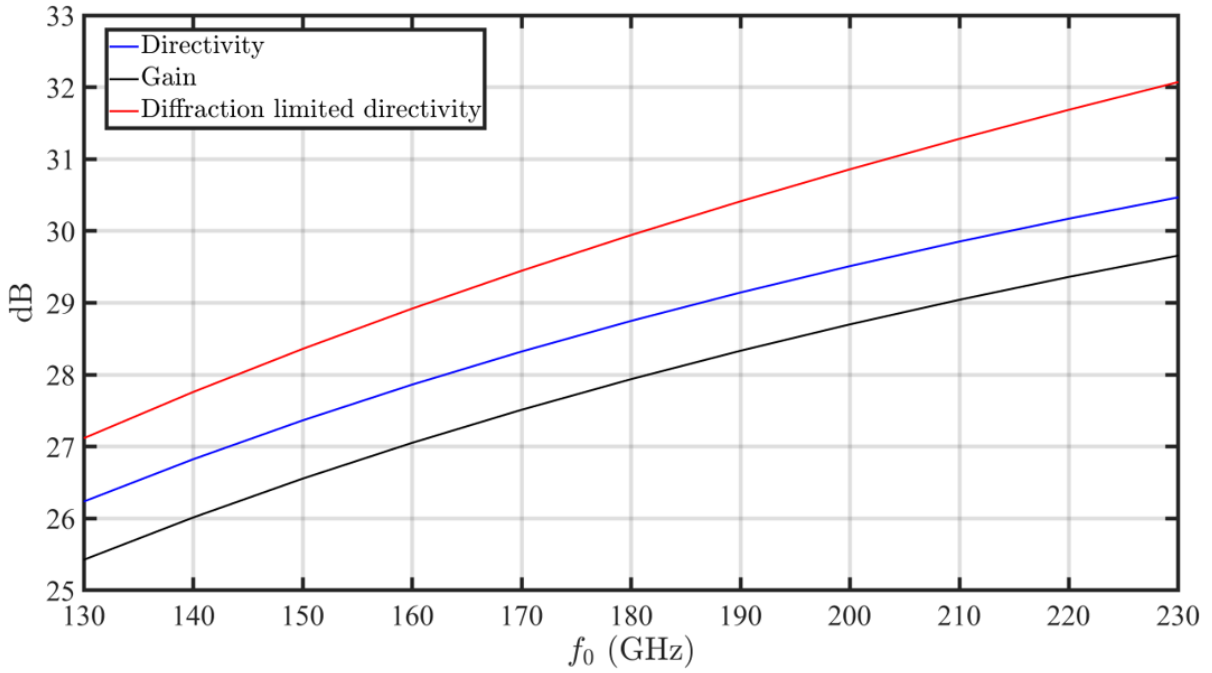


Figure 5.16: The bandwidth performance of the lens.

The total time elapsed for the MATLAB based optimization process is 90 minutes where the kernel code of the optimization process, i.e. the analysis in Rx, takes 2 seconds to elapse. On the other hand, the full wave validation of the optimized geometry took 371 minutes to complete. As a result, performing this type of optimization process using a full wave simulation would be an extremely time-consuming process. Both results were obtained using a single core Intel i5-9500 processor with a clock frequency of 3 GHz, and a RAM memory of 8 GB.

5.4. Scanning in the E- and D-plane

The previous results were obtained in the H-plane for 25° incident angle. However, it is also important to consider the performance of the optimization procedure in the E- and D-plane. The numerical results for the E-plane case are shown in Table 5.12. Fig. 5.17 shows the tangent incident and transmitted fields

Table 5.12: Optimized parameter results for the E-plane.

Parameter	Value
η	0.72
η_{ref}	0.84
η_{FM}	0.83
Directivity (dB)	34.1
Gain (dB)	33.31
SLL (dB)	-12.2
Scan Loss (dB)	-0.77

on the lens surface in both amplitude and phase for the E-plane case. With the achieved tilt, it can be observed that the radiation is pointed towards the top half of the lens. The total efficiency has decreased, and the side lobe level is also worse compared to the H-plane case (see Fig. 5.18).

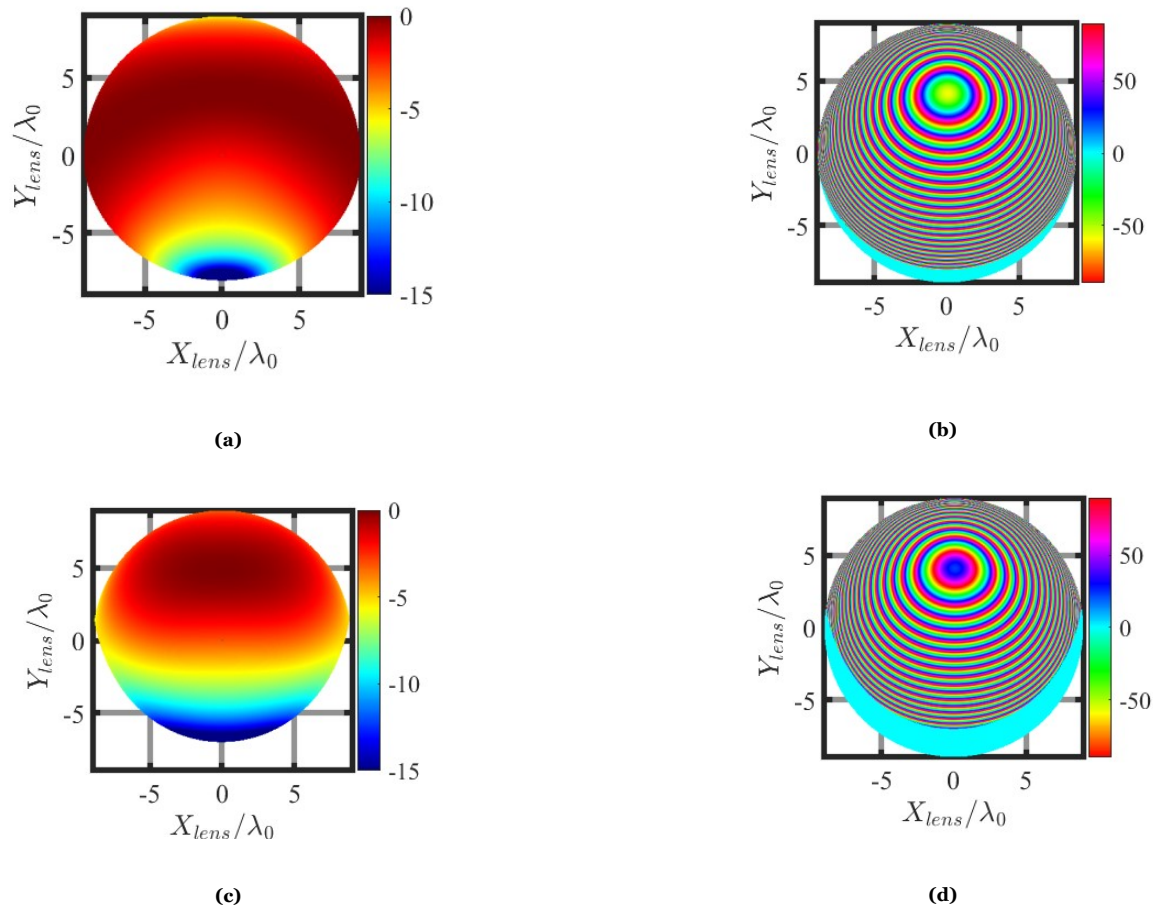


Figure 5.17: The tangent incident (a,b) and transmitted (c,d) fields on the lens surface in 2D in both amplitude and phase for the E-plane

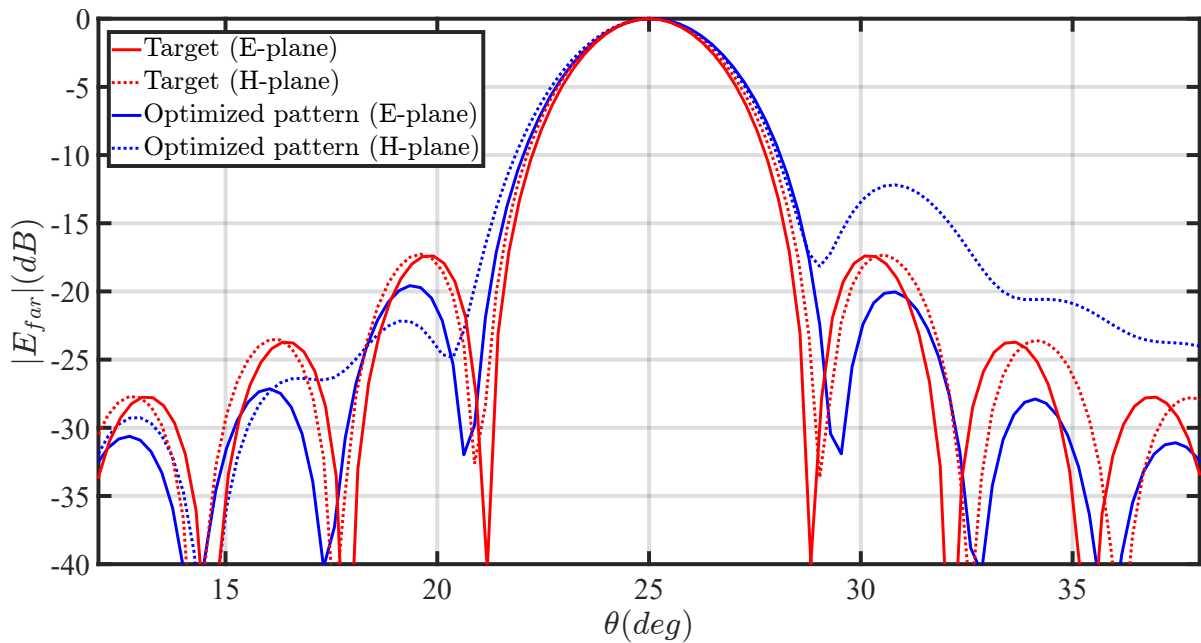


Figure 5.18: The radiated far fields for the target and the optimized lens antenna for a scanning case of 25° in the E-plane.

Table 5.13 shows the optimization results for the D-plane case. The total efficiency has decreased even more, however, the side lobe level is better. This improved side lobe level is due to the increased field match efficiency. The scan loss is also slightly lower in this case. Therefore, it is most difficult to perform the optimization in the D-plane. However, the optimizer appears to show consistent performance for the three different cases. Fig. 5.19 shows similar fields, however, now they are shown for the D-plane.

Table 5.13: Optimized parameter results for the D-plane.

Parameter	Value
η	0.66
η_{ref}	0.76
η_{FM}	0.87
Directivity (dB)	34.2
Gain (dB)	33
SLL (dB)	-16
Scan Loss (dB)	-1.1

Again, it can be observed that feed is properly tilted in the correct direction for a D-plane scanning case. Furthermore, the radiated far fields are shown in Fig. 5.20.

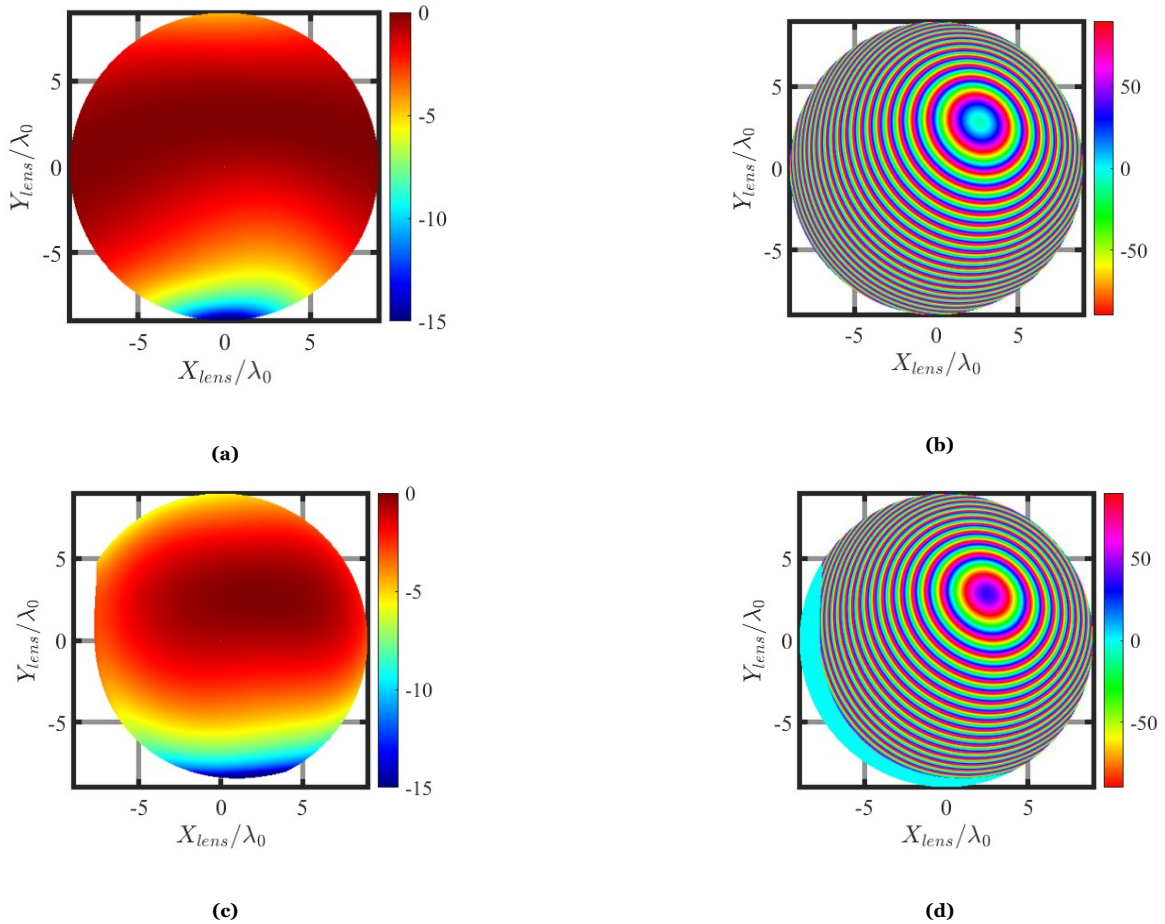


Figure 5.19: The tangent incident (a,b) and transmitted fields (c,d) on the lens surface in 2D in both amplitude and phase for the E-plane

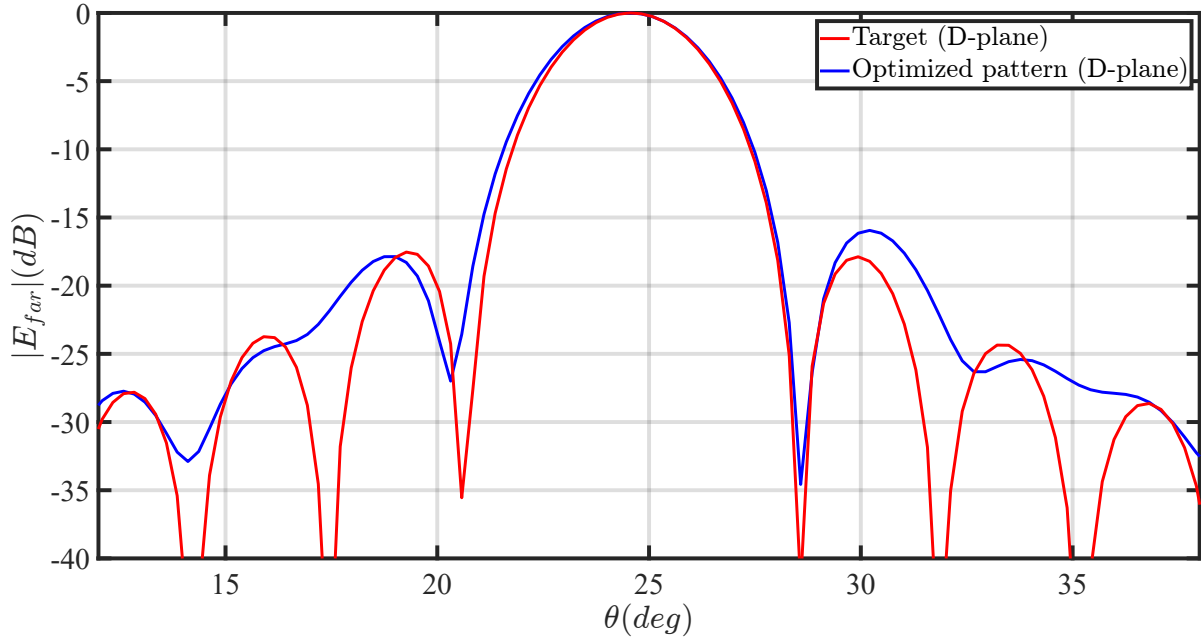


Figure 5.20: The radiated far fields for the target and the optimized lens antenna for a scanning case of 25° in the D-plane.

5.5. Testing the theoretical scanning performance of plastic lens antennas

As mentioned in the introduction of Chapter 2, plastic lenses are commercially viable candidates for the next generation of communication systems, operating at frequencies above 100 GHz. However, the canonical elliptical lenses made in plastic are fundamentally limited in scanning capabilities, due to their curvature [1]. In this section, the scanning capabilities of shaped plastic lenses are explored to determine the possible performance increase by changing the shape from the canonical one. The two explored cases are a 45° scanning case and a 60° scanning case in the H-plane. The relevant parameters for these scanning cases are listed as follows:

- Frequency of operation: $f = 180$ GHz
- Lens diameter: $D = 18\lambda_0$
- Permittivity of the material: $\varepsilon_r = 2.3$
- Incident plane wave angle: $\theta_{pw}^i = 45^\circ, 60^\circ; \phi_{pw}^i = 0^\circ$

5.5.1. 45 degree scanning scenario

Table 5.14 shows the optimized parameters. In this case, the Zernike expansion of order 4, is considered to modify the lens shape. Moreover, since the required optimization goal is more complicated to achieve, the optimization time has been increased to $t_{opt} = 90$ minutes.

Table 5.14: Optimized parameter results.

Parameter	Value
$f_\#$	0.91
Δx	$-8.09\lambda_0$
θ_{tilt}	41.2°
Δz	$3.73\lambda_0$

Fig. 5.21a shows the ray tracing in transmission with the shaped lens. The blue rays correspond to the incident field and the green rays correspond to the transmitted field. A significant shadow region is present on the lens. Fig 5.21b shows the added surface modification Δs .

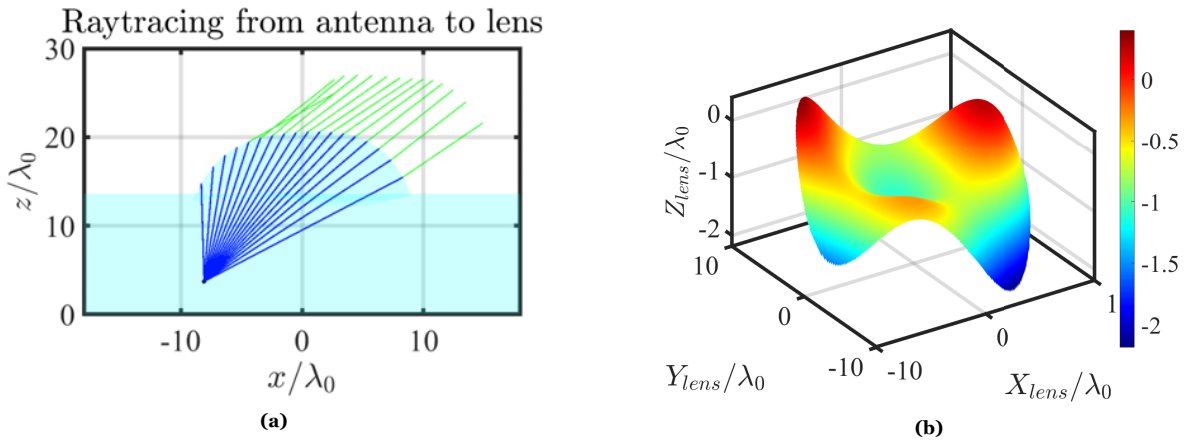


Figure 5.21: The ray tracing plot for the 45° scanning case (a) and the added surface Δs of the modified lens (b).

Fig. 5.22 shows the tangent fields on the lens surface. With Fig. 5.22a showing the tangent incident fields and Fig. 5.22b shows the transmitted fields.

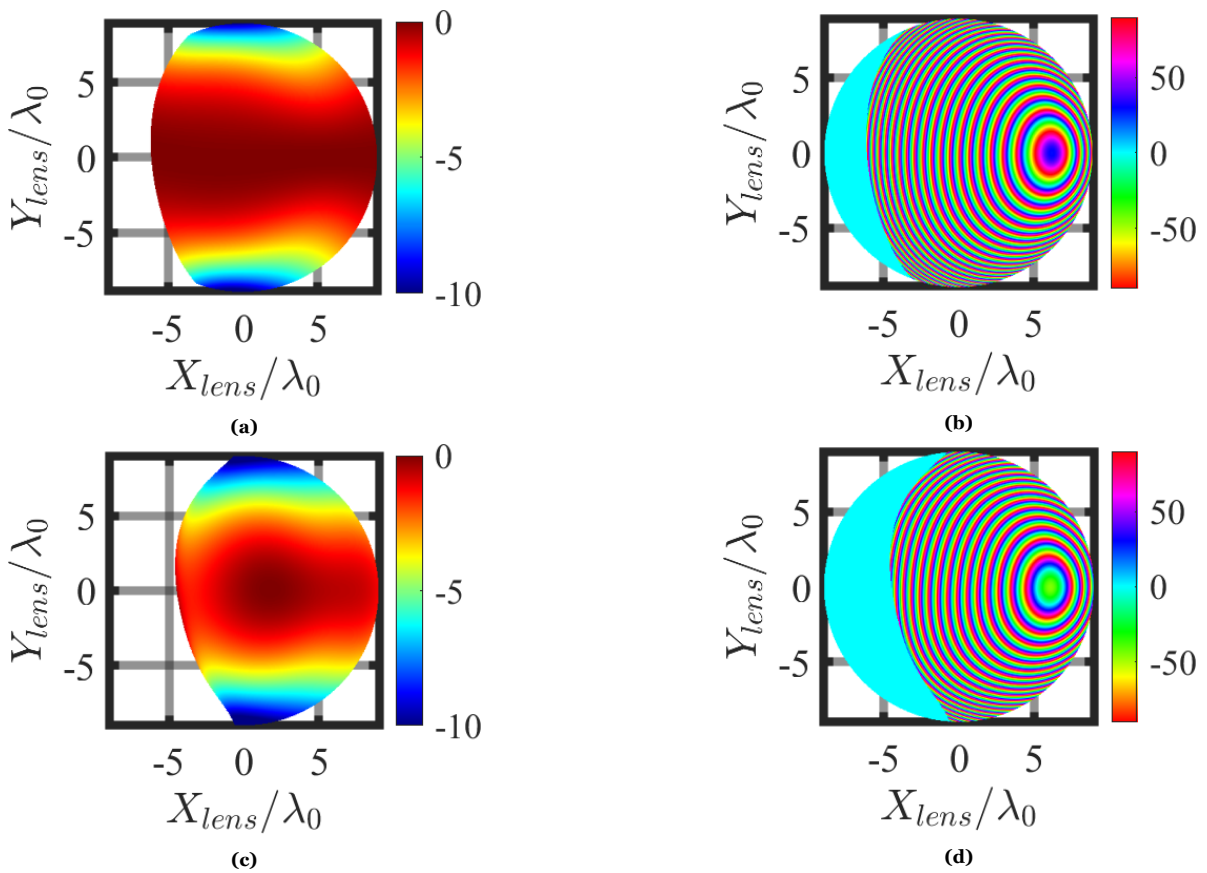


Figure 5.22: The tangent incident (a,b) and transmitted (c,d) fields on the lens surface in 2D in both amplitude and phase

Fig. 5.23 shows the far field patterns of the lens antenna in both the E- and H-plane. There is some asymmetry in the pattern, which is most likely due to the asymmetry of the Zernike surface expansion.

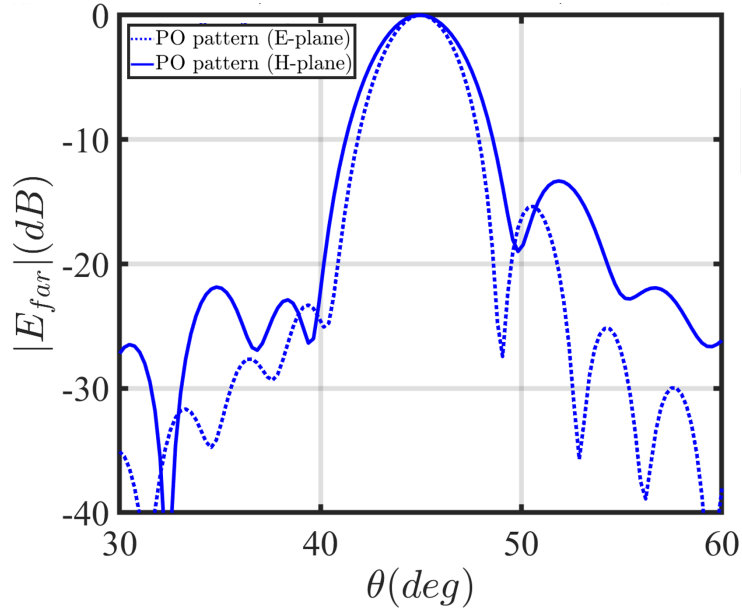


Figure 5.23: Far field pattern for the 45° case

Table 5.15 shows the directivity, side lobe level, gain and scan loss related for a 45° scanning case. The total efficiency is also shown.

Table 5.15: The performance metric of the optimized lens antenna for a 45° scanning case, obtained using the MATLAB based analysis code.

Parameter	Value
Directivity (dB)	33.0
SLL (dB)	-12.2
Gain (dB)	31.9
Scan loss (dB)	-2.2
η	0.48

5.5.2. 60 degree scanning scenario

Table 5.16 shows the optimized parameters. Again, the Zernike expansion of order 4, is considered to modify the lens shape. However, the optimization time has been increased to $t_{opt} = 120$ minutes, since the required optimization goal is even more complicated to achieve compared to the optimization goal for the 45° scanning scenario.

Table 5.16: Optimized parameter results.

Parameter	Value
$f_{\#}$	0.85
Δx	$-11.26\lambda_0$
θ_{tilt}	54.3°
Δz	$4.36\lambda_0$

Fig. 5.24a shows the ray tracing with the shaped lens. Once more, the blue rays correspond to the incident field and the green rays correspond to the transmitted field. As expected, the shadow region

is even larger. Fig. 5.24b shows the added surface modification Δs .

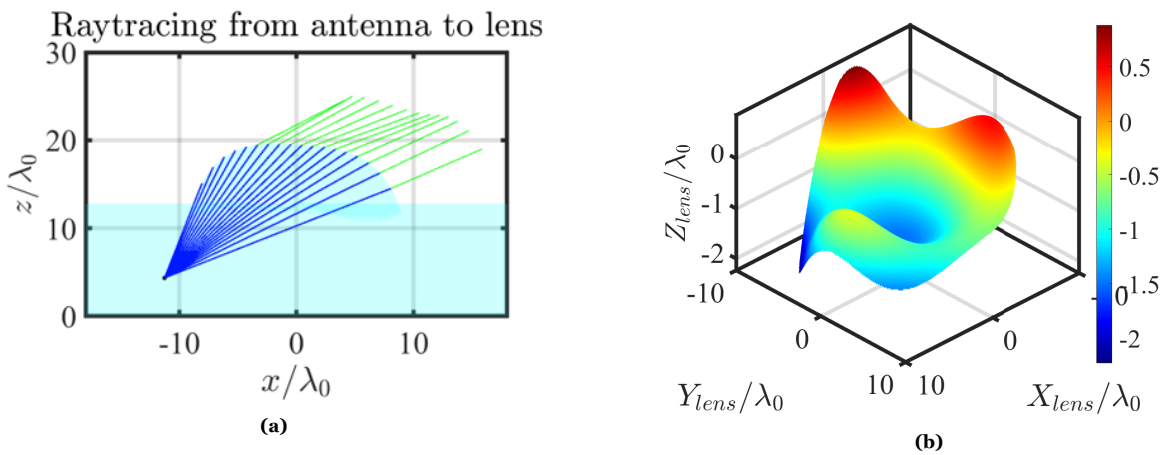


Figure 5.24: The ray tracing plot for the 60° scanning case (a) and the added surface Δs of the modified lens (b).

Fig. 5.25 shows the tangent fields on the lens surface.

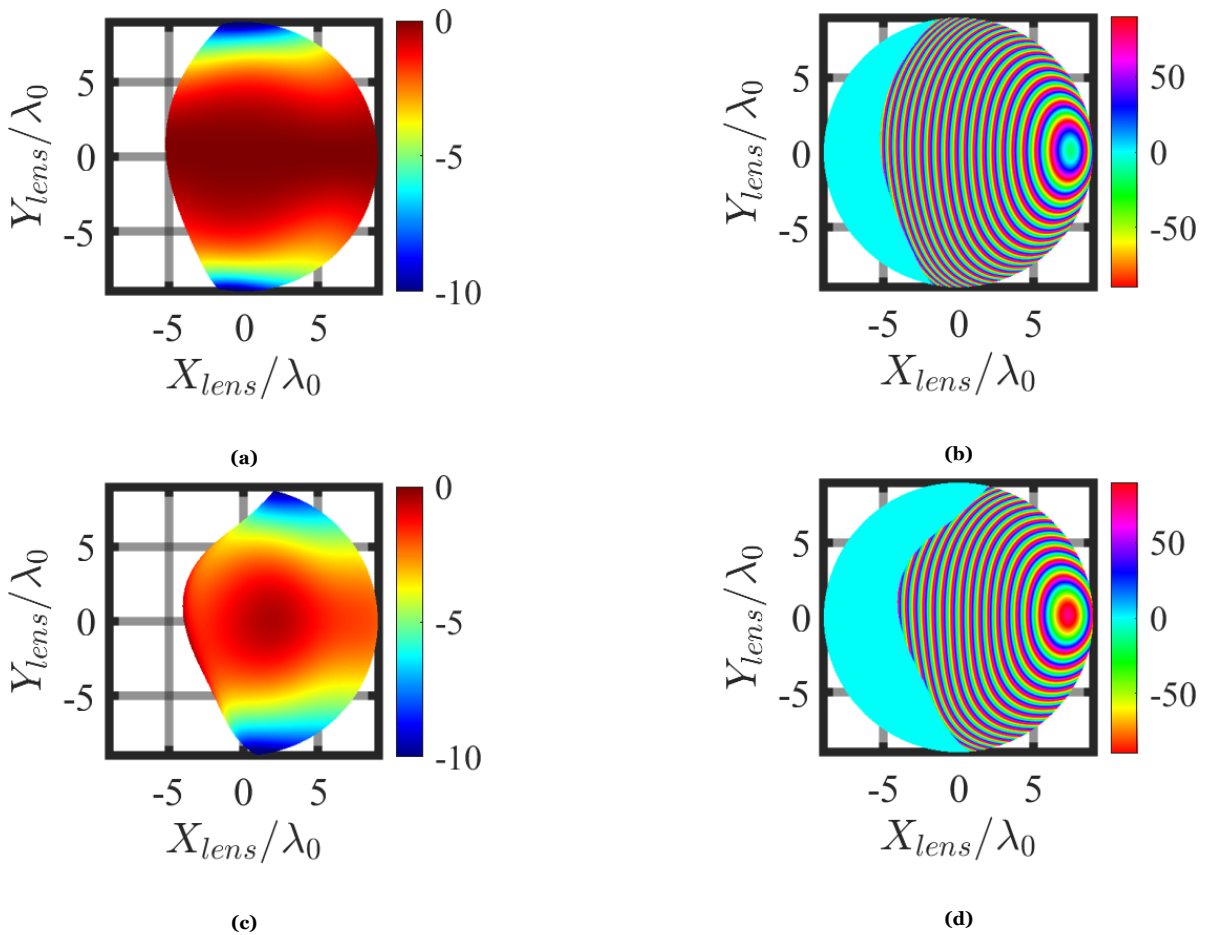


Figure 5.25: The tangent incident (a,b) and transmitted (c,d) fields on the lens surface in 2D in both amplitude and phase

Fig. 5.26 shows the far field patterns of the lens antenna in both the E- and H-plane. Table 5.17 shows the directivity, side lobe level, gain and scan loss related for a 60° scanning case. The total efficiency is also shown.

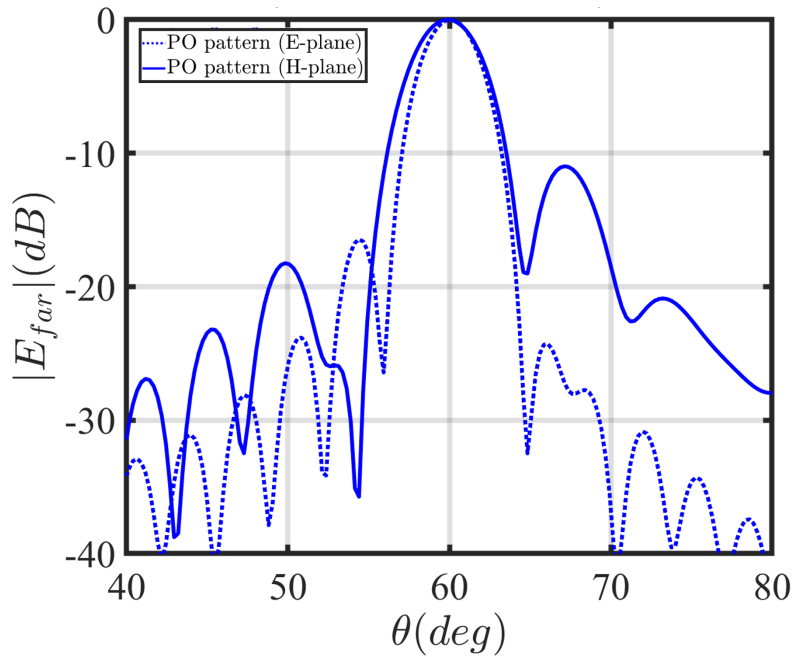


Figure 5.26: Far field pattern for the 60° case.

Table 5.17: The performance metric of the optimized lens antenna for a 60° scanning case obtained using the MATLAB based analysis code.

Parameter	Value
Directivity (dB)	32.9
SLL (dB)	-11.0
Gain (dB)	31.3
Scan loss (dB)	-2.8
η	0.42

5.5.3. Scan loss versus scan angle

Fig. 5.27 shows the scan loss versus the scan angle. As can be seen, the synthesis of shaped lens antennas using the proposed optimization process can theoretically achieve scan losses of < 3 dB for scanning angles up to 60°.

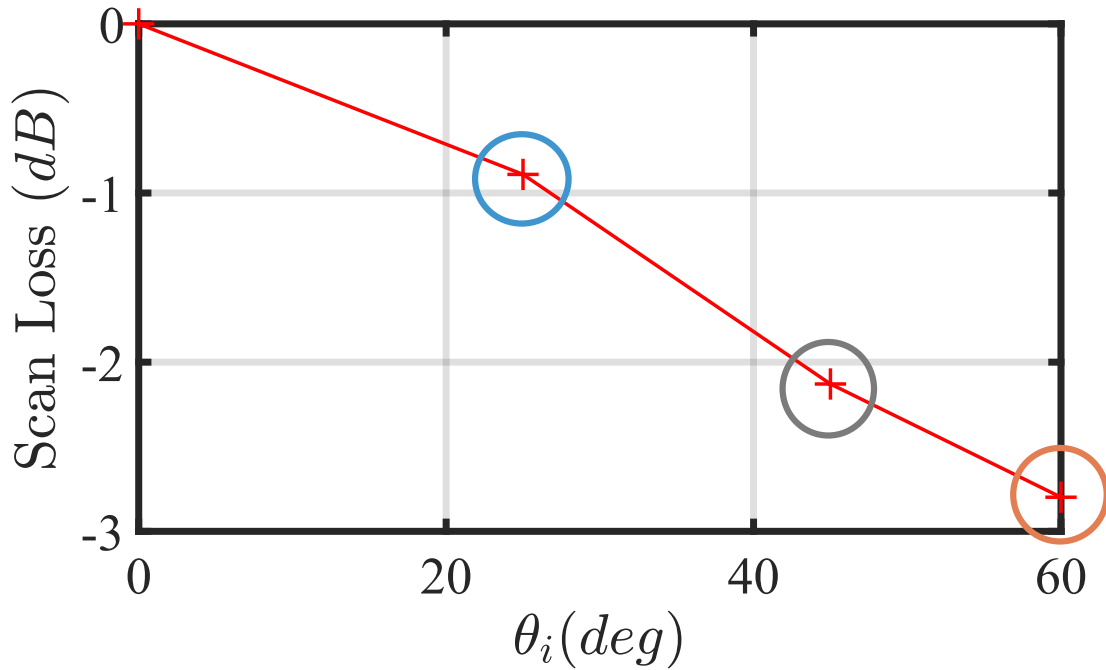


Figure 5.27: Scan loss versus scan angle.

A comparison can be made of the lens surfaces for the three considered scanning cases. This allows us to evaluate how the surface changes when the scan angle increases. Fig. 5.28 shows the lenses obtained by the optimizer. What can be observed is that the lens surface becomes flatter for larger scan angles. In conclusion, it is shown that it is theoretically possible to enhance the scanning performance of plastic lens antennas by moving away from a canonical elliptical shape. It is worth noting that the overall optimization process is significantly more complex for plastic lenses compared to lenses made out of denser materials. As a result, the proposed methodology also holds for such denser lens geometries while requiring a less complex shape modification and smaller feed tilt tangles because of the shallower curvature of such lenses.

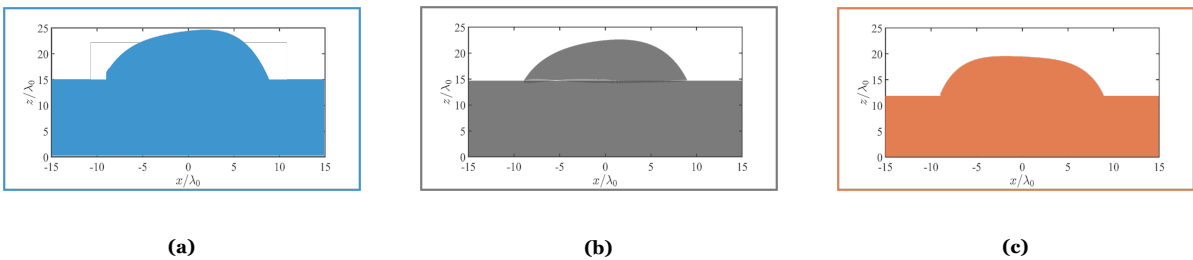


Figure 5.28: The shaped lenses for the 25°, 45° and 60° case, respectively.

6

Multi lens analysis

Recently, large Field of View (FoV) sensing systems and sub-mm imaging systems are demonstrated. Several applications benefit from a large available bandwidth, from security [9] imaging systems to astronomical spectrometers [11]. Multiple pixels working simultaneously can decrease the image acquisition time. It is therefore important to develop Quasi-Optical (QO) systems that are capable of achieving wide band and wide scanning. Most of these systems consist of multiple QO components, and there exist PO based methods that are capable of analysing these multi QO component chains. However, these methods are oftentimes extremely time-consuming. Therefore, the objective of this chapter is to implement an efficient method to analyse said multi QO component chains. In addition, this time efficient method can be used as a kernel for an optimizer similar to the one discussed in Chapter 3.

The developed method combines ray tracing techniques with a cascaded Geometrical Optics (GO) technique, thereby allowing for a less time-consuming analysis of the multi QO component chains. In previous works, multi-lens components were studied using a single transmitting surface GO and simple geometrical approximations were considered to use this propagation technique for multi transmitting surfaces. However, in this work, an accurate multi surface GO method is implemented where off-axis performance of the QO system is accurately evaluated.

This chapter explains the analysis of multi QO component chains. Firstly, the QO setup is introduced, and the components are parametrized. Secondly, the analysis of the system in reception and transmission mode is explained. Thirdly, the ray tracing method is discussed. Afterwards, the GO method for multi layer lenses is introduced. In addition, the codes are validated using a Physical Optics approach and a few example cases are discussed.

6.1. Multi lens example scenario

In this work, an example case as shown in Fig. 6.1 is considered. In this example case, a silicon extended hyper-hemispherical lens (blue) and a plastic hyperbolic lens (green) as shown in Fig. 6.1 are analyzed.

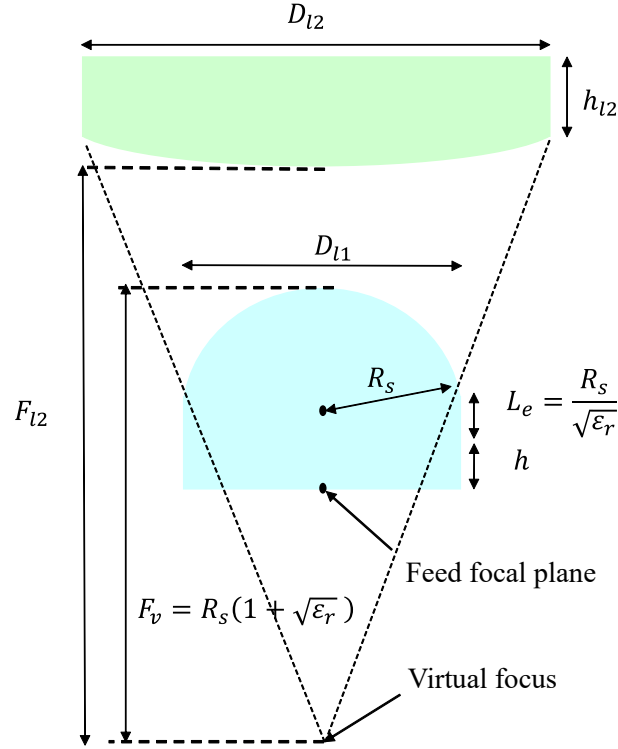


Figure 6.1: Dual lens setup with the silicon hyper-hemispherical lens shown in blue and the plastic hyperbolic lens shown in Green

The considered feed is the Gaussian feed as described in Chapter 2. However, for this application, the feed has a -11 dB taper at 45° . The centre frequency for this example case is $f_c = 480$ GHz.

The specifications of the extended hyper-hemispherical lens are as follows

- The relative permittivity of the lens $\epsilon_r = 11.9$
- The diameter of the lens $D_{l1} = 48\lambda_0$
- The focal length of the lens $F_v = 106.8\lambda_0$

where λ_0 is the free space wavelength.

The specification of the hyperbolic lens are

- The relative permittivity of the lens $\epsilon_r = 2.4$
- The diameter of the lens $D_{l2} = 82.3\lambda_0$
- The focal length of the lens $F_{l2} = 164.6\lambda_0$
- The thickness of the lens $h_{l2} = 28\lambda_0$

6.1.1. Lens parametrization

As mentioned, the two canonical QO components that are analysed in this section are the hyper-hemispherical lens antenna and the hyperbolic lens antenna. Similar to Chapter 2, a lens parametrization procedure is applied to these QO components. In addition, the derivatives are given, which are needed for the calculation of the normal vector and the Jacobian.

Hyper-hemispherical lens

The z coordinates of the hyper-hemispherical surface are calculated as follows:

$$z_{lens} = L_e + h + \sqrt{R_s^2 - (x_{lens}^2 + y_{lens}^2)} \quad (6.1)$$

where the extension length $L_e = \frac{R_s}{\sqrt{\varepsilon_r}}$; $h = F_v - R_s - L_e$, with F_v being the virtual focus; x_{lens} and y_{lens} are the surface locations of the lens in the ρ plane. For an arbitrary point Q^{hh} on the hyper-hemispherical lens surface the locations in x , y and z are defined as

$$Q_x^{hh} = x \quad (6.2a)$$

$$Q_y^{hh} = y \quad (6.2b)$$

$$Q_z^{hh} = L_e + h + \sqrt{R_s^2 - (x^2 + y^2)} \quad (6.2c)$$

The partial derivatives with respect to x and y are defined as

$$\frac{\partial Q_x^{hh}}{\partial x} = 1 \quad (6.3a)$$

$$\frac{\partial Q_y^{hh}}{\partial x} = 0 \quad (6.3b)$$

$$\frac{\partial Q_z^{hh}}{\partial x} = \frac{-x}{\sqrt{R_s^2 - (x^2 + y^2)}} \quad (6.3c)$$

and

$$\frac{\partial Q_x^{hh}}{\partial y} = 0 \quad (6.4a)$$

$$\frac{\partial Q_y^{hh}}{\partial y} = 1 \quad (6.4b)$$

$$\frac{\partial Q_z^{hh}}{\partial y} = \frac{-y}{\sqrt{R_s^2 - (x^2 + y^2)}} \quad (6.4c)$$

respectively.

Hyperbolic lens

The surface of a hyperbolic lens antenna can be expressed in terms of Cartesian coordinates, as follows

$$\frac{(z_{hyp} - c)^2}{a^2} - \frac{x_{hyp}^2 + y_{hyp}^2}{b^2} = 1 \quad (6.5)$$

where a is the semi-major axis; b is the semi-minor axis; c is the distance from the centre to a focus. These parameters are defined as:

$$a = \frac{F_{l2}}{1 + e} \quad (6.6)$$

$$b = \sqrt{c^2 - a^2} \quad (6.7)$$

$$c = a \cdot e \quad (6.8)$$

where F_{l2} is the focal length of the hyperbolic lens; e is the eccentricity of the hyperbolic lens, defined as $e = \sqrt{\varepsilon_{hyp}}$. The z coordinates of the hyperbolic surface can be calculated as follows

$$z_{hyp} = a \sqrt{1 + \frac{(x_{hyp}^2 + y_{hyp}^2)}{b^2}} + c \quad (6.9)$$

Similarly, for an arbitrary point Q^{hyp} on the hyperbolic lens surface the locations in x , y and z are defined as

$$Q_x^{hyp} = x \quad (6.10a)$$

$$Q_y^{hyp} = y \quad (6.10b)$$

$$Q_z^{hyp} = a \sqrt{1 + \frac{(x_{hyp}^2 + y_{hyp}^2)}{b^2}} + c \quad (6.10c)$$

The partial derivatives with respect to x and y are defined as

$$\frac{\partial Q_x^{hyp}}{\partial x} = 1 \quad (6.11a)$$

$$\frac{\partial Q_y^{hyp}}{\partial x} = 0 \quad (6.11b)$$

$$\frac{\partial Q_z^{hyp}}{\partial x} = \frac{\frac{ax}{b^2}}{\sqrt{1 + \frac{x^2+y^2}{b^2}}} \quad (6.11c)$$

and

$$\frac{\partial Q_x^{hyp}}{\partial y} = 0 \quad (6.12a)$$

$$\frac{\partial Q_y^{hyp}}{\partial y} = 1 \quad (6.12b)$$

$$\frac{\partial Q_z^{hyp}}{\partial y} = \frac{\frac{ay}{b^2}}{\sqrt{1 + \frac{x^2+y^2}{b^2}}} \quad (6.12c)$$

respectively.

6.2. Multi layer lens analysis

A similar approach can be taken as the one discussed in Chapter 3 to analyse and then optimize multi layer lenses. Again, one can perform the reaction integral defined as

$$V_{oc}I_{tx} = \iint_S (\vec{H}_{inc} \cdot \vec{M}_{tx}^{flat} - \vec{E}_{inc} \cdot \vec{J}_{tx}^{flat}) dS \quad (6.13)$$

over an induction surface taken at the top of the multi layer structure (see Fig. 6.2). Here \vec{H}_{inc} and \vec{E}_{inc} are the incident magnetic and electric fields, which can be defined as described in Chapter 3; \vec{M}_{tx}^{flat} and \vec{J}_{tx}^{flat} are the transmitted equivalent currents on the surface generated by the multi layer lens feed. Fig. 6.2 shows the two lenses and the surface s^+ where the reaction integral is performed.

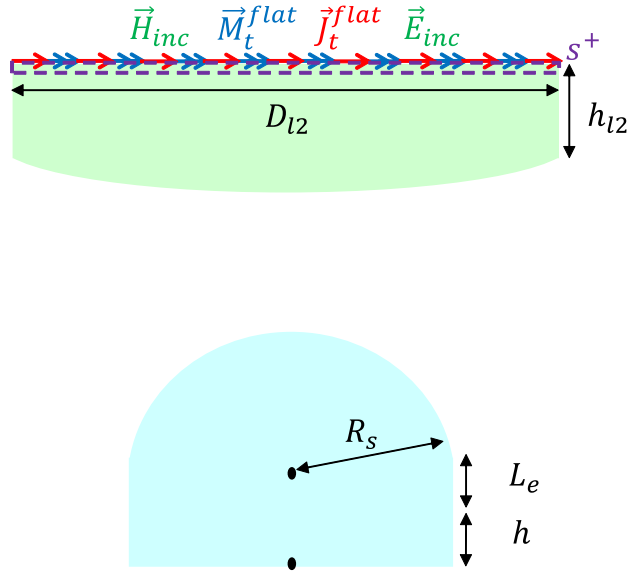


Figure 6.2: The enclosed surface s^+ where the reaction integral is performed.

To determine the equivalent magnetic and electric currents on the surface, a code is developed that combines ray tracing and a cascaded GO method. The next section explains these methods.

6.2.1. Ray tracing for multi layer components

As mentioned in the introduction of this chapter, an efficient multi surface GO code is implemented to compute the fields through multiple lens surfaces. In order to determine the progressive phase and amplitude spreading using a GO method, a ray tracing technique is needed to determine the propagation distance of each ray that travels through the multi lens surface. For this, a forward ray tracing method is applied, and the ray tracing procedure is subdivided into three separate parts.

1. From the feed to the lens surface of the hyper-hemispherical lens
2. From the hyper-hemispherical lens to the hyperbolic lens
3. From the hyperbolic lens to the flat extension

Fig. 6.3 shows an illustration of the steps as previously discussed, and this procedure is explained step by step in the next subsections.

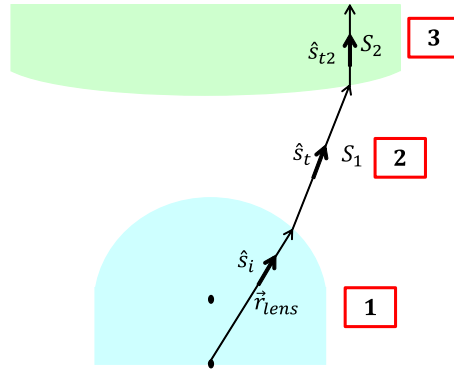


Figure 6.3: Schematic overview of the lens with its respective regions considered for the ray tracing procedure.

From feed to lens surface

The first part of the ray tracing method focuses on the propagation from the feed to the surface of the hyper-hemispherical lens. This approach is the same as the one taken in Chapter 3. Therefore, the propagation distance is defined as $|\vec{r}_{lens}|$ as shown in region 1 in Fig. 6.3.

From hyper-hemispherical lens to hyperbolic lens

The next step focuses on the propagation distance from the hyper-hemispherical lens to the hyperbolic lens, as shown in region 2 in Fig. 6.3. This propagation distance S_1 is determined by setting up and solving the general system of equations:

$$Q_2^x = Q_1^x + S_1 s_{tx} \quad (6.14a)$$

$$Q_2^y = Q_1^y + S_1 s_{ty} \quad (6.14b)$$

$$Q_2^z = Q_1^z + S_1 s_{tz} \quad (6.14c)$$

here Q_1^x , Q_1^y and Q_1^z represent the points on the surface of the hyper-hemispherical lens; Q_2^x , Q_2^y and Q_2^z represent the points on the surface of the hyperbolic lens; s_{tx} , s_{ty} and s_{tz} represent the components of transmission propagation vectors. As previously discussed, the z-locations of the hyperbolic lens can be calculated in terms of its x- and y- locations as shown in Eq. (6.9). Therefore, by substituting Eq. (6.14a) and Eq. (6.14b) into Eq. (6.14c), the ray tracing system of equations is reduced to the following quadratic equation

$$\left[\frac{a^2}{b^2} (s_{tx}^2 + s_{ty}^2) - s_{tz}^2 \right] S_1^2 + \left[\frac{a^2}{b^2} (2s_{tx}^2 x_{hh} + 2s_{ty}^2 y_{hh}) - 2s_{tz}^2 z_{hh} \right] S_1 + \left[a^2 + \frac{a^2}{b^2} (x_{hh}^2 + y_{hh}^2) - z_{hh}^2 \right] \quad (6.15)$$

Therefore, the propagation distance S_1 is found by applying and solving the abc formula. Note that this formula gives two solutions, so it is important to select a feasible solution. This means a solution

that represents the forward propagation of the ray towards the upper hyperbola. The other solution represents a backward ray travelling to a hyperbola located at locations with negative z values, therefore, this solution is discarded.

From hyperbolic lens to the flat extension

Lastly, the propagation distance from the hyperbolic lens to the top of the flat extension has to be determined. This propagation distance S_2 is represented by region 3 in Fig. 6.3. The extension length h is known. The propagation vector in transmission is determined using Snell's law. Therefore, the S_2 is found by

$$S_2 = \frac{(Q_2^{z_{max}} + h) - Q_2^z}{s_{tz2}} \quad (6.16)$$

the points on the flat surface are determined by the following system of equations:

$$Q_3^x = Q_2^x + S_2 s_{tx2} \quad (6.17a)$$

$$Q_3^y = Q_2^y + S_2 s_{ty2} \quad (6.17b)$$

$$Q_3^z = Q_2^z + S_2 s_{tz2} \quad (6.17c)$$

An example of the resulting ray tracing picture is shown in Fig. 6.4.

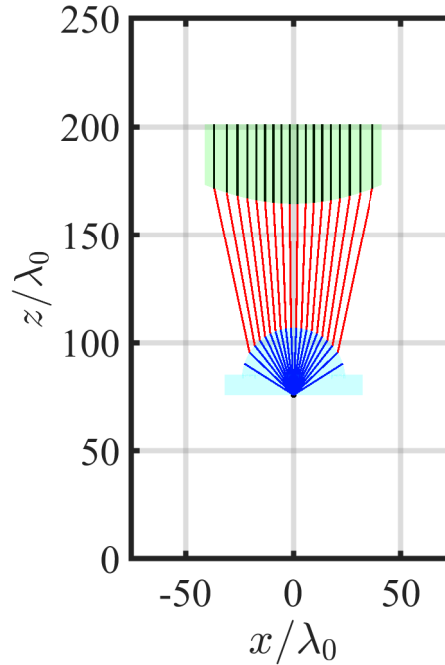


Figure 6.4: The result of the ray tracing procedure after steps 1 – 3.

6.2.2. Geometrical Optics for multi lens QO systems

To determine the field on the flat side of the hyperbolic lens as shown in Fig. 6.2, the field that is transmitted by the feed has to be propagated through multiple surfaces. Therefore, one can resort to a GO based code for multi transmitting surfaces. In this section, the general principle behind this GO analysis is explained. Firstly, the GO propagation in a homogeneous medium is discussed. Afterwards, the field interaction with transmitting surfaces is explained.

Geometrical optics propagation in a homogeneous medium

GO is a technique that is often used to determine wave propagation at high frequencies. The GO representation summarized in this chapter is based on derivations in [19]. This method is also known as ray optics, since the EM waves can be approximated as tubes of rays. First let us consider a generalized problem, where an EM propagation in a homogeneous medium is represented by a surface A_1 as shown

in Fig. 6.5. Such a wavefront is spherical for far field radiations, planar for plane wave radiations or cylindrical for cylindrical propagations (i.e. surface waves). In more general terms, this wavefront is defined as an astigmatic surface that has two radii of curvature ρ_1^i and ρ_2^i . The point P_0 is defined on the wavefront around the axial ray originating from point A .

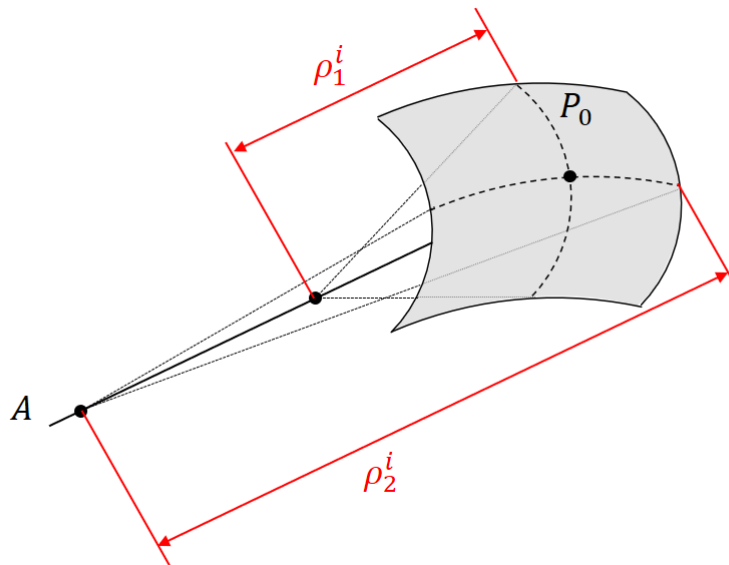


Figure 6.5: The primary wavefront A_1 .

Using a GO approximation, one can determine the amplitude and phase of this EM field when it is propagated a certain distance along its axial ray. To do so, the following two steps are taken:

1. Determine the secondary wavefront surface at a location along the axial ray.
2. Form a relation between the primary and secondary wavefront in terms of power density and field intensity.

Firstly, let us define an elementary area dA_1 of wavefront A_1 as shown in Fig. 6.6. This elementary area has the same radii of curvature as wavefront A_1 . The paraxial rays that form a tube of rays are found by considering the rays emerging from dA_1 .

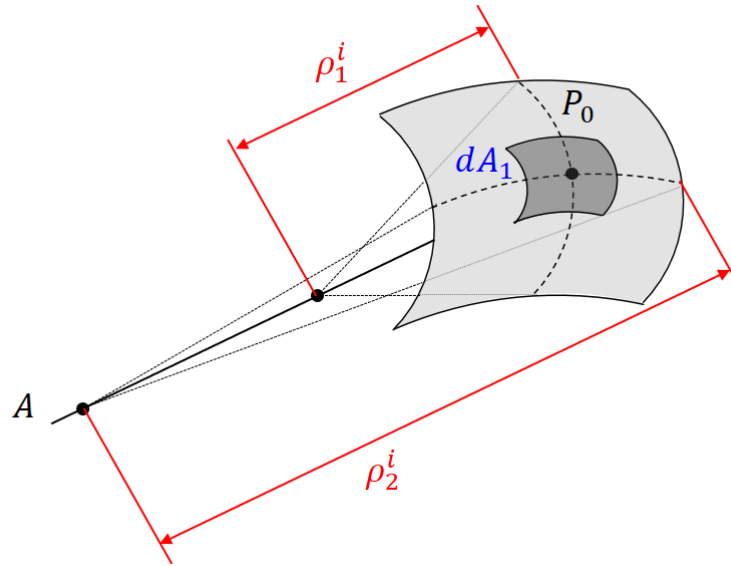


Figure 6.6: The elementary area around point P_1 defined as dA_1 .

Now, one can estimate the EM fields when the wavefront A_1 is propagated a certain distance S within the homogeneous medium. The secondary wavefront at distance S is shown in Fig. 6.7. An elementary surface surrounding the center point P can be defined as dA_2 .

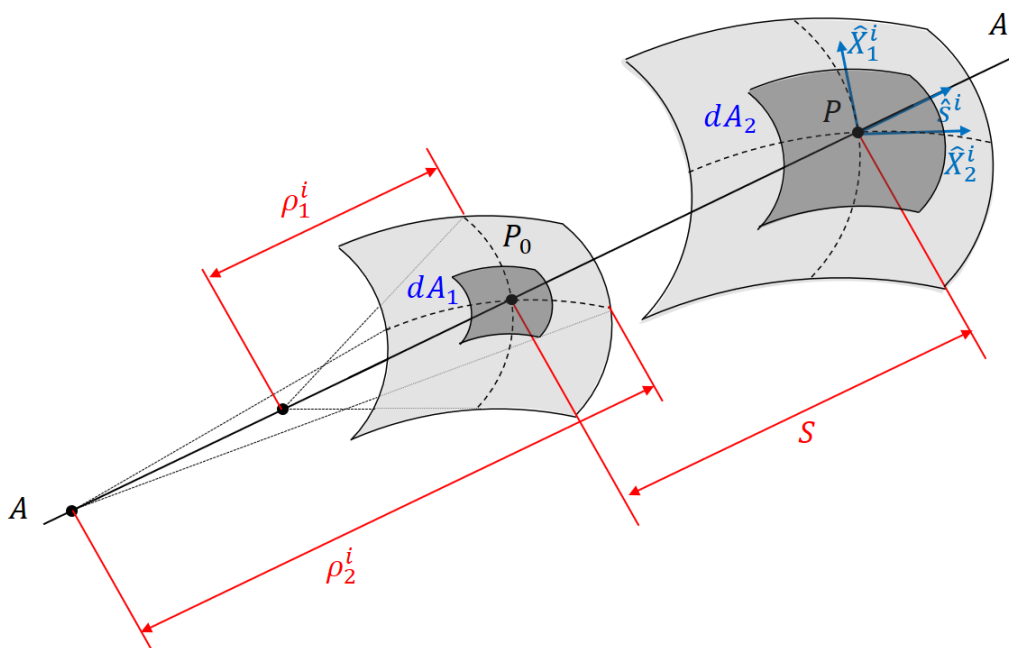


Figure 6.7: The secondary wavefront A_2 with its respective elementary area around point P defined as dA_2 .

As mentioned before, the direction of power flow is along the rays. Therefore, the principle of conservation of energy can be applied and the following relation holds:

$$|\vec{E}_1^i|^2 dA_1 = |\vec{E}_2^i|^2 dA_2 \quad (6.18)$$

where \vec{E}_1^i and \vec{E}_2^i are the electric field values in dA_1 and dA_2 , respectively. Equation 6.19 show the

relationship between the two elementary areas of the wavefronts in terms of their radii of curvature.

$$\frac{dA_1}{dA_2} = \frac{\rho_1^i \rho_2^i}{(\rho_1^i + S)(\rho_2^i + S)} \quad (6.19)$$

These relationships allow for an expression to be determined that expresses the incident field at the secondary wavefront in terms of the known incident field, as follows:

$$\vec{E}_2^i(P) = \vec{E}_1^i(P_0) \sqrt{\frac{\rho_1^i \rho_2^i}{(\rho_1^i + S)(\rho_2^i + S)}} e^{(-jk_1 S)} \quad (6.20)$$

where the exponent term signifies the progressive phase term, and k_1 is the propagation constant in the homogeneous medium. In addition, the propagation direction, which is along the axial ray, is represented by \hat{s}_i . The principal direction of the wavefront \hat{X}_1^i and \hat{X}_2^i are the unit vectors tangent to the two primary planes of the wavefront (see Fig.6.7). They have the following relation with respect to the incident propagation direction.

$$\hat{X}_1^i \perp \hat{X}_2^i \perp \hat{s}_i \quad (6.21)$$

Geometrical optics interaction with transmitting surfaces

After representing the propagation of EM fields inside a homogeneous medium, we would like to model the propagation of EM field through multiple lens surfaces using GO approximations. Therefore, it is necessary to analyze the interaction of GO fields with a transmitting surface. Let us assume that the field given by Equation 6.20 is incident upon a surface as shown in Fig. 6.8.

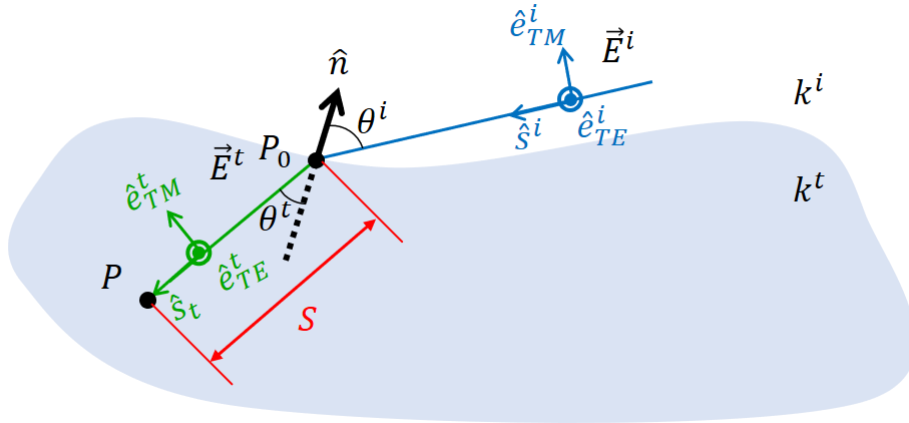


Figure 6.8: The field is incident upon a transmitting surface

The transmitted field can be written as

$$\vec{E}^t(S) = \vec{E}^i(P_0) \cdot \bar{\bar{\mathbf{T}}}(P_0) \sqrt{\frac{\rho_1^t \rho_2^t}{(\rho_1^t + S)(\rho_2^t + S)}} e^{(-jk_2 S)} \quad (6.22)$$

where $\bar{\bar{\mathbf{T}}}$ is the transmission dyad; ρ_1^t and ρ_2^t are the principal radii of curvature of the transmitted wavefront. In order to calculate the transmission dyad using available Fresnel coefficients, a coordinate system based on TE and TM polarizations is desired. This coordinate system $(\hat{s}^i, \hat{a}, \hat{b})$ is shown in Fig. 6.9.

However, the radii of curvature for the transmitted wavefront are calculated using the radii of curvature of the incident wavefront, the principal direction of the wavefront and the surface curvature. These calculations are straightforward in a reference system based on \hat{X}_1^i , \hat{X}_2^i and \hat{s}_i , when the continuity of the phase at the intersection surface is considered. As a result, there are two different reference systems present, and it is necessary to relate them. This can be achieved by introducing a rotation matrix \mathbf{J}_α .

$$\mathbf{J}_\alpha = \begin{bmatrix} \cos \alpha & \sin \alpha \\ -\sin \alpha & \cos \alpha \end{bmatrix} \quad (6.23)$$

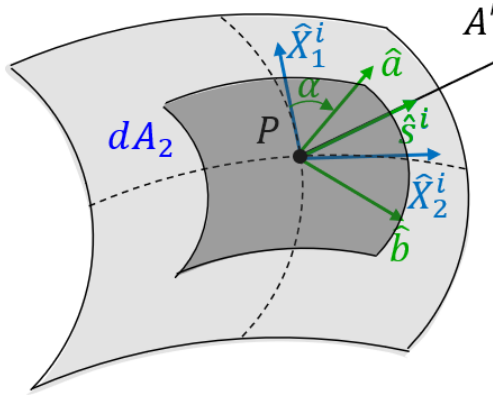


Figure 6.9: The two different coordinate systems shown in point P on the wavefront.

where α is the rotation angle between the two coordinate systems, as shown in Fig. 6.9. α is calculated as

$$\alpha = \arccos(\hat{X}_1^i \cdot \hat{a}) \quad (6.24)$$

The principal radii of curvature of the transmitted wavefront are determined by solving the transmission curvature matrix \mathbf{A}^t as detailed in [19].

$$\mathbf{A}^t = \begin{bmatrix} \frac{k_i A_{11}^i + h C_{11}}{k_t} & \frac{\sec \theta_t (k_i \cos \theta_i A_{12}^i - h C_{12})}{k_t} \\ \frac{\sec \theta_t (k_i \cos \theta_i A_{12}^i - h C_{12})}{k_t} & \frac{\sec^2 \theta_t (k_i \cos^2 \theta_i A_{22}^i - h C_{22})}{k_t} \end{bmatrix} \quad (6.25)$$

where

$$h = k_i \cos \theta_i - k_t \cos \theta_t \quad (6.26)$$

the \mathbf{C} matrix is defined as the curvature of the interface in the neighbourhood of point P_0 . The matrix is defined as

$$\mathbf{C} = \begin{bmatrix} \frac{1}{R_1} & 0 \\ 0 & \frac{1}{R_2} \end{bmatrix} \quad (6.27)$$

where R_1 and R_2 are the principal radii of curvature of the intersection surface [20]. The derivations of R_1 and R_2 are shown in Appendix B. The \mathbf{A}^i matrix is defined as the incident field curvature matrix. This matrix is defined as

$$\mathbf{A}^i = \begin{bmatrix} \frac{\cos \alpha^2}{\rho_1^i} + \frac{\sin \alpha^2}{\rho_2^i} & \cos \alpha \sin \alpha \left[\frac{1}{\rho_1^i} - \frac{1}{\rho_2^i} \right] \\ \cos \alpha \sin \alpha \left[\frac{1}{\rho_1^i} - \frac{1}{\rho_2^i} \right] & \frac{\sin \alpha^2}{\rho_1^i} + \frac{\cos \alpha^2}{\rho_2^i} \end{bmatrix} \quad (6.28)$$

here ρ_1^i and ρ_2^i are the incident radii of curvature. Using these matrices, the principal radii of curvature of the transmitted wavefront are determined by

$$\frac{1}{\rho_{1,2}^t} = \frac{A_{11}^t + A_{22}^t \pm \sqrt{(A_{11}^t - A_{22}^t)^2 + 4(A_{12}^t)^2}}{2} \quad (6.29)$$

In this section, a general principle behind the cascading GO analysis has been explained. The next step is to apply this principle to the analysis problem with the hyper-hemispherical and hyperbolic lens. This is discussed in the next section.

6.3. Propagation of the EM fields through the multi-lens geometry

In this section, the generalized GO analysis is applied to the multi-lens example scenario to find the transmitted fields on the surface S^+ (see Fig. 6.2). Once more, this can be subdivided into three parts as shown in Fig. 6.10.

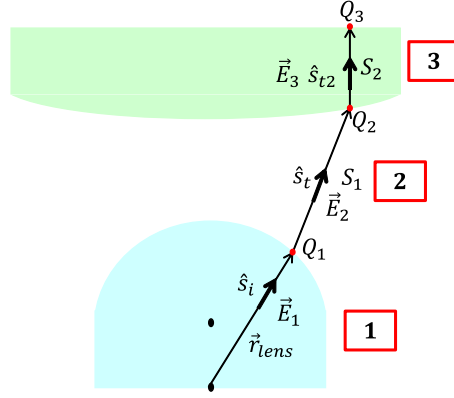


Figure 6.10: The lens setup with the three evaluation points Q_1 , Q_2 and Q_3 .

6.3.1. Finding the field outside the hyper-hemispherical lens

The field at point Q_1 , ($\vec{E}_1(Q_1)$) on the outside of the surface of the hyper-hemispherical lens is found in a similar manner to the method described in Chapter 3. The initial radii of curvature ρ_1^i and ρ_2^i are defined as $|\vec{r}_{lens}^i|$. The principal directions of the wavefront are defined as

$$\hat{X}_1^i = \hat{y} \times \hat{s}_i \quad (6.30a)$$

$$\hat{X}_2^i = \hat{s}_i \times \hat{X}_1^i \quad (6.30b)$$

using these principal radii of curvature and the principal directions of the wavefront, the transmitted radii of curvature and transmitted directions of the wavefront can be calculated. Here, the principal radii of curvature (ρ_1^t and ρ_2^t) are calculated according to Eq. (6.29). The transmitted direction of the wavefront (\hat{X}_1^t, \hat{X}_2^t) are calculated as

$$\hat{X}_1^t = \frac{(A_{22}^t - \frac{1}{\rho_1^t})\hat{x}_1^t - A_{12}^t\hat{x}_2^t}{\sqrt{(A_{22}^t - \frac{1}{\rho_1^t})^2 + A_{12}^t}} \quad (6.31a)$$

$$\hat{X}_2^t = \hat{s}_t \times \hat{X}_1^t \quad (6.31b)$$

where $\hat{x}_1^t = \hat{n}_{Q_1} \times \hat{s}_t$ and $\hat{x}_2^t = \hat{s}_t \times \hat{x}_1^t$. With \hat{n}_{Q_1} being the inward pointing normal vector at point Q_1 .

6.3.2. Finding the field outside the hyperbolic lens

Using the results from the previous section, the field at point Q_2 can be defined as

$$\vec{E}_2(Q_2) = \bar{\mathbf{T}}(Q_1) \cdot \vec{E}_1(Q_1) \sqrt{\frac{\rho_1^t \rho_2^t}{(\rho_1^t + S_1)(\rho_2^t + S_1)}} e^{(-jk_0 S_1)} \quad (6.32)$$

To find the transmitted field at point Q_2 , one needs to find the transmitted radii of curvature, and the transmitted direction of the wavefront. This principle is similar to the previous discussed steps.

6.3.3. Propagating the field to the flat surface

Once the steps are performed, the field $\vec{E}_3(Q_3)$ determined. This field is described as

$$\vec{E}_3(Q_3) = \bar{\mathbf{T}}(Q_2) \cdot \vec{E}_2(Q_2) \sqrt{\frac{\rho_1^{t1} \rho_2^{t1}}{(\rho_1^{t1} + S_2)(\rho_2^{t1} + S_2)}} e^{(-jk_d S_2)} \quad (6.33)$$

where ρ_1^{t1}, ρ_2^{t1} are the principal radii of curvature, and k_d is the propagation constant in the dielectric of the hyperbolic lens. The field on the outside of the surface S^+ (see Fig. 6.2) is given by

$$\vec{E}_{tx}^{flat}(Q_3) = \bar{\mathbf{T}}(Q_3) \cdot \vec{E}_3(Q_3) \quad (6.34)$$

The equivalent currents are then expressed as

$$\vec{M}_t^{flat}(Q_3) = -\hat{n}_Q^{flat}(Q_3) \times \vec{E}_{tx}^{flat}(Q_3) \quad (6.35)$$

$$\vec{J}_t^{flat}(Q_3) = \hat{n}_Q^{flat}(Q_3) \times \vec{H}_{tx}^{flat}(Q_3) \quad (6.36)$$

here, \hat{n}_Q^{flat} is the normal vector of the flat surface; \vec{E}_{tx}^{flat} and \vec{H}_{tx}^{flat} are the transmitted electric and magnetic fields, respectively. Similar to the process in Chapter 3, the currents are radiated using a standard Fourier transform far field approach with the free space Green's function to find the far field.

6.3.4. Efficiency terms for a multi lens QO system

Similar to Chapter 3, the total efficiency η_{tot} is defined as

$$\eta_{tot} = \frac{P_{rx}}{P_{in}} = \frac{|V_{oc} I_{tx}|^2}{16 P_{rad}^{feed} P_{inc}} \quad (6.37)$$

this efficiency can also be split up into multiple terms as follows

$$\eta_{tot} = \eta_{FM} \eta_{ref}^{hh} \eta_{ref}^{hyp} \quad (6.38)$$

where η_{FM} is the field match efficiency; η_{ref}^{hh} is the reflection efficiency of the hyper-hemispherical lens and η_{ref}^{hyp} is the reflection efficiency of the hyperbolic lens. For an optimization problem one could again consider using a multi-variable optimizer with two cost functions ($\frac{1}{\eta_{FM}}$ and $\frac{1}{\eta_{ref}^{hh} \eta_{ref}^{hyp}}$).

Reflection efficiency of the hyper-hemispherical lens

The reflection efficiency of the hyper-hemispherical lens is calculated as:

$$\eta_{ref}^{hh} = \frac{P_{tx}^{hh}}{P_{rad}^{feed}} \quad (6.39)$$

where P_{rad}^{feed} is the transmitted power out of the feed, and it is calculated as previously discussed in Chapter 2. P_{tx}^{hh} is the power transmitted out of the hyper-hemispherical lens, and it is calculated as:

$$P_{tx}^{hh} = \iint_S \frac{1}{2} \Re\{\vec{E}_{tx}^{hh} \times \vec{H}_{tx}^{hh*}\} \cdot \hat{n}^{hh} dS \quad (6.40)$$

where \vec{E}_{tx}^{hh} is the transmitted electric field out of the hyper-hemispherical lens; \vec{H}_{tx}^{hh} is the transmitted magnetic field out of the hyper-hemispherical lens; S is the hyper-hemispherical surface and \hat{n}^{hh} is the normal vector of the hyper-hemispherical lens.

Reflection efficiency of the hyperbolic lens

The reflection efficiency of the hyperbolic lens is calculated as:

$$\eta_{ref}^{hyp} = \frac{P_{tx}^{flat}}{P_{tx}^{hh}} \quad (6.41)$$

where P_{tx}^{flat} is the transmitted power out of the flat part of the lens, and it is calculated as:

$$P_{tx}^{flat} = \iint_S \frac{1}{2} \Re\{\vec{E}_{tx}^{flat} \times \vec{H}_{tx}^{flat*}\} \cdot \hat{n}^{flat} dS \quad (6.42)$$

where \vec{E}_{tx}^{flat} is the transmitted electric field out of the flat part of the hyperbolic lens; \vec{H}_{tx}^{flat} is the transmitted magnetic field out of the flat part of the hyperbolic lens; S is the flat part of the hyperbolic surface and \hat{n}^{flat} is the normal vector of the flat part of the hyperbolic lens.

Field match efficiency

The field match efficiency representing the field match between the incident and transmitted fields is calculated as:

$$\eta_{FM} = \frac{|V_{oc} I_{tx}|^2}{16 P_{inc} P_{tx}^{flat}} \quad (6.43)$$

where P_{inc} is the incident power.

6.4. Physical Optics validation

A Physical Optics (PO) approach is taken in order to validate the results produced by the developed code. In the PO approach, the field that is radiated by a QO component is calculated using the radiative part of the Green's function (GF) as shown in Eq. (6.44) and Eq. (6.45), respectively.

$$\vec{E}_{PO}^i(\vec{r}) = \iint_{S'} j\vec{k}^i \times \vec{M}_{eq}^i \frac{e^{-jk^i|\vec{r}-\vec{r}'|}}{4\pi|\vec{r}-\vec{r}'|} dS' - j\omega\mu \iint_{S'} [\vec{J}_{eq}^i - (\hat{k}^i \cdot \vec{J}_{eq}^i)\hat{k}^i] \frac{e^{-jk^i|\vec{r}-\vec{r}'|}}{4\pi|\vec{r}-\vec{r}'|} dS' \quad (6.44)$$

$$\vec{H}_{PO}^i(\vec{r}) = -\frac{jk^i}{\zeta^i} \iint_{S'} [\vec{M}_{eq}^i - (\hat{k}^i \cdot \vec{M}_{eq}^i)\hat{k}^i] \frac{e^{-jk^i|\vec{r}-\vec{r}'|}}{4\pi|\vec{r}-\vec{r}'|} dS' - \iint_{S'} j\vec{k}^i \times \vec{J}_{eq}^i \frac{e^{-jk^i|\vec{r}-\vec{r}'|}}{4\pi|\vec{r}-\vec{r}'|} dS' \quad (6.45)$$

where $\vec{k}^i = k^i \frac{\vec{r}-\vec{r}'}{|\vec{r}-\vec{r}'|}$. The incident direction of propagation \hat{s}^i as shown in Fig. 6.11 can be approximated by the calculating the pointing vector as

$$\vec{S} = \frac{1}{2} \vec{E}_{PO}^i(\vec{r}) \times \vec{H}_{PO}^{i*}(\vec{r}) \rightarrow \hat{s}^i = \frac{\vec{S}}{|\vec{S}|} \quad (6.46)$$

here the pointing vector is calculated using the incident electric and magnetic field \vec{E}_{PO}^i and \vec{H}_{PO}^i , respectively.

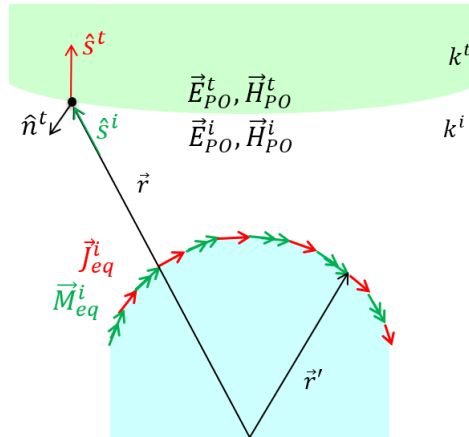


Figure 6.11: An visualisation of the PO validation for the considered scenario

The electric and magnetic transmitted fields from the outside of the secondary surface to the inside of the secondary surface are calculated as in Eq. (6.47) and Eq. (6.48), respectively. From these fields, the transmitted equivalent currents are calculated on the second surface. As a result, the PO analysis can be cascaded.

$$\vec{E}_{PO}^t(\vec{r}) = \bar{\tau}(\vec{r}) \cdot \vec{E}_{PO}^i(\vec{r}) \quad (6.47)$$

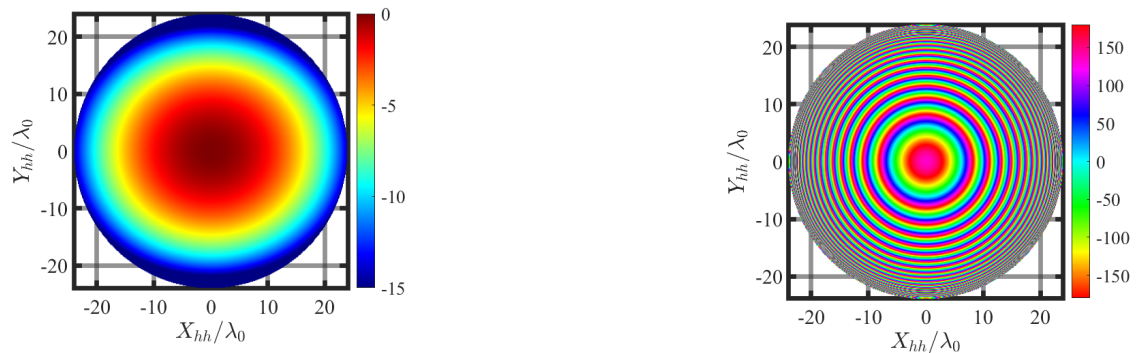
$$\vec{H}_{PO}^t(\vec{r}) = \frac{1}{\zeta_t} \hat{s}^t \times \vec{E}_{PO}^t(\vec{r}) \quad (6.48)$$

6.5. Application cases

As mentioned before, the goal is to analyse double lens geometries using a double GO method. For comparison's sake, the same amount of evaluation points are considered for both the GO and PO methods. This section focuses on three different cases, and results for the previously mentioned analysis methods are shown and compared. The three different analysis cases are considered; a broadside case; a 5 beams scanning case; and a 15 beams scanning case. All of these three cases are validated using the PO approach.

6.5.1. Broadside case

For the broadside case, the tangent electric fields are shown on three different surface of the QO component chains. Fig. 6.12 shows both the amplitude and the phase of the fields on the hyper-hemispherical surface of the lens.

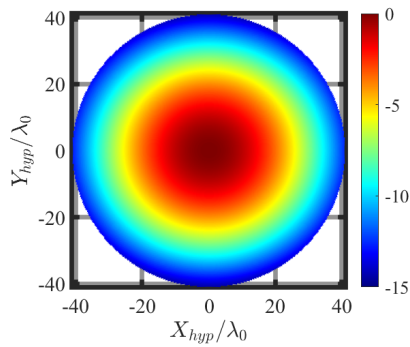


(a) The amplitude of the tangent electric field on the outside of the hyper-hemispherical lens obtained by the GO code.

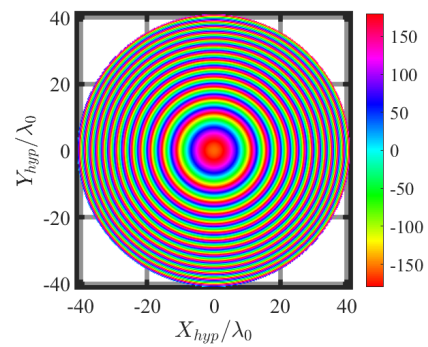
(b) The phase on the surface of the hyper-hemispherical lens obtained by the double GO code.

Figure 6.12: The amplitude and phase on the hyper-hemispherical lens

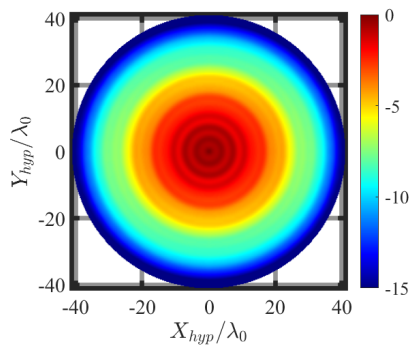
Fig. 6.13 shows the amplitude and phase on the outside of the hyperbolic lens obtained by the double GO code. In addition, the results of the PO validation are shown. As can be observed, both codes produce similar amplitude and phase profiles. Where the amplitude profile has a tapered distribution.



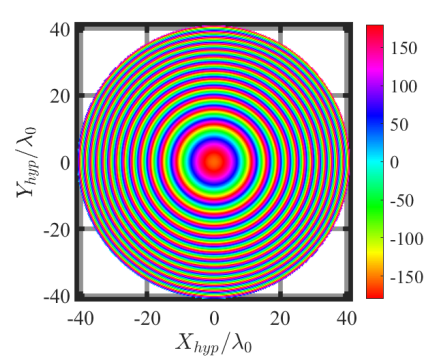
(a) The amplitude of the tangent electric field on the outside of the hyperbolic lens obtained by the GO code.



(b) The phase on the surface of the hyperbolic lens obtained by the double GO code.



(c) The amplitude of the tangent electric field on the outside of the hyperbolic lens obtained by the PO validation method.



(d) The phase on the surface of the hyperbolic lens obtained by the PO validation method.

Figure 6.13: The amplitude and phase on the hyperbolic surface using the GO method (a,b) and the PO validation method (c,d).

Fig. 6.14 shows the amplitude and phase on the flat part of the hyperbolic lens. While the amplitude profiles show similarity, the phase profiles show some discrepancies. For the double GO code, there appears to be a phase difference from the edge to the centre of the lens of approximately 10° . However, the phase profile still remains relatively flat.

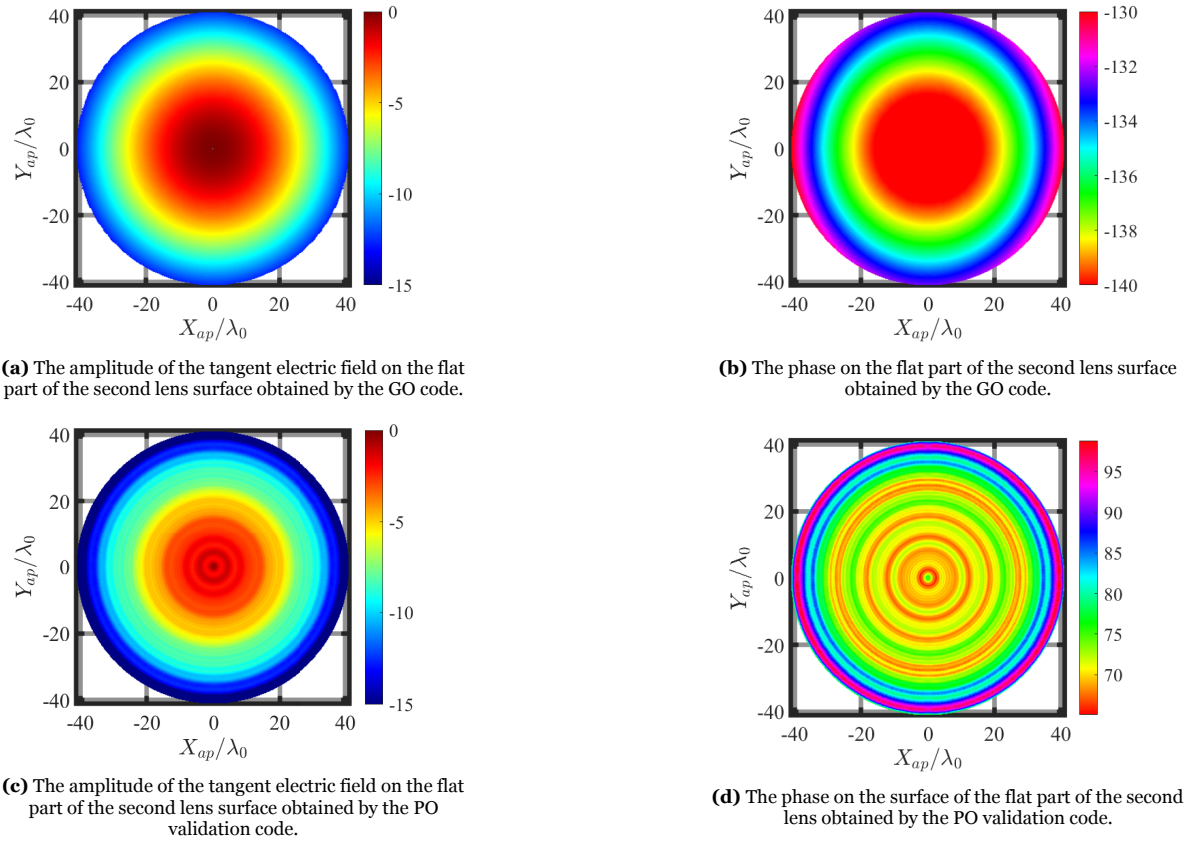


Figure 6.14: The phase and amplitude on the flat surface of the hyperbolic lens with the results of the GO method shown in (a,b) and the results of the PO method shown in (c,d).

The far fields obtained by both methods are compared for the broadside case, they are shown in Fig. 6.15. It is apparent that both methods produce similar results. There is a substantial difference between the operation time of the code. The PO code took approximately 12.5 hours to run, however, the GO code took 15 seconds to run. The gain and directivity are shown in Table 6.1.

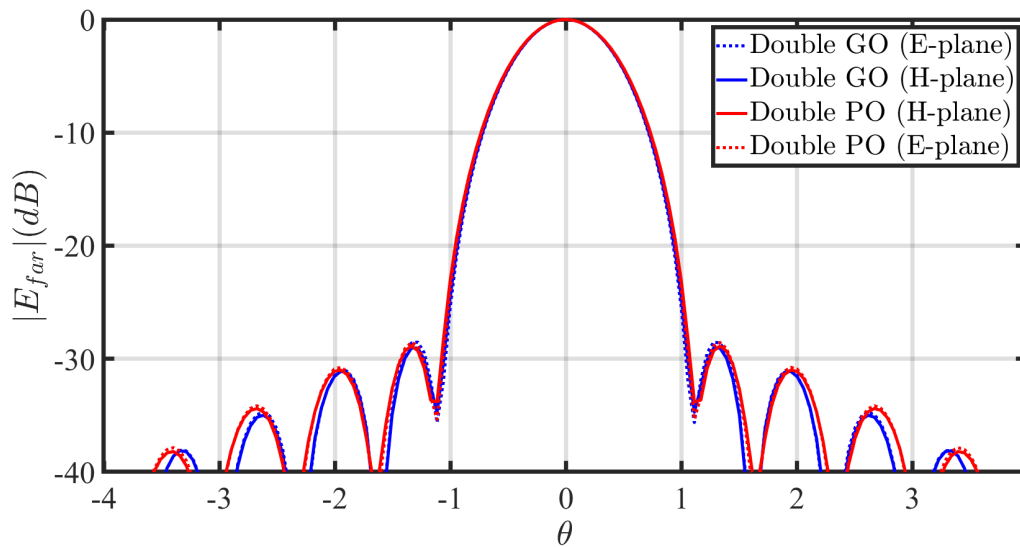


Figure 6.15: The radiated far field for the broadside case.

Table 6.1: The gain and directivity for the broadside case.

Parameter	Value
Directivity (dB)	47.5
Gain (dB)	46.2

6.5.2. Scanning cases

It is also important to determine how well the GO code performs for off-broadside cases. In this work, two scanning cases are considered, a 5 beam scanning case and a slightly more extreme 15 beams scanning case. The feed horizontal displacement for an N beams scanning is determined as

$$x_{ant} = \frac{f_{\#}}{\sqrt{\varepsilon_r^{hh}}} \lambda_d N \quad (6.49)$$

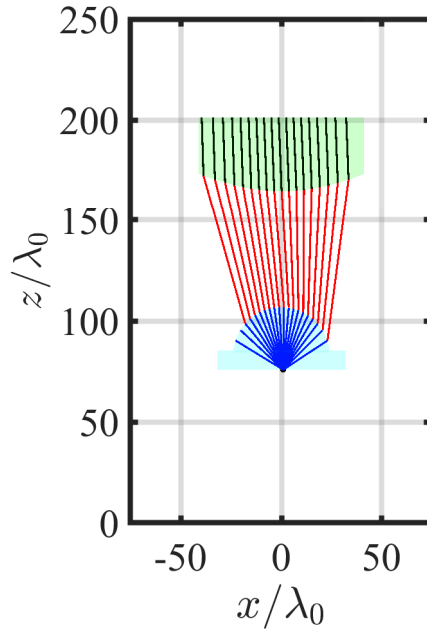
where ε_r^{hh} is the relative permittivity of the hyper-hemispherical lens and λ_d is the wavelength of the hyper-hemispherical lens. These number of beams can also be translated into an angular value that corresponds to the incident angle of the wave. This leads to the following expression

$$\theta_i = -\frac{\sqrt{\varepsilon_r^{hh}} x_{ant}}{L + R_{sph}} \frac{1}{\sqrt{\varepsilon_r^{hyp}}} \frac{180}{\pi} \quad (6.50)$$

where ε_r^{hyp} is the relative permittivity of the hyperbolic lens.

5 beams scanning results

Fig. 6.16 shows the ray tracing results for the 5 beams scanning case. What can be observed is that there is a section of the hyperbolic lens that is not illuminated, this is due to displacement of the feed. There are also some rays on the left side of the hyper-hemispherical lens that are not transmitted to the hyperbolic lens, because they would not hit the hyperbolic lens.

**Figure 6.16:** The ray tracing results for 5 beams scanning

For the 5 beams scanning case, the tangent electric fields are shown on three different surface of the QO component chains. Fig. 6.17 shows both the amplitude and the phase of the fields on the hyper-hemispherical surface of the lens.

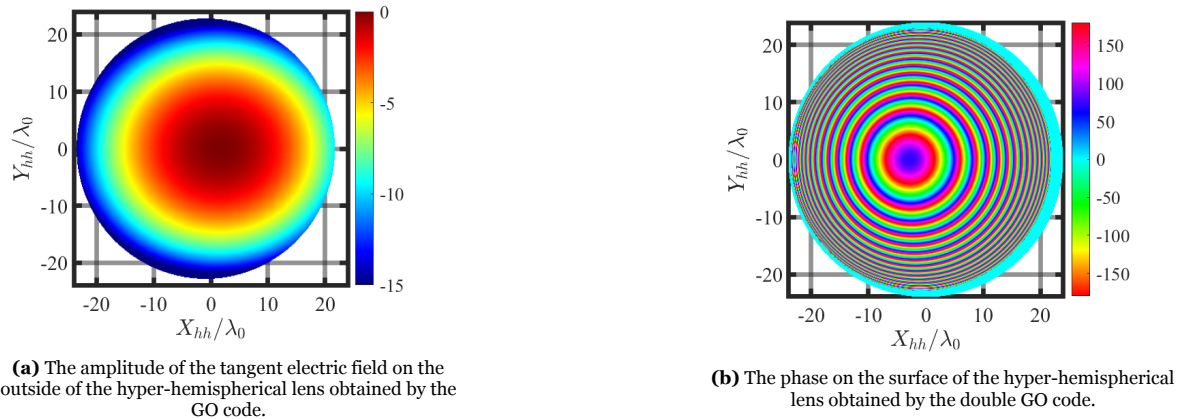


Figure 6.17: The amplitude and phase on the hyper-hemispherical lens

Fig. 6.18 shows the amplitude and phase on the outside of the hyperbolic lens obtained by the double GO code. In the GO method, the rays that do not hit the lens will produce a field that is zero. However, for the PO results, there are some non-zero fields. Moreover, the PO results show some oscillations, which is expected when the evaluation is done when the observation and source grid are close to each other.

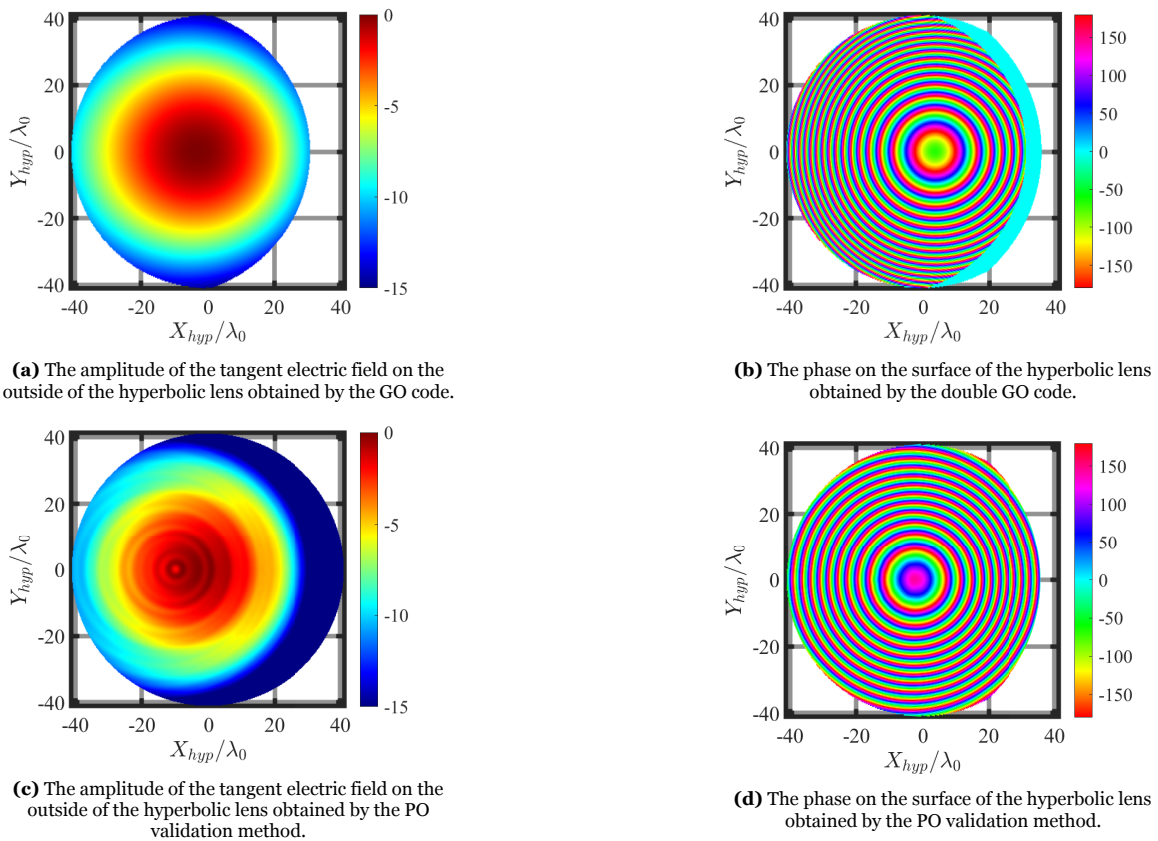


Figure 6.18: The amplitude and phase on the hyperbolic surface using the GO method (a,b) and the PO validation method (c,d).

Fig. 6.19 shows the amplitude and phase on the flat part of the hyperbolic lens. As expected for a displacement, the phases show a linear phase profile.

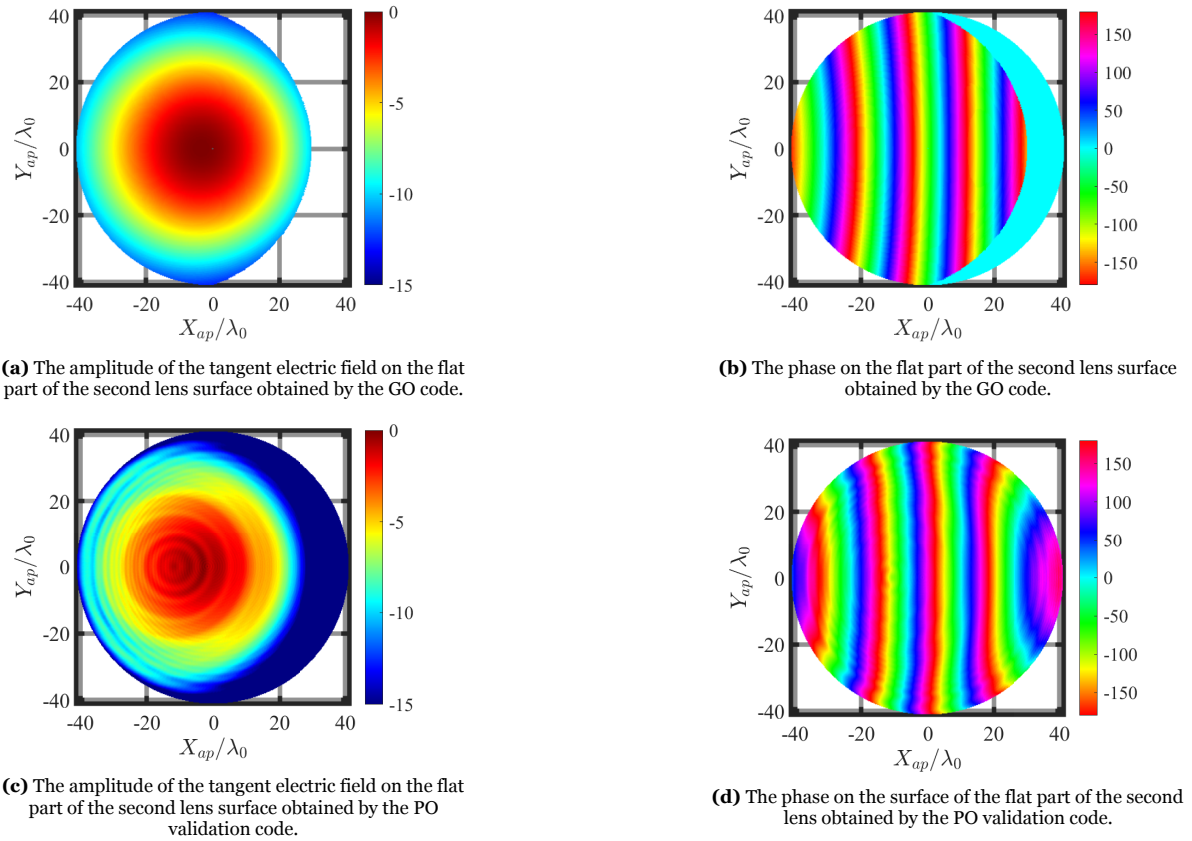


Figure 6.19: The phase and amplitude on the flat surface of the hyperbolic lens with the results of the GO method shown in (a,b) and the results of the PO method shown in (c,d).

The far fields obtained by both methods are compared for the 5 beams scanning case, they are shown in Fig. 6.20. Even for a small displacement, both codes appear to give similar results. In addition, the pattern is less symmetrical than for the broadside case. The gain and directivity are shown in Table 6.2.

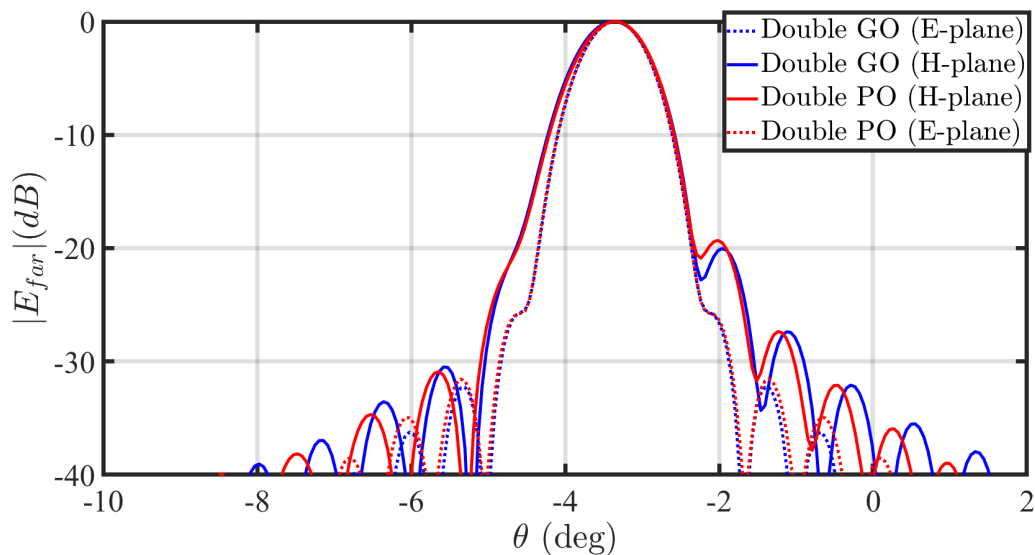


Figure 6.20: The radiated far field for the 5 beams scanning case.

Table 6.2: The gain and directivity for the 5 beams scanning case.

Parameter	Value
Directivity (dB)	46.6
Gain (dB)	45.3

15 beams scanning results

Fig. 6.21 shows the ray tracing results for the 15 beams scanning case. What can be observed, is that in this case nearly half of the hyperbolic lens is not illuminated anymore. The region on the hyper-hemispherical lens where the rays do not transmit has also become larger.

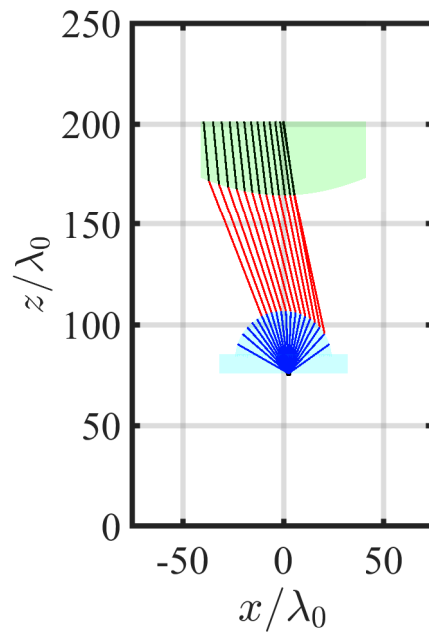
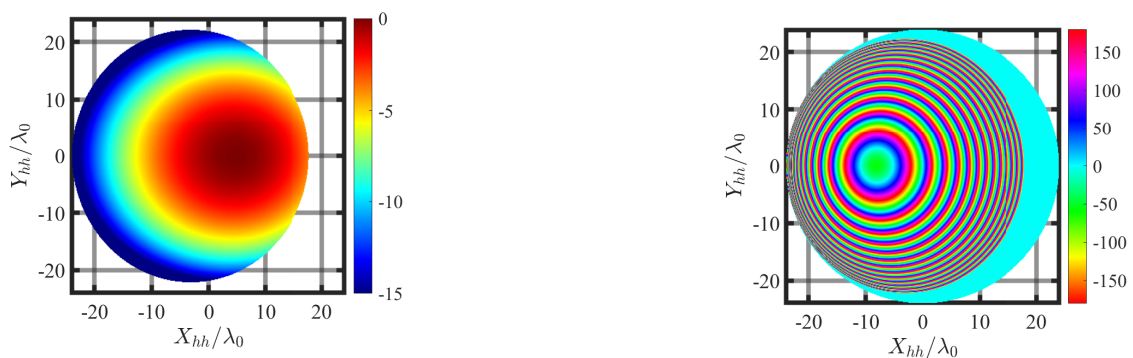
**Figure 6.21:** The ray tracing results for 15 beams scanning**(a)** The amplitude of the tangent electric field on the outside of the hyper-hemispherical lens obtained by the GO code.**(b)** The phase on the surface of the hyper-hemispherical lens obtained by the double GO code.**Figure 6.22:** The amplitude and phase on the hyper-hemispherical lens

Fig. 6.23 shows the amplitude and phase on the outside of the hyperbolic lens obtained by the double GO code.

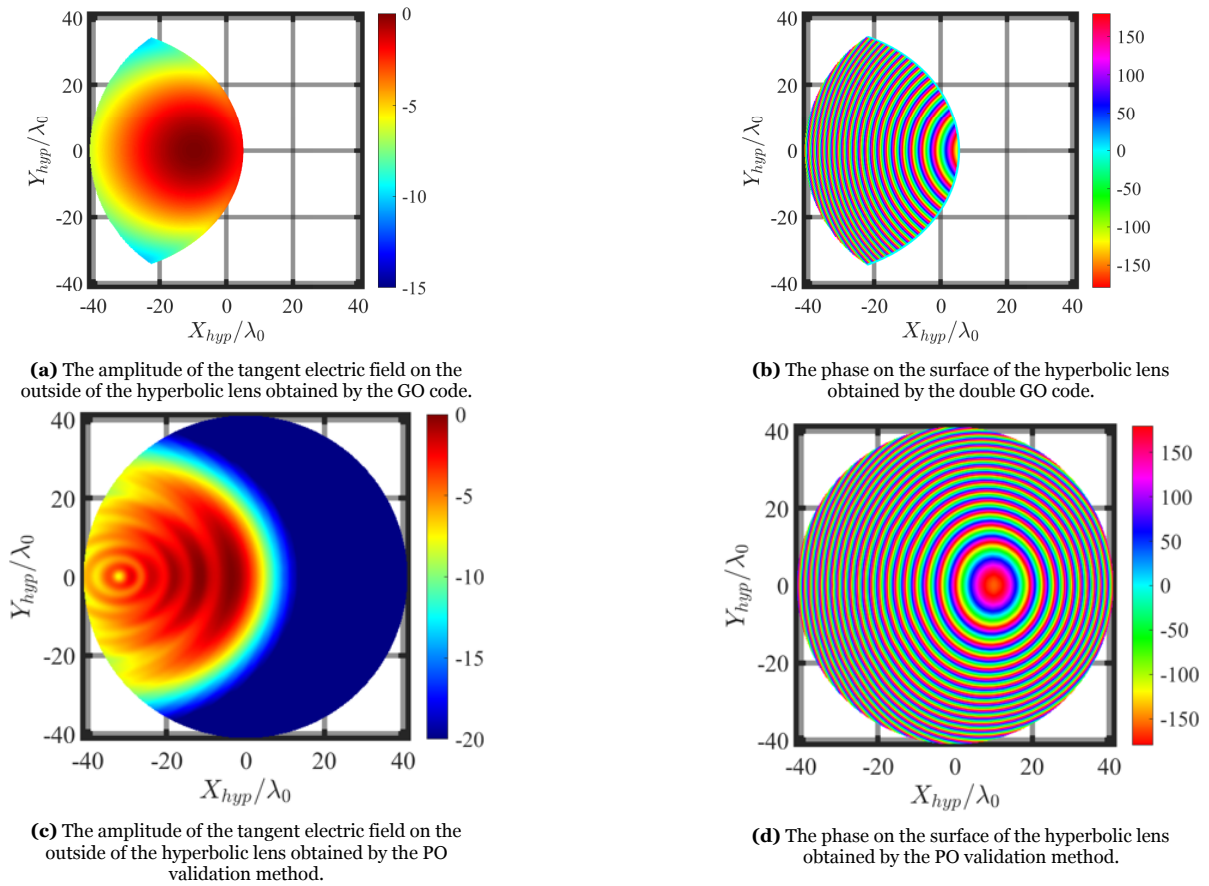


Figure 6.23: The amplitude and phase on the hyperbolic surface using the GO method (a,b) and the PO validation method (c,d).

Fig. 6.24 shows the amplitude and phase on the flat part of the hyperbolic lens. As expected for a displacement, the phases show a linear phase profile.

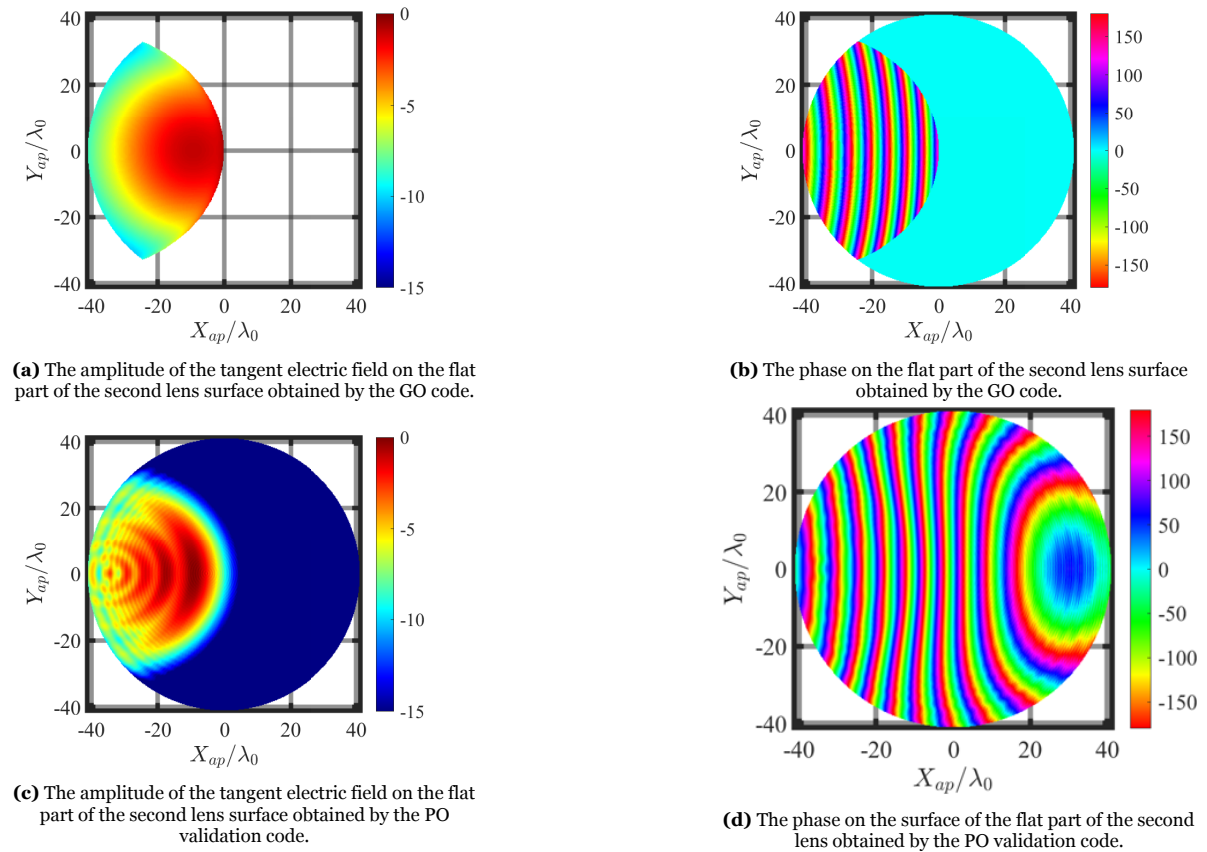


Figure 6.24: The phase and amplitude on the flat surface of the hyperbolic lens with the results of the GO method shown in (a,b) and the results of the PO method shown in (c,d).

The far fields obtained by both methods are compared for the 15 beams scanning case, they are shown in Fig. 6.25. Now it becomes apparent that both the codes produce much more dissimilar results for a more extreme scanning case. It is especially noticeable in the H-plane (solid lines).

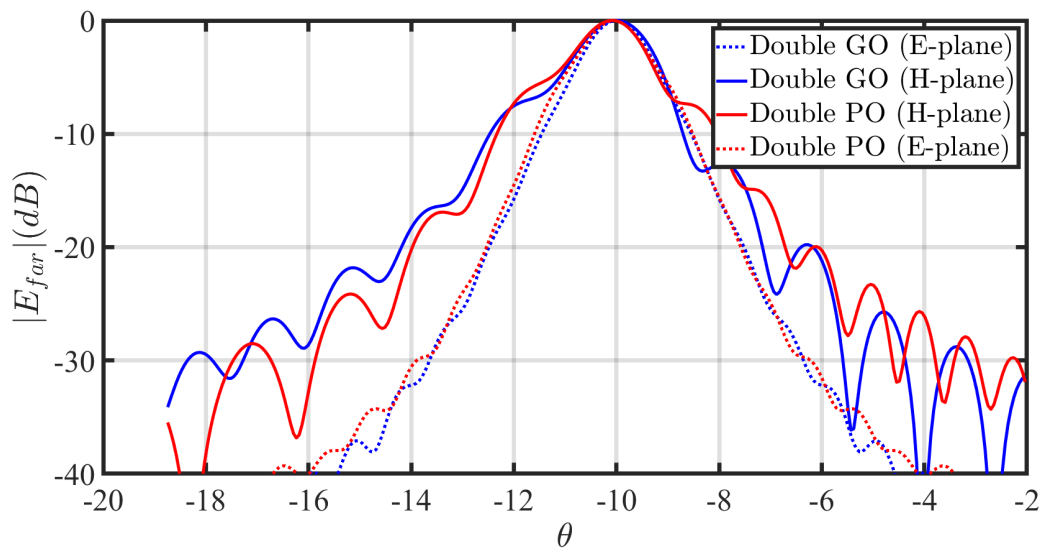


Figure 6.25: The radiated far field for the 15 beams scanning case.

The gain and directivity are shown in Table 6.1. In this chapter, a time efficient method has been pre-

Table 6.3: The gain and directivity for the 15 beams scanning case.

Parameter	Value
Directivity (dB)	40.3
Gain (dB)	38.4

sented that is capable of analysing multi layer QO systems. Table 6.4 shows the time elapsed for both methods.

Table 6.4: The time elapsed for the cascaded GO and the PO analysis.

N_{beams}	GO time	PO time
0	14.9 sec	12.5 hours
5	16.1 sec	12.6 hours
15	24.5 sec	13.1 hours

From the table, it can be observed that the GO is fast compared to the PO method. Moreover, the results presented in this chapter are sufficiently accurate. Therefore, this developed kernel is a feasible solution for more involved design problems.

Conclusion

7.1. Summary and Conclusion

In this thesis, time efficient methods have been presented for the analysis of single lens and multi lens QO systems. In the first part of the thesis, the focus was predominantly on the analysis and optimization of low permittivity elliptical plastic lenses.

In Chapter 2 the lens antenna geometry under investigation was introduced. The lens geometry was shaped by adding a Zernike expansion with varying weights to the canonical ellipsoidal shape. The expression and the derivatives for the Zernike expansion were presented, and some examples of the modes were shown. Finally, the definition of the lens feed was presented. Here a Gaussian pattern was chosen with a -10 dB edge taper level at the lens angle of $\theta_l = 35^\circ$. This representation models the far field pattern of the leaky wave antenna feed in [1].

In Chapter 3 the concept of field correlation on the lens surface is introduced to form a foundation for the optimization kernel. Firstly, the objective of the optimization kernel was explained and the efficiency terms were introduced. Afterwards, the incident and transmitted fields to perform a field correlation were discussed. The transmitted field was determined by a GO plus ray tracing method. The incident field was defined as a plane wave with an amplitude taper.

In Chapter 4 the optimization problem was introduced. The considered optimization parameters were the lens focal length to diameter ratio; the lateral and vertical displacement of the feed; the tilt angle of the feed; and the Zernike expansion coefficients. Furthermore, the setup of the optimizer was presented, where the initial guess points of the optimizer were given in addition to the parameter search range. Lastly, the optimizer choice was presented where a comparison was performed between two MATLAB optimizers and a multi-variable optimizer was chosen. This choice was based on the nature of our optimization problem, where multiple cost functions following different trends must be optimized together.

To conclude the first part of the thesis, a case study of a plastic shaped elliptical lens was introduced in Chapter 5. The main objective was to investigate the performance of the low density integrated lens antennas for large beam steering scenarios. For this, a Fly's eye example case, similar to [1], for a 25° scanning scenario was chosen. The effect of the introduced optimization parameters was investigated and a scan loss of -0.52 dB was obtained. In addition, a validation was performed using CST STUDIO SUITE [13] confirming the performance of the optimization process and the kernel. Furthermore, the bandwidth performance of the shaped lens antenna was presented. Finally, the theoretical scanning performance of plastic lens antennas was investigated, where lens antenna geometries were optimized for 45° and 60° scanning cases. The geometries achieved a scan loss of ≤ 3 dB, showing the potential of low density lens antennas for wide scanning scenarios.

The second part of the thesis focused on the analysis of multi lens systems in Chapter 6. The multi lens analysis was investigated using an example scenario of a hyper-hemispherical and hyperbolic lens based QO system. Firstly, the lens elements were introduced and parametrized. Afterwards, the concept of the cascading GO analysis was explained. The described GO analysis paired together with ray tracing techniques forms the basis for the computational analysis of such multi lens systems. Finally,

the methodology was validated using a multi surface PO analysis. The analysis method was tested for broadside, 5 and 15 beams scanning cases. From this chapter, it can be concluded that the analysis method is significantly more time efficient compared to the physical optics method. The results are accurate for the broadside and 5 beams scanning case. However, for 15 beams scanning case, the results obtained by the two methods diverge.

7.2. Future Outlook

This developed codes form a basis for the analysis and optimization of QO elements. They have been proven to be time efficient with respect to the solutions obtained by commercial software.

Several improvements can be made regarding the multi objective optimization approach. The first improvement is to be able to automatically choose the correct number of polynomials based on the complexity of the problem. In addition, it would also be useful to develop a more consistent method of choosing the best solutions from the solution set of the optimizer.

The developed optimization process including the proposed upgrades will be packaged into a MATLAB based Graphical User Interface (GUI). This can serve as a valuable tool to provide optimized lens antenna solutions for various scanning cases.

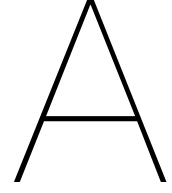
The considered feed tilt in the optimization processes is a theoretical assumption. In the future, a realization of such tilt angles using solutions that are compatible with other QO components is necessary.

For the multi layer lenses, a similar surface expansion can be implemented to compensate for the phase aberrations in a scanning case. This surface expansion can be implemented by means of a symmetrical polynomial for scenarios with an antenna feed array below a single lens. For single feed per lens element scenarios, a Zernike expansion can be used, which allows for asymmetric shape modification.

References

- [1] M. A. Campo, *On the design of Fly's Eye lenses at sub-THz frequencies for wideband communications*. 2021, PhD thesis.
- [2] M. A. Campo, G. Carluccio, S. Bruni, and N.Llombart, "Dielectric gratings enhancing the field of view in low dielectric permittivity elliptical lenses," *IEEE Transactions on Antennas and Propagation*, vol. 69, no. 11, pp. 7308–7322, 2021.
- [3] H. Zhang, S. Dabironezare, M. Zhang, and N.Llombart, "Design of lens based focal plane arrays for wide field-of-view imagers at sub-millimeter wavelengths," *46th International Conference on Infrared, Millimeter and Terahertz Waves (IRMMW-THz)*, 2021.
- [4] S. Karki, J. Ala-Laurinaho, and V. Viikari, "Low-profile scanloss-reduced integrated metal-lens antenna," *IEEE Transactions on Antennas and Propagation*, vol. 70, no. 2, pp. 876–887, 2022.
- [5] E.Gandini, A. Tamminen, A. Luukanen, and N. Llombart, "Wide field of view inversely magnified dual-lens for near-field submillimeter wavelength imagers," *IEEE Transactions on Antennas and Propagation*, vol. 66, no. 2, pp. 541–549, 2018.
- [6] J. Costa, M. Silveirinha, and C. Fernandes, "Evaluation of a double-shell integrated scanning lens antenna," *Antennas Wireless Propagation Letter*, vol. 7, pp. 781–784, 2008.
- [7] S. Dabironezare, G. Carluccio, A. Neto, and N. Llombart, "Analysis of wide band wide-scanning quasi-optical systems based on fourier optics," *47th International Conference on Infrared, Millimeter and Terahertz Waves (IRMMW-THz)*, pp. 1–2, 2022.
- [8] V. Lakshminarayanan and A. Fleck, "Zernike polynomials: A guide," *Journal of Modern Optics*, vol. 58, no. 7, pp. 545–561, 2011.
- [9] A. F. Bernardis, P. Sberna, A. Neto, and N. Llombart, "Signal to noise ratio budget of a picoseconds pulsed radar system for stand-off imaging," *44th International Conference on Infrared, Millimeter and Terahertz Waves (IRMMW-THz)*, pp. 1–2, 2019.
- [10] S. van Berkel, O. Yurduseven, A. Neto, and N. Llombart, "Thz imaging using uncooled wideband direct detection focal plane arrays," *IEEE Transactions on Terahertz Science and Technology*, pp. 481–492, 2017.
- [11] A. E. et al., "First light demonstration of the integrated superconducting spectrometer," *Nature Astronomy*, vol. 3, no. 11, pp. 989–996, 2019.
- [12] N. van Rooijen, M. A. delPino, M. Spirito, and N. Llombart, "Core-shell leaky-wave lens antenna for 150ghz fly's eye communication systems," *47th International Conference on Infrared, Millimeter and Terahertz Waves (IRMMW-THz)*, pp. 1–2, 2022.
- [13] CST. "Cst studio suite 2020." (), [Online]. Available: <https://www.cst.com>.
- [14] T. Tools. "Grasp." (), [Online]. Available: <https://www.ticra.com>.
- [15] S. Dabironezare, G. Carluccio, A.Freni, A. Neto, and N.Llombart, "Coherent fourier optics model for the synthesis of large format lens-based focal plane arrays," *IEEE Transactions on Antennas and Propagation*, vol. 69, no. 2, pp. 734–746, 2021.
- [16] S. Dabironezare, *Fourier Optics Field Representations for the Design of Wide Field-of-View Imagers a Sub-millimetre Wavelengths*. 2020, PhD thesis.
- [17] R. Hoferer and Y. Rahmat-Samii, "Subreflector shaping for antenna distortion compensation: An efficient fourier-jacobs expansion with go/po analysis," *IEEE Transactions on Antennas and Propagation*, vol. 50, no. 12, pp. 1676–1687, 2002.
- [18] I. The MathWorks. "Global optimization toolbox user's guide." (2021), [Online]. Available: <https://www.mathworks.com> (visited on 09/13/2021).

-
- [19] G. James, *Geometrical theory of diffraction for electromagnetic waves*. Stevenage: P.Peregrinus, 1980.
- [20] C. Balanis, *Advanced Engineering Electromagnetics*, 2nd ed. Hoboken, NJ: John Wiley & Sons, 2012.



Derivatives of the Zernike expansion

In this Appendix the detailed derivation of the derivatives for the Zernike expansion is shown. One can define the ρ and ϕ coordinates as

$$\rho = \sqrt{\left(\frac{x}{\frac{D_l}{2}}\right)^2 + \left(\frac{y}{\frac{D_l}{2}}\right)^2} \quad (\text{A.1a})$$

$$\phi = \arctan\left(\frac{y}{x}\right) \quad (\text{A.1b})$$

Where x and y are defined as

$$x = \frac{D_l}{2} \rho \cos \phi \quad (\text{A.2a})$$

$$y = \frac{D_l}{2} \rho \sin \phi \quad (\text{A.2b})$$

The derivative of ρ w.r.t x is given by

$$\frac{\partial \rho}{\partial x} = \frac{x}{\left(\frac{D_l}{2}\right)^2 \sqrt{\left(\frac{x}{\frac{D_l}{2}}\right)^2 + \left(\frac{y}{\frac{D_l}{2}}\right)^2}} = \frac{\frac{D_l}{2} \rho \cos \phi}{\left(\frac{D_l}{2}\right)^2 \rho} = \frac{\cos \phi}{\frac{D_l}{2}} \quad (\text{A.3})$$

The derivative of ϕ w.r.t x is given by

$$\frac{\partial \phi}{\partial x} = \frac{1}{\left(\frac{y}{x}\right)^2 + 1} \frac{-y}{x^2} = \frac{-\frac{D_l}{2} \rho \sin \phi}{\left(\frac{D_l}{2}\right)^2 \rho^2 \sin^2 \phi + \left(\frac{D_l}{2}\right)^2 \rho^2 \cos^2 \phi} = \frac{-\sin \phi}{\frac{D_l}{2} \rho} \quad (\text{A.4})$$

Applying similar steps, one can find the derivatives with respect to y :

$$\frac{\partial \rho}{\partial y} = \frac{\sin \phi}{\frac{D_l}{2}} \quad (\text{A.5a})$$

$$\frac{\partial \phi}{\partial y} = \frac{\cos \phi}{\frac{D_l}{2} \rho} \quad (\text{A.5b})$$

B

Derivations for the radii of curvature of an arbitrary surface

In this appendix the derivation of the R_1 and R_2 terms are provided. This is based on the theory discussed in [20]. One can define an arbitrary surface as

$$z = f(u) \quad (\text{B.1})$$

where

$$u = \frac{x^2 + y^2}{2} \quad (\text{B.2})$$

$$K^2 = 1 + 2u \left[\frac{df(u)}{du} \right]^2 \quad (\text{B.3})$$

The principal radii of curvature are then defined as

$$R_1 = \frac{1}{\frac{1}{K} \frac{df(u)}{du}} \quad (\text{B.4a})$$

$$R_2 = \frac{1}{\frac{1}{K^3} \left[\frac{df(u)}{du} + 2u \frac{d^2 f(u)}{du^2} \right]} \quad (\text{B.4b})$$

The derivatives for a hemispherical lens are given by

$$\frac{df(u)}{du} = -\frac{1}{\sqrt{R_{sph}^2 - 2u}} \quad (\text{B.5a})$$

$$\frac{df^2(u)}{du^2} = -\frac{1}{(R_{sph}^2 - 2u)\sqrt{R_{sph}^2 - 2u}} \quad (\text{B.5b})$$

The derivatives for a hyperbolic lens are given by

$$\frac{df(u)}{du} = \frac{\frac{a}{b^2}}{\sqrt{1 + \frac{2u}{b^2}}} \quad (\text{B.6a})$$

$$\frac{df^2(u)}{du^2} = -\frac{\frac{a}{b^4}}{\left(1 + \frac{2u}{b^2}\right)\sqrt{1 + \frac{2u}{b^2}}} \quad (\text{B.6b})$$